MIT/WHOI

Massachusetts Institute of Technology
Woods Hole Oceanographic Institution

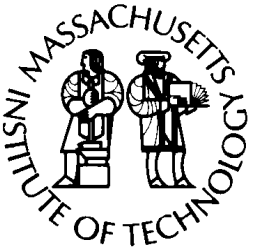

Joint Program in Oceanography/ Applied Ocean Science and Engineering

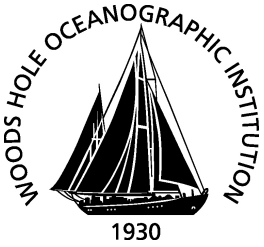

DOCTORAL DISSERTATION

Finescale Abyssal Turbulence:
Sources and Modeling

by

Bryan Edward Kaiser

February 2020

Finescale Abyssal Turbulence: Sources and Modeling

by

Bryan Edward Kaiser
B.F.A., Alfred University (2006)
B.S., University of New Mexico (2013)
M.S., University of New Mexico (2014)

Submitted in partial fulfillment of the requirements for the degree of
Doctor of Philosophy in Physical Oceanography
at the
MASSACHUSETTS INSTITUTE OF TECHNOLOGY
and the
WOODS HOLE OCEANOGRAPHIC INSTITUTION
February 2020

Author .....
Joint Program in Oceanography/Applied Ocean Science and Engineering
Massachusetts Institute of Technology
and Woods Hole Oceanographic Institution
December 20, 2019

Certified by .....
Lawrence Pratt
Senior Scientist
Woods Hole Oceanographic Institution
Thesis Supervisor

Accepted by .....
Glenn Flierl
Chair, Joint Committee for Physical Oceanography
Massachusetts Institute of Technology/
Woods Hole Oceanographic Institution

Finescale Abyssal Turbulence: Sources and Modeling

by

Bryan Edward Kaiser

Submitted on December 20, 2019 in partial fulfillment of the
requirements for the degree of
Doctor of Philosophy in Physical Oceanography

Abstract

A detailed understanding of the intensity and three-dimensional spatial distribution of diabatic abyssal turbulence is germane to understanding the abyssal branch of the global overturning circulation. This thesis addresses the issue through 1) an investigation of the dynamics of an abyssal boundary layer and through 2) the construction of a probabilistic finescale parameterization using mixture density networks (MDNs). A boundary layer, formed by the interaction of heaving isopycnals by the tide and viscous/adiabatic boundary conditions, is investigated through direct numerical simulations (DNS) and Floquet analysis. Turbulence is sustained throughout the tidal period in the DNS on extra-critical slopes characterized by small slope Burger numbers, leading to the formation of turbulent stratified Stokes-Ekman layers. Floquet analysis suggests that the boundary layers are unstable to disturbances to the vorticity component aligned with the across-isobath tidal velocity on extra-critical slopes. MDNs, trained on microstructure observations, are used to construct probabilistic finescale parameterization dependent on the finescale vertical kinetic energy (VKE), $N^2 f^{-2}$, and both variables. The MDN model predictions are as accurate as conventional parameterizations, but also predict the underlying probability density function of the dissipation rate as a function of the dependent parameters.

Thesis Supervisor: Lawrence Pratt
Title: Senior Scientist
Woods Hole Oceanographic Institution

Acknowledgments

I wish to express my sincere gratitude to my advisor, Larry Pratt. Larry's curiosity, creativity, patience, perspective, trust, and openness taught me how to think like a scientist. The transformation from engineer to scientist took me a long time, as I finally came to appreciate the freedom of choosing and approaching problems as a scientist. Larry was an invaluable part of that process. It was a privilege to work with him and I am grateful for all of the experiences I've had under his mentorship.

I thank my committee, Jörn Callies, Jesse Canfield, Raf Ferrari, Karl Helfrich, and Andreas Thurnherr, for fruitful discussions, support, and guidance. I am grateful to Jörn for the numerous conversations we had as office mates and his contributions to the DNS chapter of this thesis. I am grateful to Jesse for discussions regarding the numerical schemes I employed in the Floquet analysis chapter, grateful to Karl for teaching me everything I know about internal waves, grateful to Andreas for pushing to think about what actually occurs in the deep ocean, and grateful to Raf for pushing me to consider how my work fits into the larger narrative of the role of deep ocean turbulence in Earth's climate.

I thank Glenn Flierl, Kurt Polzin, and John Toole for valuable discussions, and I further thank John for chairing my defense and Kurt for taking me to sea (twice) and giving me the opportunity to understand first hand how turbulence is measured in the ocean. I also thank Alison MacDonald for taking me to sea for a WOCE repeat hydrography cruise.

I am grateful to all of the administrative, academic, and program support staff whose work makes the Joint Program possible. In particular, I thank Roberta Allard, Matt Barton, Martha Bridgers, Lea Fraser, Kevin Kerwin, Kris Kipp, Christine Maglio, Brandon Milardo, Delia Oppo, Jean Taft, Meg Tivey, and Julia Westwater.

I am particularly grateful to the community of EAPS/JP students and postdocs. Not only did I find many wonderful friends and research colleagues in them, I came to rely on quite a few of them for logistical support while I remotely completed the end of the PhD. I am especially grateful to Astrid Pacini for her concern for my wellbeing and her support. I am grateful to Carlos Alvarado, Sebastian Essink, Evan Howard, Matt "Oz" Osman, Danielle Potter, Kate Sawatzki, Kane Stone, Kevin Sutherland, and Colin & Kelly Thackray for

providing lodging and transportation on many occasions. I am grateful for all of the friends I've made in the program, who are too numerous to list here.

I thank Mary Beth Libbey for the many hours she spent editing my thesis and other documents, this document would undoubtedly be incoherent without the technical writing skills that I learned from her.

I am grateful to my parents and my brothers for their steadfast support and encouragement. I am also grateful to Loren Kahn and Isabelle Kessler, who have in effect become family. I deeply appreciate their support and guidance. I also wish to express gratitude to Meredithe and Roc Sweeney, who have been incredibly supportive friends.

Most of all, I am grateful to my wife Fran, as she has made countless sacrifices to help me reach this point, from moving to Boston for me to attend the Joint Program, to dealing with extended periods of my stress. I could not have done this without her love and support and this thesis is dedicated to her.

My doctoral studies in the WHOI/MIT Joint Program were funded by the National Science Foundation (OCE-1657870) and the National Science Foundation Graduate Research Fellowship Program.

Contents

List of Figures

List of Tables

Chapter 1

Introduction

Due to its immense thermal inertia, the ocean dominates the climate system on long timescales (e.g. Dommenget (2009)). It absorbs more heat than any other component of the climate system; between 1955 and 2016 it absorbed more than 90% of the extra heat trapped on Earth (Levitus et al. (2012); Wijffels et al. (2016)), and it continues to steadily warm at the present moment. The magnitude of recent ocean warming portends a different future climate, relative to the present, because the ocean redistributes and stores heat on long timescales and over great distances. If the ocean fluxed all of the extra heat accumulated in the preceding six decades directly into the lower atmosphere in one day, the global mean warming of the lower atmosphere would be approximately 36°C/65°F (Levitus et al. (2012)). While that scenario is grossly simplistic and inconsistent with the physics of the Earth's climate, it illustrates the low frequency and large magnitude role of the ocean's heat budget on the climate system.

The ocean has also absorbed approximately half of all anthropogenic CO_2 emissions between 1800 to 1994, and it has the capacity to sequester much more (Sabine et al. (2004)). Heat loss and brine rejection at the surface at high latitudes drives the formation dense waters, laden with absorbed CO_2 and other dissolved gases, that sink into the abyss and then slowly spread throughout the global abyss (Wunsch and Ferrari (2004)). The sequestering of dissolved gases and other surface properties in the abyssal ocean effectively gives the ocean a long "memory" of atmospheric conditions (Primeau and Holzer (2006)). However, the abyssal ocean is "ventilated:" conservation of mass for a nearly incompressible fluid requires

that a volume flux into the abyss must be approximately balanced by a volume flux out of the abyss. The mechanisms and spatial distribution of abyssal ventilation is linked to regulation of atmospheric CO_2 levels on long time scales (Sarmiento and Toggweiler (1984); Ferrari et al. (2014)).

1.1 The abyssal branch of the global overturning circulation

The ventilation rate of the abyssal ocean is a crucial component of the global overturing circulation (GOC), which is central to variations in Earth's climate (Talley (2013)). The abyssal branch of the GOC (the lowest blue and green lines of the schematic of Talley (2013) shown Figure 1-1) is fed by water subducted at a rate of approximately 30 Sverdrups (10^6 m^3s^{-1}) near the poles (Munk and Wunsch (1998)), balanced by spatially heterogeneous upwelling across all ocean basins (St. Laurent and Simmons (2006)). The upwelling is exceedingly difficult to measure directly: 30 Sv of upwelling spread uniformly across the Pacific, Atlantic, and Indian oceans (area $\sim 3 \cdot 10^8$ m^2) would upwell at a rate of 3 m yr^{-1}. Even though the upwelling is unlikely to be uniform, the difficulty involved in adequately sampling such small velocities over large areas over long time periods is prohibitive. Instead, diapycnal mixing is inferred from measurements of the microstructure (shear and temperature fluctuation measurements that resolve the dissipation range of turbulence, see Figure 1-2), or estimates of turbulence diffusion by measuring the distribution of released tracers. Inferred upwelling and downwelling rates, volume averaged over individual ocean basins, inform the "conveyor belt" portrait of the Eulerian residual bulk flow of abyssal branch of the GOC shown in the schematic of Talley (2013) in Figure 1-1. For a comprehensive discussion of the dynamics of the entire GOC, the reader is referred to Cessi (2019).

Although the dynamics of the abyssal circulation contrast that of upper ocean dynamics above the thermocline, where planetary vorticity and the curl of the wind stress controls the basin-scale circulation, the upper ocean and the abyssal circulations are intertwined (Ferrari et al. (2014)). After downwelling near Antarctica, in the Labrador Sea, and in the Nordic Sea

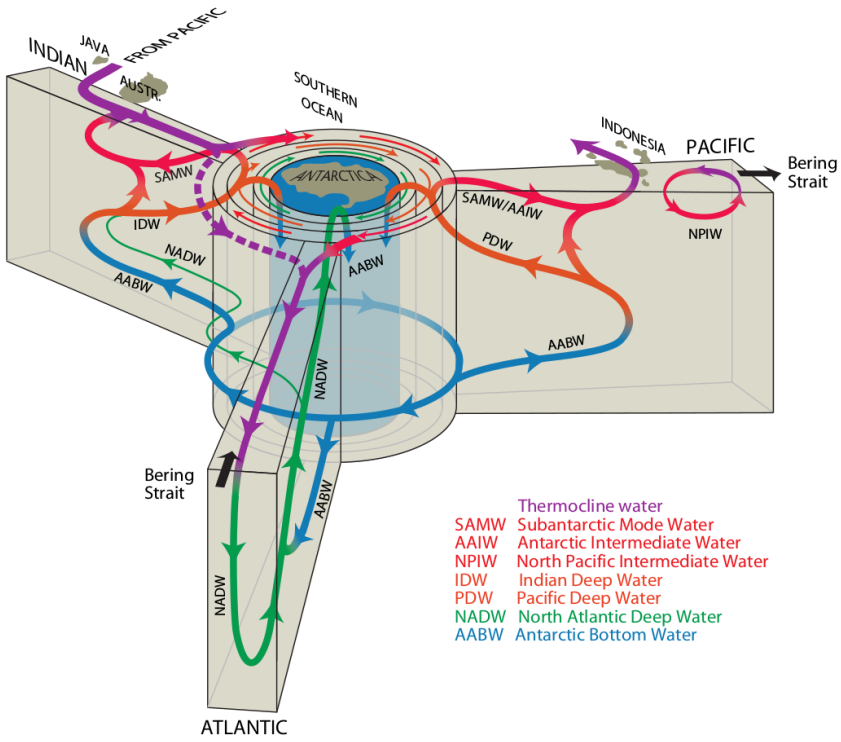

Figure 1-1: Schematic of the global overturning circulation by Talley (2013).

(the downwards blue and green arrows in Figure 1-1), Antarctic Bottom Water (AABW) and North Atlantic Deep Water (NADW), are transported by the abyssal circulation laterally before rising to approximately 2000 m depth (Lumpkin and Speer (2007); Marshall and Speer (2012)). Above approximately 2000 m depth, intermediate waters are driven adiabatically (i.e. along neutral density surfaces, where neutral density is the density corrected to eliminate dynamically negligible compressive effects that increase the water density at depth, Jackett and McDougall (1997)) by upper ocean wind-driven circulation (the upwards blue-to-red lines and blue/green upward lines in Figure 1-1 of Talley (2013)) to eventually outcrop at the surface in the Southern Ocean (Marshall and Speer (2012); Ferrari et al. (2014)). The processes and controlling dynamics of how the bottom waters rise to approximately 2000 m depth is, arguably, the least understood component of the GOC and motivates the research presented in this thesis.

To exit the abyss, water masses must cross density surfaces (Lumpkin and Speer (2007); Talley (2013); Ferrari et al. (2014)), diabatically transforming into less dense fluid. The relevance of diabatic dynamics to abyssal upwelling was anticipated by Munk (1966), who

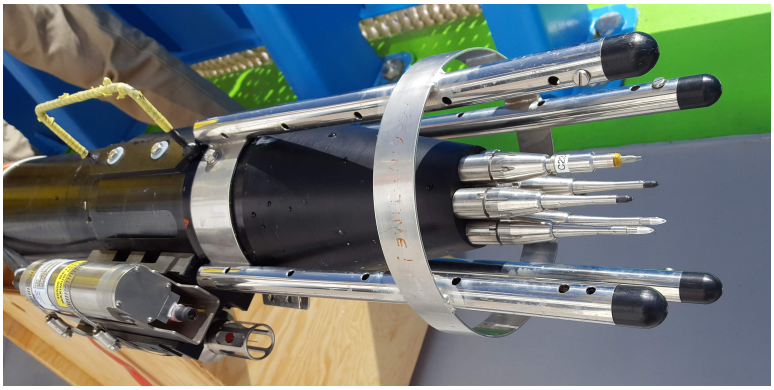

Figure 1-2: A vertical microstructure profiler deployed by the author in November 2018.

pointed out that a one-dimensional (the vertical) stratified ocean must be in advective-diffusive balance to maintain a steady state stratification in the presence of upwelling. In Munk's toy model, the diffusion of buoyancy (e.g. heat) downwards is exactly balanced by advection across surfaces of constant buoyancy. In Munk's formulation the advective-diffusive balance lies purely in the vertical direction; hence, diabatic water mass transformation and abyssal upwelling are often understood as synonyms. Recent work (Thurnherr and Speer (2003); Polzin (2009); Ferrari et al. (2016); Lavergne et al. (2017); Holmes et al. (2018)) suggests that horizontal geometric constraints on the water mass transformation plays an important role in setting the spatial distribution of abyssal upwelling. In recent years, the number of and geographic spread of samples of observation-inferred diapycnal mixing has accumulated to permit the calculation of global mean estimates of diapycnal mixing in the deep ocean (mixing is an arguably ambiguous term; here diapycnal mixing refers unequivocally to rates of irreversible buoyancy flux convergence/divergence). The most recent calculation of total diapycnal mixing (abyssal and upper ocean), contemporary with the writing of this thesis, by Waterhouse et al. (2014), roughly agrees with the estimate of Munk (1966) required to maintain the observed global mean thermocline.

1.2 Abyssal turbulence and mean flows

As a box model (a ocean basin average perspective, Figure 1-1) portrait of the abyssal branch of the GOC began to emerge around the turn of the millenium (viz. Talley (2013)),

so did questions regarding how to reconcile the magnitude of basin-average diapycnal mixing with observations of inferred diapycnal mixing, which suggested the distribution of mixing is highly heterogeneous in the horizontal and vertical directions (Toole et al. (1994); Polzin et al. (1997); Ledwell et al. (2000); Thurnherr et al. (2005); Kunze et al. (2006); St Laurent and Thurnherr (2007); Whalen et al. (2012); MacKinnon et al. (2013); Waterhouse et al. (2014)). The Brazil Basin Tracer Release Experiment (Polzin et al. (1997),Toole et al. (1997),Ledwell et al. (2000)) was an early diapycnal mixing field campaign that unambiguously illustrated the complexity of the diapycnal mixing in the abyssal ocean. By using a microstructure profiler to measure dissipation rates of turbulent kinetic energy and by using measurements of tracer spread, they inferred that the distribution of diapycnal mixing on the western flanks of the Mid-Atlantic Ridge varied horizontally by proximity to distinct bathymetric features (canyons, the crest of ridge flanks, etc) and dramatically in the vertical (see Figure 1-3). A striking feature of Figure 1-3 is the intensification of the inferred diapycnal mixing with depth. The rate of water mass transformation can be determined by the divergence of the irreversible buoyancy flux. The observed increase in mixing with depth in the Brazil Basin implies a divergence of buoyancy flux and thus downwelling, as the effect of localized patches of mixing is to increase the density of water at a given depth. Polzin et al. (1997) hypothesized that the abyssal mass budget of the Brazil Basin is closed by the buoyancy flux convergence within the deep canyons that run up the flanks of the Mid-Atlantic Ridge. Observations by Thurnherr et al. (2005) of a cross-isopycnal, time mean, up canyon flow measured by current meters in a Mid-Atlantic Ridge canyon over a two year period support the canyon buoyancy flux convergence hypothesis.

The horizontal structure (approximately along-isopycnal) of abyssal flows appears just as complex as the vertical structure. A mean circulation of meridionally and vertically interwoven zonal currents flowing both directions has been repeatedly observed in another set of Brazil Basin studies (Hogg and Owens (1999); Thurnherr and Speer (2004); St.Laurent et al. (2001)), that are markedly inconsistent with the early theoretical models of Stommel et al. (1958) and Stommel and Arons (1960), in which it is assumed that the upwelling is uniformly distributed in the horizontal. The difference is explained by the fact that, in the absence of other sources of energy, irreversible buoyancy flux convergences/divergences

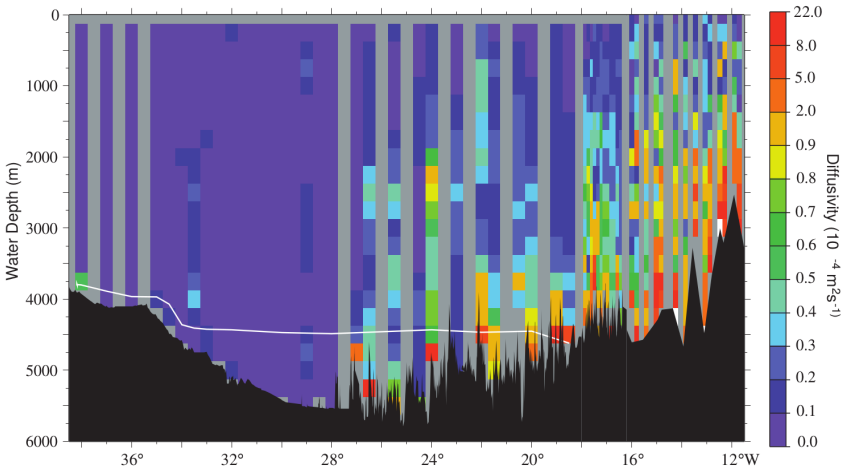

Figure 1-3: Brazil basin depth-longitude diapycnal diffusivity from Polzin et al. (1997).

push and pull mass laterally as isopycnals spread/collapse. This phenomena of buoyany-flux-driven lateral mass exchange appears to be robust with respect to the source of the irreversible buoyancy flux convergences/divergences: it occurs in constant diffusivity flows with sufficiently rough bathymetry (Dell and Pratt (2015)), in the interaction of a turbulent boundary layer and a pycnocline in the mean stratification (Phillips et al. (1986)), in observed flows with variable stratication and turbulence (St.Laurent et al. (2001)), and in theoretical models of idealized diapycnal mixing over a set of simple seafloor geometries (Holmes et al. (2018)).

The influence of the spatial distribution of diapycnal mixing also appears to be a considerable source of uncertainty in the abyssal flows in ocean circulation models. Numerical models suggest that the rate at which the abyssal branch of the GOC is ventilated and that the abyssal horizontal circulation are dependent on the spatial distribution of diapycnal mixing (Large et al. (1994); Munk and Wunsch (1998); Huang and Jin (2002)). Melet et al. (2013) compared the exponentially decaying parameterizations of abyssal mixing of St.Laurent and Garrett (2002) and Simmons et al. (2005) with the Polzin (2009) model, in which the internal tide dissipation decays algebraically with height above the bottom as a function of the stratification, and found that the Indo-Pacific overturning circulation is sensitive to the choice of model for internal tide driven mixing. Taken together with observations and theory, the sensitivity of numerical models to the distribution of diapycnal mixing implies that the abyssal circulation, in three dimensions, is primarily controlled by

buoyancy flux convergence/divergence.

Munk and Wunsch (1998) concluded that the buoyancy flux convergence/divergence needed to drive the upwelling branch of the overturning circulation is primarily a function of the rate of mechanical energy supplied by the wind and tides; geothermal heat fluxes in the deep ocean only contribute to a small percentage of the total buoyancy flux convergence. Abyssal buoyancy flux convergence/divergence is often attributed to the breaking of internal waves resulting from wave-wave interactions. So-called internal tides are internal waves generated as the barotropic tide forces stratified flows to oscillate over rough bathymetry (St.Laurent and Garrett (2002); Garrett and Kunze (2007)). Regions of enhanced diapycnal mixing rates, such as the Mid-Atlantic Ridge sites investigated in the BBTRE, are often so because they are sites of intense internal tide generation (Lueck and Mudge (1997); Polzin et al. (1997); Ledwell et al. (2000); Pinkel et al. (2000)) where high wavenumber internal waves propagate too slowly to escape the local internal wave field and therefore tend to dissipate locally through nonlinear interactions (Polzin (2004), Polzin (2009)).

Internal waves generate turbulence in a number of ways other than wave-wave interactions. The reflection and/or generation of internal waves at critical slopes, where the group velocity of the wave is parallel to the slope, produces patches of intense turbulence and diapycnal mixing. Stratified flows oscillating over topography can also produce internal lee waves, and hydraulically controlled flows (such as cross-sill flows in canyons (Thurnherr et al. (2002)), and hydraulic jumps, such as in the Luzon Strait (Alford et al. (2011)). Non-Boussinesq flow phenomena, double diffusive flows, and phenomena associated with nonlinearities in the equation of state for seawater may also be important for abyssal diapycnal mixing and will not be addressed in this thesis. The interested reader is referred to Gregg et al. (2018).

Finally, the viscous and diffusive boundary layer that forms as the internal tides heave isopycnals across isobaths of sloping bathymetry to produce boundary layers that have been observed on continental slopes (Gemmrich and Van Haren (2001); Gemmrich and van Haren (2002)) and continental shelves (Shaw et al. (2001)) are another source of abyssal turbulence but are not well sampled in the deep ocean. Before proceeding, it is necessary to define precisely what is meant by the term "boundary layer." Prandtl (1904) articulated the concept

of a fluid boundary layer as a thin region near a frictional, impermeable surface in which low Reynolds number effects predominate. Goldstein et al. (1938) formalized Prandtl's concept with the method of matched asymptotic expansions, a sweeping formalism that generalized the concept of a boundary layer beyond fluid dynamics. The boundary layers examined in this thesis adhere to Prandtl's concept of a boundary layer, in which the rate of production of turbulent kinetic energy arises *directly because of* viscous and/or diffusive boundary effects. However, in the abyssal ocean, the observations of bottom-intensified dissipation rates, driven by primarily inviscid processes, such as internal wave breaking, occur within a layer of approximately 10-1000 m above the seafloor that is sometimes referred to as a boundary layer in the literature. In order to distinguish it from the Prandtl-type bottom boundary layer, such regions are perhaps more aptly referred to as "stratified mixing layers" (Ferrari et al. (2016)). The next two chapters of this thesis explore the dynamics of "internal tide boundary layers" (Thorpe (2007)) on hydraulically smooth slopes and in conditions typical of mid-latitude abyssal slopes.

1.3 Perspective and thesis outline

Science is an exercise of methodological reductionism: explanations of patterns in observed physical systems are sought by reducing physical systems to sub-systems that can be explained by hypothesis testing. The research in this thesis is a manifestation of two meditations on methodological reductionism: 1) that it is worthwhile to explain every sub-system in attempting to explain a larger system; and 2) that in highly nonlinear, chaotic systems, advances in predictive skill can be made by abandoning reductionism in favor of data-driven (as opposed to theory-driven) analyses. If the ultimate measure of success of a scientific theory is defined by its predictive skill, then 2) is of equal merit to 1). On the other hand, a data-driven prediction without at least a elemental understanding of the meaning and context of the result is a potentially dangerous *deus ex machina*. The advent of sufficient computing power for the routine application of machine learning to complex problems and the seemingly intractible mathematical properties of large nonlinear physical systems, such as Earth's climate, begs the question: if a tool can create its own successful "theories," how

do we translate such theories into science?

The first (approximately) two thirds of this thesis adheres to the first meditation and pertains to studies of the dynamics of a geometrically idealized boundary layer in isolation. The examined boundary layers are relevant to smooth near-constant abyssal slopes and are formed by the interaction of the heaving of constant density surfaces by the internal tide and the viscous/adiabatic boundary conditions of the slope. The boundary layers are investigated through direct numerical simulations (DNS) and Floquet stability analysis, and address the question: *What are the dynamics (viz. stability, mixing efficiency, turbulence production mechanisms) of oscillating, stratified, viscous, diffusive sloping boundary layers as functions of slope criticality, Reynolds number, and Rossby number?* The diapycnal mixing of the internal tide wave field that gives rise to the boundary layers investigated in this thesis is surely larger than the diapycnal mixing that the boundary layers could produce alone. Therefore, the point of examining the boundary layers is not to look for "hot spots" of diapycnal mixing, but rather to understand the fundamental dynamics of the flow. Such an understanding may lead to insights into the dynamics of the larger scale flows in which the boundary layer is embedded, and will illuminate the boundary layer physics that are important for numerical model validation.

The last study in this thesis pertains to the construction of a finescale parameterization for the dissipation rate of turbulent kinetic energy by modeling the underlying probability density functions of observed dissipation rates by region. The work addresses the question: *can the accuracy of finescale parameterizations of ocean turbulence be improved by relaxing the assumption of a time- or ensemble-mean state in order to include time-dependent aspects of the turbulence?* Finescale parameterizations of the dissipation rate are usually constructed as deterministic ensemble-mean predictions in terms of the properties of the local internal wave field, which varies on hourly time scales. The data-driven finescale parameterization in the last study in this thesis is probabilistic. Therefore it can be used as either a deterministic ensemble-mean prediction tool or as a stochastic model of localized intermittent turbulence, which has a probability density function controlled by the statistical behavior of the local turbulence production mechanisms.

Chapter 2

Direct Numerical Simulations

Recent observations suggest that mechanical energy supplied by the barotropic tides contributes a significant percentage of the rate of irreversible buoyancy flux convergence (a.k.a. water mass transformation) in the abyssal ocean (Egbert and Ray (2000), Wunsch and Ferrari (2004)). Baroclinic tides, or internal tides, are oscillations in pressure, buoyancy, and velocity with vertical structure formed by the forcing of rotating, stratified flow over variable bathymetry by the barotropic tide. In the deep ocean, baroclinic tides are generated by and propogate away from roughness features with horizontal scales of $\mathcal{O}(10$ km) or larger (Jayne and St. Laurent (2001),Garrett and Kunze (2007)). On much smaller length scales, within $\mathcal{O}(10$ m) of the seafloor, baroclinic tides manifest as the approximately slope parallel heaving of isopycnals up and down the flank of the much larger roughness feature such as an abyssal hill or continental rise. Bottom friction acts on the oscillating flow to produce baroclinic tide boundary layers (BTBLs), sometimes referred to as "swash zones" (Polzin (2009)), "internal slope boundary layers" (Thorpe and Umlauf (2002)).

Detailed in situ observations of abyssal BTBL turbulence are difficult to obtain and are complicated by the presence of myriad of turbulence production mechanisms, including but not limited to gravitational instabilities, Ekman instabilities, oscillating shear instabilities, nonlocal and nonlinear forcing by the flow on the (much larger) scales of the baroclinic tide generation, reflected internal waves, hydraulic roughness, and flow separation arising from roughness features that are much larger than the viscous length scale but much smaller than the excursion length of the tide. However, despite a recent surge of interest in the

role of turbulent processes in the abyssal branch of the global overturning circulation, the instabilities, turbulence production mechanisms, and mixing "efficiency" of even idealized BTBLs remains largely unknown.

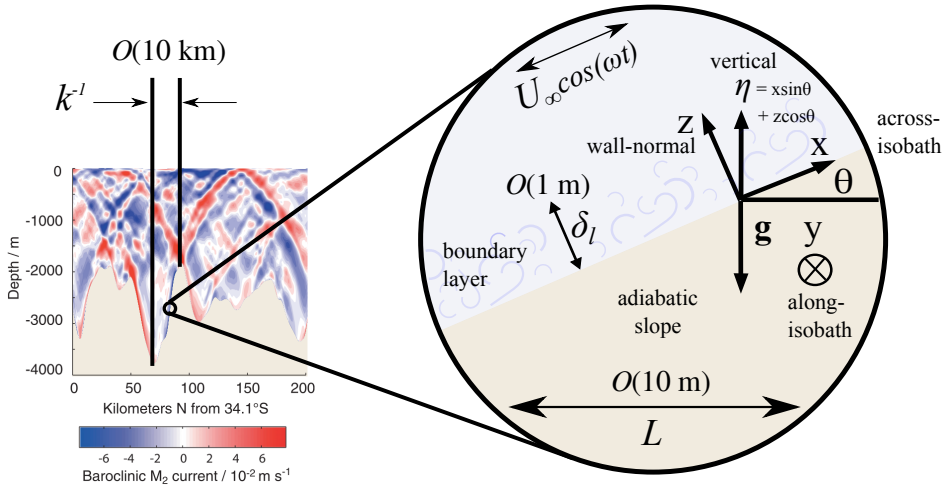

Figure 2-1: Illustration of BTBL length scales and geometry.
The M_2 tide velocity contour plot on the left is from Zilberman et al. (2009).

Figure 2-1 illustrates the scale separations between the horizontal length scale of baroclinic tide generation, k^{-1}, the excursion length scale of the tide, L, and the largest BTBL eddy scale, δ_l, that are assumed valid in this study. The contour plot of simulated M_2 baroclinic tide currents on the left of Figure 2-1 was copied from Zilberman et al. (2009) for illustrative purposes. The boundary layers investigated in this chapter apply to boundary layer flows on hydraulically smooth slopes where the excursion parameter

$$\mathcal{E} = kL, \tag{2.1}$$

where L is the tidal oscillation excursion length and k is the horizontal wavenumber of the topographic feature, is small, $\mathcal{E} \ll 1$. The excursion parameter $\mathcal{E}$ can representative of the ratio of net fluid advection by the barotropic tide to the topographic length and the nonlinearity of the baroclinic response to the barotropic forcing is proportional to the magnitude of $\mathcal{E}$ (Bell (1975a), Bell (1975b), Garrett and Kunze (2007), Sarkar and Scotti (2017)). The excursion length scale, L, is approximately the across-isobath distance between

the trajectory extrema in the inviscid problem, defined

$$L \sim \frac{U_\infty}{\omega}, \tag{2.2}$$

where U_∞ is the baroclinic tide amplitude parallel to the slope and ω is the tide frequency.

The scale separation described by $\mathcal{E} \ll 1$ is depicted in Figure 2-1. On hydraulically smooth slopes, with no bathymetric variations of higher wavenumber than k, the slope is approximately constant over the excursion length of the tide, L. While the generation of internal waves on length scales of k^{-1} produces baroclinic motions with vertical structure, within the narrow region of $\mathcal{O}(\delta_l)$ m from the slope the internal waves can be approximately represented as a locally irrotational inviscid heaving of isopycnals in the across-isobath direction. Irrotational flow is defined by a velocity field with zero curl. While the baroclinic tide has non-zero velocity curl, here the baroclinic tide is approximated as irrotational over length scales much smaller than the length scale of baroclinic tide generation. In this study, the assumption that there are no bathymetric variations in the along-isobath direction and $\mathcal{E} \ll 1$ permits the following approximations:

1. the slope is constant,

2. the internal waves generated by the interaction of the barotropic tide with undulating bathymetry of horizontal length scale k are modeled as an across-isobath oscillating pressure gradient body force that is invariant to translation, within a narrow region near the slope.

Steady boundary layers on an infinite slope

Before elaborating further on the oscillating boundary layers on adiabatic slopes, it is necessary to review the steady flows that arise wherever diffusive stratified flows encounter adiabatic slopes in the absence of imposed forces (e.g. tides, quasi-geostrophic mean flows, etc) other than the force of gravity and the restoring force of stratification. Motion arises because diffusive adiabatic sloping boundaries produce baroclinicity by tilting density surfaces parallel to the wall normal axis (the z axis in Figure 2-1), such that the angle θ separates

density surfaces from the hydrostatic pressure gradient in the vertical (the η axis in Figure 2-1) with the diffusive boundary layer. The baroclinicity produces vorticity in the along-slope, constant isobath direction (y axis in Figure 2-1), which in turn drives across-slope wall parallel flows with a net upslope transport. Phillips (1970) and Wunsch (1970) simultaneously derived analytical solutions for the laminar flows induced by the presence of sloping adiabatic boundaries, the former for the stationary reference frames and the latter for both stationary and rotating reference frames. Hereafter the stationary reference frame linear solution will be referred to as the steady boundary layer, SBL, and the rotating reference frame linear solution will be referred to as the rotating steady boundary layer, RSBL. Laboratory experiments have since validated both the SBL (Peacock et al. (2004)) and the RSBL (MacCready and Rhines (1991)) laminar flow solutions.

A peculiar feature of the RSBL solution is that for a given set of constant flow parameters (slope angle, Coriolis parameter, stratification, buoyancy diffusivity, & kinematic viscosity) the linear solution for the geostrophic flow field over a slope that does not vary in the along-isobath direction is unique (Wunsch (1970)). The solution specifies the magnitude and direction of the geostrophic flow over a slope as a function of the boundary layer conditions. However, it is well known that geostrophic flows over slopes in the ocean are not restricted to the unique solutions of Wunsch (1970). MacCready and Rhines (1991) resolved the conundrum by examining the RSBL initial value problem to determine an Ekman "shut down" time scale required for the formation of the RSBL and its unique geostrophic state. MacCready and Rhines (1991) defined Ekman layer shut down as an across-slope Ekman-type boundary layer transport that arises from an along-isobath geostrophic flow, which ceases or shuts down when it balances with buoyancy forces. The same phenomena is sometimes referred to as buoyancy arrest (Brink and Lentz (2010a)). Using experiments and theoretical arguments, MacCready and Rhines (1991) showed that on time scales less than the shut down time scale, the dynamics resemble that of Ekman boundary layers on slopes, in which the boundary layer transport is a response to the far field geostrophic flow, and on time scales greater than the shut down time scale the RSBL manifests.

Oscillating boundary layers on a slope

The addition of an oscillating, across-slope, body force to the SBL and RSBL gives rise to a class of boundary layers that, in various limits, collapse to familiar classical oscillating boundary layers (Stokes second problem, Stokes-Ekman layers, Stokes-buoyancy layers, etc) and describes the frictional interaction of baroclinic tide with a slope if the scale separations of Equation 2.1 is satisfied to a reasonable degree. Baidulov (2010) derived the linear solutions for the oscillating, stratified, viscous, and diffusive boundary layer in a stationary (not rotating) reference frame (hereafter the oscillating boundary layer, OBL) and found that the linear flow is a superposition of two evanescent modes. Baidulov (2010) noted that the phase of one of the boundary layer modes changes sign as the slope increases from subcritical to supercritical, where critical slope is defined by the slope angle θ_c that satisfies $\omega = N \sin\theta_c$ and N is the buoyancy frequency. The change in sign of the boundary layer solution mode is representative of the fact that the boundary layers share some of the dynamics of the parent flow (the larger scale internal wave field), which undergoes a change of sign of the group velocity of the radiated or reflected internal waves as the slope angle increases from subcritical to supercritical topography. At critical slope, the OBL and the far field flow resonate because the frequency of buoyant restoring force parallel matches that of the across-isobath velocity oscillation.

A commonly observed OBL flow feature is the formation and growth of gravitational instabilties produced by the upslope advection of relatively heavy water over relatively light water trapped at the boundary by friction, as depicted in diagram (a) of Figure 2-2. The energy source for OBL gravitational instabilities is the baroclinic tide, the same as for near boundary gravitational instabilities and overturning formed by critically reflecting internal waves (Dauxois and Young (1999)) and the nonlinear baroclinic tide generation at critical slope (Rapaka et al. (2013), Gayen and Sarkar (2011a), Sarkar and Scotti (2017)). However, gravitational instabilities at critical slope are formed by primarily inviscid nonlinearities in the baroclinic response to the barotropic tide (Dauxois and Young (1999)); whereas, in the OBL graviational instabilities are formed by viscous, insulating boundary conditions (Hart (1971)). OBL gravitational instabilities on extra-critical slopes have been observed in exper-

iments (Hart (1971)), and observed in OBLs in lakes associated with internal seiche waves (Lorke et al. (2005)) and internal gravity waves (Lorke et al. (2008)). Similar boundary layer gravitational instabilities have been observed in the flood (i.e. upslope) phase of estuarine tidal flows (Simpson et al. (1990), Chant and Stoner (2001), Geyer and MacCready (2014)), formed by a combination of bottom friction and the straining of horizontal buoyancy gradients over shallow finite topography, shown in diagram (*b*) of Figure 2-2.

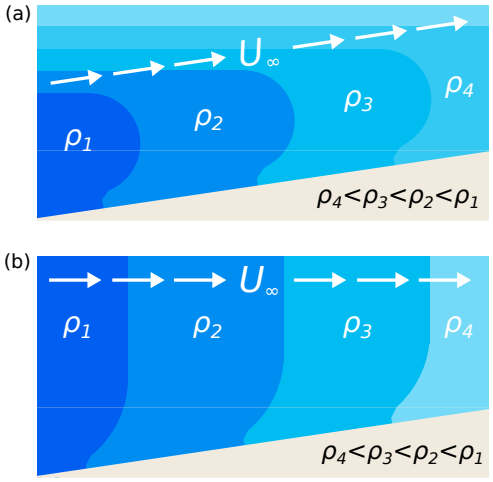

Figure 2-2: Boundary layer gravitational instability mechanisms.
Figure *(a)* depicts the density field during the upslope phase of an oscillating flow with viscous, adiabatic boundary conditions at the sloping wall. Figure *(b)* depicts the density field in a shallow estuarine flow during the flood phase of the tide, during which horizontal density gradient is strained as it stretches around finite topography. Both cases develop gravitationally unstable density (or buoyancy) gradients in the boundary layer.

Supercritical slope OBL laboratory experiments by Hart (1971) identified spanwise plumes and rolls (described by the streamwise, or across-slope vorticity component), associated with the periodic reversals of the density gradient, that qualitatively resembled the rolls that appeared in high Rayleigh number Couette flow experiments by Bénard and Avsec (1938), Chandra (1938), and Brunt (1951). Perhaps due to the similarity to the convection experiments, the rolls observed by Hart (1971) are often referred to as "convective rolls" although the term is misleading because it implies diabatic processes are at work; the gravitational instabilities, rolls, and overturns of interest in this study are locally adiabatic. Linear stability analyses by Deardorff (1965), Gallagher and A. Mercer (1965), and Ingersoll (1966), revealed that the observed growth of gravitationally unstable disturbances in high Rayleigh number

Couette flows is suppressed in the plane of the shear (the streamwise-vertical plane) by the shear (i.e. the suppression of the spanwise vorticity disturbances). However, they also found that the growth of disturbances in the spanwise-vertical plane (steamwise vorticity disturbances) is unimpeded by the shear and grows in the same manner as pure convection. It has since been established that streamwise (the across-isobath direction) vortices with axes in the direction of a mean shear flow (a.k.a. "rolls") can arise due to heating or centrifugal effects (Hu and Kelly (1997)).

The study of wave-driven turbulent boundary layers in stratifed flows on sloping bathymetry has been dominated by simulation-based studies of the critical slope wave reflection or generation problem (Gayen and Sarkar (2010a), Gayen and Sarkar (2011a), Gayen and Sarkar (2011b), Rapaka et al. (2013), Winters (2015), Chalamalla and Sarkar (2015)). Second-moment turbulence closure simulations of subcritical, hydraulically rough, OBLs at moderate Reynolds numbers by Umlauf and Burchard (2011) developed unstable buoyancy gradients and overturning during the upslope flow phase of the fully turbulent regime (turbulence throughout the entire phase of the oscillation). However, the results of their model indicated that mixing (irreversible buoyancy flux convergence) by the fully turbulent regime increases with slope angle, but is also relatively inefficient when compared with open ocean mixing processes, such as Kelvin-Helmholtz and Holmboe wave breaking. Umlauf and Burchard (2011) also found mixing efficiences substantially smaller than $\Gamma = 0.2$, the value typical of the open ocean (recall that Γ is equal to minus the buoyancy flux, or rate of conversion of turbulent kinetic energy into potential energy, divided by the dissipation rate of turbulent kinetic energy). The low mixing efficiencies and buoyancy flux convergence found by Umlauf and Burchard (2011) suggest that either the second-moment turbulence closure simulations did not adequately represent the boundary layer physics, or that stress-driven BTBLs (in which the production of turbulent kinetic energy arises from the frictional/adiabatic boundary conditions) are not efficient at mixing fluid at Prandtl numbers typical of the abyssal ocean.

Rotating, oscillating boundary layers on a slope

Linear solutions for the OBL in a rotating reference frame (hereafter the rotating oscillating boundary layer, ROBL) were derived by Thorpe (1987). Assuming laminar flow, the empirically tested shut down time scale of MacCready and Rhines (1991) (mentioned previously) indicates that if the ROBL oscillates at subinertial frequences, then the ROBL solution oscillates around the RSBL and its unique geostrophic flow, as in the solutions of Wunsch (1970) and Thorpe (1987). Therefore oscillations with shorter periods than the shut down time scale will generate Stokes-Ekman boundary layers (a.k.a. "pulsating Ekman layers," Munk et al. (1970), Weatherly et al. (1980), Salon and Armenio (2011)) in stratified flow on a sloping boundary.

Mid-latitude deep ocean observations by Aucan et al. (2006) and Klymak et al. (2008), coastal observations by Lentz and Trowbridge (1991) and Moum et al. (2004), and simulations by Slinn and Levine (1997), suggest density overturns and Stokes-Ekman -type dynamics are common features of ROBLs driven by the M_2 semidiurnal tide. Studies of ROBLs on sloping bathymetry tend to fall into one of two categories. The first category is comprised of theoretical and numerical studies of the dynamics of boundary layers that occur due to the reflection of remotely forced internal waves (Slinn and Riley (1996), Dauxois and Young (1999), Lamb (2014), Winters (2015)), where the resulting turbulent boundary layer is produced by nonlinearities on the scale of the internal waves (e.g. length scales of k^{-1} in Figure 2-1). The second category developed as the logical extension of the investigations of the RSBL (MacCready and Rhines (1991), Garrett (1991), Garrett et al. (1993), Trowbridge and Lentz (1991), Brink and Lentz (2010a)) to time dependent flows. The studies investigate ROBLs forced by low Rossby number along-slope (along-isobath) oscillations by employing turbulence models (e.g. turbulence closures of varying order, from zero-order eddy diffusivities to second-order Reynolds stress models) to represent the bulk characteristics of the boundary layer turbulence. Middleton and Ramsden (1996), Brink and Lentz (2010a) and Brink and Lentz (2010b) investigated the dynamics of buoyancy arrest (a balance between across-slope Ekman transport and the far field geostrophic flow due to the thermal wind created by the Ekman transport). The results of Brink and Lentz (2010b) indicate that, for

typical oceanic parameters, buoyancy arrest is unimportant for M_2 semidiurnal tides BTBLs. Ruan and Thompson (2016) studied the effect of a divergent along-slope oscillatory forcing (along-slope jets) on ROBLs, and found that in the near inertial to high frequency regimes (Rossby number unity or greater), the quasi-steady state Ekman theory is not applicable and that the boundary layer behavior is dominated by the the mean flow oscillation.

Objectives

Simulations of OBLs and ROBLs that fully resolve the near wall dynamics, down to the Kolmogorov scales, have not been performed, and observations of OBLs and ROBLs in the deep ocean are scarce and limited to one dimensional profiles of selected variables. The vast majority of high fidelity, wall resolving simulations are of critical or near critical OBLs and other "hot spots" of turbulence. The vast majority of studies of ROBL dynamics have sought to explain the low frequency, subinertial dynamics (ignoring the superinertial M_2 tide) by relying on turbulence models to represent the nonlinearities at the boundary. The gap in the literature suggests a need for wall resolving simulations of M_2 tide boundary layers on extra-critical slopes to answer a plethora of questions:

- Are the assumptions of the turbulence closures that are commonly used for ROBL studies justifiable? Are the boundary layers laminar, transitional, intermittent, or fully turbulent for typical ocean parameters?
- How do OBLs and ROBLs transition to turbulence?
- What might be the roll of mundane (extra critical) but omnipresent abyssal slope boundary layers in the global overturning circulation, i.e. how much buoyancy flux convergence occurs in M_2 tide boundary layers?

The objectives of this chapter are to 1) to determine if the boundary layers are laminar, intermittently turbulent, or fully turbulent for the portion of parameter space that pertains to frictional boundary layers forced by the M_2 tide on abyssal slopes, 2) estimate the irreversible mixing and diapycnal velocities / water mass transformation rate, and 3) estimate the boundary layer dissipation rate of turbulent kinetic energy that is likely to be observed by in-situ measurements.

This chapter is organized as follows. In the *Problem formulation* section the relevant governing equations and non-dimensional parameters for OBLs and ROBLs that satisfy the geometric constraint of Equation 2.1 are discussed. In *Linear Flow Solutions*, salient features of the linear laminar flows are reviewed to ascertain how the linear dynamics inform the analysis of the intermittently turbulent boundary layers. In the *Nonlinear Flow Solutions* section, the numerical methods for the direct numerical simulation of the boundary layers is reported and the statistical analysis of the simulated intermittently turbulent and fully turbulent boundary layers is discussed. In the *Discussion* the boundary layer simulations are compared to an observation and contextualized within the dynamical parameter space; and finally, in *Conclusions*, the chapter is summarized.

2.1 Problem formulation

The boundary layers examined in this study are created by the superposition of viscous/diffusive boundary conditions and a harmonic pressure gradient oscillation in the across-isobath (streamwise) x direction:

$$\partial_x \tilde{p}_\mathrm{d}(t) = -\mathrm{real}[A_\mathrm{d} i \mathrm{e}^{it}], \tag{2.3}$$

where A_d is a real dimensional amplitude of the dimensional across-isobath pressure gradient $\partial_x \tilde{p}_\mathrm{d}$. The total flow variables are denoted with tildes because the statistical analysis of the results is concentrated on the anomalies from the background flow. If the oscillatory pressure gradient is applied in the along-isobath (y) direction, such that the forcing of the flow is driven by $\partial_y \tilde{p}$, then gravity only acts directly on flow instabilities and turbulence, and not on the linear oscillations. That problem will not be examined in this thesis. However, the ROBL produces oscillations in the velocity and therefore produces transient along-isobath flows as the Ekman-like velocity spiral swings back and forth in response to an across-isobath oscillatory forcing.

2.1.1 Governing equations

Several geometric and physical approximations are invoked for the sake of tractibility and conceptual simplicity. The flow is approximated as Boussinesq: oceanic density variations are roughly $\mathcal{O}(10^{-2})$ (Talley (2011)); therefore, the incompressibility condition is justified, and Joule heating (increases of internal energy due to the viscous dissipation of mechanical energy) is neglected because, in water Kolmogorov scale of 1 cm, it is several orders of magnitude smaller than the other terms in the thermodynamic energy (buoyancy) equation (Chandrasekhar (1961)). The largest inaccuracies arising from the idealization of abyssal flow buoyancy as purely a function of temperature are most likely due to the linearization of nonlinearities in the equation of state for seawater, and possibly from the neglect of double diffusive processes (primarily salinity diffusion vs. thermal diffusion). The role of both phenomena to ocean mixing are poorly understood on a global scale (Gregg et al. (2018)); here they are neglected for simplicity.

A Cartesian coordinate system, rotated θ radians counterclockwise above the horizontal as in Figure 2-1, was chosen for analytical convenience. The x coordinate is referred to as the across slope (or streamwise) coordinate, oriented parallel to the surface of the slope and positive x points in the direction of the maximum rate of elevation gain / shallowing depth. The y coordinate is referred to as the along slope (or spanwise) coordinate; it is also oriented parallel to the surface of the slope but points along lines of constant elevation / depth. The z coordinate is the wall-normal (or transverse) coordinate, which is at angle θ from the vertical coordinate (the coordinate anti-parallel to the gravity). To distinguish between the slope-normal and vertical coordinates, the vertical coordinate (and vertical velocities, fluxes, etc) in the direction normal to Earth's surface will be denoted as η, such that $\eta = x\sin\theta + z\cos\theta$, also shown in Figure 2-1.

For the chosen approximations and coordinate system, the non-dimensional Cartesian form of the Boussinesq governing equations for conservation of mass, momentum, and ther-

modynamic energy for the flow are

$$\partial_x \tilde{u} + \partial_y \tilde{v} + \partial_z \tilde{w} = 0, \tag{2.4}$$

$$\mathrm{d}_t \tilde{u} = \frac{1}{\mathrm{Ro}}\tilde{v} - \partial_x \tilde{p} + \frac{1}{\mathrm{Re}_L}\big(\partial_{xx} + \partial_{yy} + \partial_{zz}\big)\tilde{u} + \mathrm{C}^2\tilde{b} + \Big(\mathrm{C}^2 + \frac{1}{\mathrm{Ro}^2} - 1\Big)\mathrm{real}[i\mathrm{e}^{it}], \tag{2.5}$$

$$\mathrm{d}_t \tilde{v} = -\frac{1}{\mathrm{Ro}}\tilde{u} - \partial_y \tilde{p} + \frac{1}{\mathrm{Re}_L}\big(\partial_{xx} + \partial_{yy} + \partial_{zz}\big)\tilde{v}, \tag{2.6}$$

$$\mathrm{d}_t \tilde{w} = -\partial_z \tilde{p} + \frac{1}{\mathrm{Re}_L}\big(\partial_{xx} + \partial_{yy} + \partial_{zz}\big)\tilde{w} + \mathrm{C}^2\tilde{b}\cot\theta, \tag{2.7}$$

$$\mathrm{d}_t \tilde{b} = \frac{1}{\mathrm{PrRe}_L}\big(\partial_{xx} + \partial_{yy} + \partial_{zz}\big)\tilde{b}, \tag{2.8}$$

where $\mathrm{d}_t = \partial_t + \tilde{\mathbf{u}} \cdot \nabla$ denotes the material derivative. The magnitude of the body force exerted on the streamwise momentum by the oscillating pressure gradient, the last term on the righthand side of the across-isobath (streamwise) momentum equation (equation 2.5) is set by a linear, inviscid, pressure-momentum-buoyancy balance that describes the heaving of isopycnals up and down the slope and will be discussed below in the *Oscillatory forcing* section. The tildes denote the total flow; the linear decomposition of the total flow is discussed in the *Variable decomposition* section.

Time, space, and the prognostic variables are non-dimensionalized as follows (subscript "d" denoting dimensional variables):

$$\mathbf{x} = \mathbf{x}_\mathrm{d}/L, \qquad \tilde{\mathbf{u}} = \tilde{\mathbf{u}}_\mathrm{d}/U_\infty, \qquad t = \omega t_\mathrm{d}, \qquad \tilde{p} = \tilde{p}_\mathrm{d}/U_\infty^2, \qquad \tilde{b} = \tilde{b}_\mathrm{d}/(LN^2\sin\theta), \tag{2.9}$$

where the reference density ρ_0 is absorbed into the mechanical pressure p_d such that it has units $\mathrm{J\,kg^{-1}}$. θ is the slope angle, rotated counterclockwise from horizontal. N^2 is the square of the buoyancy frequency (the frequency of the restoring force due to the stratification).

Even for the simplifications of Boussinesq flow and a slope that satisfies $\mathcal{E} \ll 1$, as well as the reduced range of the parameter space relevant to abyssal flows, the dynamical parameter space is vast. Since θ is dimensionless, the remaining relevant dynamical variables are $N, \omega, f, \nu, \kappa$, and U_∞, where f is the Coriolis parameter, ν is the kinematic viscosity coefficient, κ is the buoyancy diffusivity coefficient (approximately the thermal diffusivity), and Buckingham Π theorem posits that there are four relevant non-dimensional ratios. We

formulate the Π groups in terms of the Prandtl number Pr, the slope Rossby number Ro, the slope frequency ratio C, and Stokes layer Reynolds number Re. In this study, the Stokes layer Reynolds number is referred to in the analysis of the flow instead of the excursion length Reynolds number

$$\mathrm{Re}_L = \frac{U_\infty L}{\nu} = \frac{U_\infty^2}{\nu\omega}, \tag{2.10}$$

which naturally appears in the non-dimensional governing equations, because the Stokes layer Reynolds number is common in literature regarding oscillating boundary layers. The Prandtl and Stokes layer Reynolds numbers are defined as

$$\mathrm{Pr} = \frac{\nu}{\kappa}, \tag{2.11}$$

$$\mathrm{Re} = \frac{U_\infty \delta}{\nu} = \sqrt{2\mathrm{Re}_L}, \tag{2.12}$$

where κ is the molecular diffusion of buoyancy and ν is the kinematic viscosity of abyssal seawater, and where the Stokes' layer thickness is:

$$\delta = \sqrt{2\nu/\omega}. \tag{2.13}$$

The slope frequency ratio is defined as the ratio of the projection of the buoyant acceleration onto the across slope (x) direction (parallel to the forcing) to the acceleration of the oscillatory forcing

$$\mathrm{C} = \frac{N \sin\theta}{\omega}. \tag{2.14}$$

The slope frequency ratio was first identified as an important ratio for describing the boundary layer by Hart (1971) (who denoted it as Q, where $\mathrm{Q} = \mathrm{C}^2$), and the frequency ratio N/ω appears as an important measure of the role of stratification in the case of Stokes' second problem in a stratified flow (Gayen and Sarkar (2010b)). If the characteristic time scale of the shear is equivalent to the the tide period, ω^{-1}, then the ratio N^2/ω^2 is equivalent to the gradient Richardson number. However, the gradient Richardson number is indicative of the suppression, or lack thereof, of shear instability by buoyant restoring forces, and therefore has limited applicability to a flow which oscillates between stable and unstable buoyancy

gradients. In contrast, the slope frequency ratio C is indicative of the degree of resonance between the oscillation body forcing and the buoyant restoring force.

Finally, the fourth non-dimensional Π ratio is slope Rossby number is

$$\mathrm{Ro} = \frac{\omega}{f \cos\theta}, \tag{2.15}$$

which indicates the ratio of the influence of planetary vorticity (projected onto the wall normal direction) relative to vorticity with a characteristic time scale of the tide period, ω^{-1}. For the finite Rossby number cases examined, ω is the M_2 tide frequency, the Coriolis parameter, f, is 10^{-4} s^{-1}, and the range of slope angles investigated are within $0 < \theta \leq 14°$. Within this subset of parameters, the slope Rossby number is approximately 1.4 for all of the rotating reference frame cases.

The mean slope of the seafloor, after filtering with a 60-km Gaussian filter and interpolating on a 0.5° grid, ranges between 0 and 5.7° across the global ocean seafloor (Becker and Sandwell (2008)). However, the mean slope commonly exceeds 2.9° on the flanks of seafloor spreading ridges (Becker and Sandwell (2008)). Slope angles up to 14° are investigated in this study for completeness, and high angle slope angles can occur over small scale features with horizontal length scales not much larger than the excursion length of the tide. Deep sediment thickness may be indicative of regions where the abyssal slopes are hydraulically smooth. In particular, the lower ends of continental slopes tend to be covered in layers of sediment deeper than 500 m (Goff and Arbic (2010)), which suggests that the boundary layers in this study may be observed there.

2.1.2 The oscillatory forcing

It follows from the assumption of no topographic variation on horizontal length scales less than k^{-1} and small excursion parameter $\mathcal{E} \ll 1$, that the deflection of the barotropic tide by a bathymetric feature can be approximated as a constant slope on length scales of $\mathcal{O}(L)$. This permits the representation of the baroclinic response to the barotropic tidal forcing, within a region of length scale $\mathcal{O}(\delta)$, to be approximated by a wall parallel body forcing in the x direction as indicated by the wall parallel oscillating velocity in figure 2-1. Within

a slope adjacent control volume, with each dimension of scale $\mathcal{O}(\delta)$, the baroclinic tide is a locally irrotational oscillating body force that heaves isopycnals up and down the slope, such that the oscillations of the velocity and buoyancy fields are 90° out of phase, similar to internal seiche waves.

The inviscid, linear form of the governing equations (Equations 2.4-2.8) that describe that inviscid heaving of isopycnals up and down the slope is:

$$\partial_t \tilde{u} = \frac{1}{\mathrm{Ro}}\tilde{v} + \mathrm{C}^2\tilde{b} + \Big(\mathrm{C}^2 + \frac{1}{\mathrm{Ro}^2} - 1\Big)\mathrm{real}[i\mathrm{e}^{it}], \tag{2.16}$$

$$\partial_t \tilde{v} = -\frac{1}{\mathrm{Ro}}\tilde{u}, \tag{2.17}$$

$$\partial_t \tilde{b} = -\tilde{u}, \tag{2.18}$$

where the wall normal momentum (w) equation reduces to a diagnostic equation for the pressure due to the impermeability boundary condition at the wall and the incompressiblity condition. The dimensional amplitude of the pressure gradient, A_d in Equation 2.3, appears in a non-dimensional form in Equation 2.16:

$$A = -\frac{A_\mathrm{d}}{U_\infty \omega}, \tag{2.19}$$

$$= \Big(\mathrm{C}^2 + \frac{1}{\mathrm{Ro}^2} - 1\Big), \tag{2.20}$$

where the righthand side of Equation 2.20 is the only value of A that satisfies non-trivial solutions of Equations 2.16 through 2.18. The solutions to Equations 2.18-2.18 are

$$\tilde{u} = -\mathrm{real}[\mathrm{e}^{it}], \qquad \tilde{v} = -\frac{1}{\mathrm{Ro}}\mathrm{real}[i\mathrm{e}^{it}], \qquad \tilde{b} = -\mathrm{real}[i\mathrm{e}^{it}]. \tag{2.21}$$

For the non-rotating, $\mathrm{Ro} \to \infty$ regime, the streamwise flow velocity is directed down the pressure gradient and the isopycnals are advected by the momentum. In the finite Ro regime, the Coriolis force deflects momentum along the oscillating pressure gradient and along the slope, forming tidal ellipses. In the limit rapid rotation, $\mathrm{Ro} \to 0$, the inviscid flow reduces to inertial oscillations.

Resonance conditions

The magnitude of the body force term in equation 2.16 (the last term on the right hand side), vanishes if the critical slope condition

$$\mathrm{C}^2 + \frac{1}{\mathrm{Ro}^2} - 1 = 0, \tag{2.22}$$

is satisfied. If Equation 2.22 is valid, the slope is referred to as "critical" and the dynamics of the inviscid baroclinic response to the barotropic forcing are no longer described by Equations 2.18-2.18. The unusual resonance condition of Equation 2.22, in which the forcing vanishes at critical slope, is a consequence of the locally irrotational flow assumption (zero curl of the velocity field) inherent in the inviscid flow described by Equations 2.18-2.18. However, on critical slopes, the energy of the inviscid baroclinic tide is tightly focused into narrow beams that follow the curvature of the bathymetry (Balmforth et al. (2002)), therefore assumption of locally irrotational flow breaks down at critical slope, even on small length scales. To properly describe inviscid internal tide dynamics at critical slope in a semi-infinite domain, additional terms that account for the rotational nature of the velocity field should be included in Equations 2.18-2.18, but that is not done here because the goal of this study is to investigate extra-critical slope boundary layer dynamics. However, the conditions in Equation 2.22 are exactly the same definition of critical slope as used in internal wave theory:

$$\tan\theta_c = \sqrt{\frac{\omega^2 - f^2}{N^2 - \omega^2}}, \tag{2.23}$$

where θ_c is the critical slope angle. To reveal the relationship between equations 2.22 and 2.23, let slope angle $\theta \neq \theta_c$, such that the non-dimensional across-slope body force amplitude $A \neq 0$:

$$\mathrm{C}^2 + \frac{1}{\mathrm{Ro}^2} - 1 = A, \tag{2.24}$$

where A is the non-dimensional across-slope body force amplitude. Equation 2.24 can be rearranged by expanding the definitions of the Rossby number and slope frequency ratio

rearranging to obtain

$$\tan\theta = \sqrt{\frac{\omega^2(1+A) - f^2}{N^2 - \omega^2(1+A)}}. \tag{2.25}$$

Therefore the criticality condition in equation 2.22 is identical to the criticality condition defined by the slope parameter ϵ from internal wave theory:

$$\epsilon = \frac{\tan\theta}{\tan\theta_c}, \tag{2.26}$$

where criticality states are defined:

$$\begin{aligned}
&\text{if} \quad A < 0 \quad \text{then} \quad \epsilon < 1 \quad \rightarrow \quad \theta \text{ is subcritical,} \\
&\text{if} \quad A = 0 \quad \text{then} \quad \epsilon = 1 \quad \rightarrow \quad \theta \text{ is critical,} \\
&\text{if} \quad A > 0 \quad \text{then} \quad \epsilon > 1 \quad \rightarrow \quad \theta \text{ is supercritical.}
\end{aligned}$$

In this the prefix extra is meant to refer its definition as "outside," therefore extra-critical slopes refers to subcritical or supercritical slopes that are not near-critical.

2.1.3 Boundary conditions

At the solid boundary, the boundary conditions on the total velocity are no-slip and impermeability

$$\tilde{\mathbf{u}} = 0, \tag{2.27}$$

and the boundary conditions on the total buoyancy is the adiabatic condition:

$$\partial_z \tilde{b} = 0. \tag{2.28}$$

At $z \to \infty$, the velocity boundary conditions are the oscillatory solutions for the inviscid flow and zero flow in the wall normal direction:

$$\tilde{u} = -\text{real}[\mathrm{e}^{it}], \qquad \tilde{v} = -\frac{1}{\text{Ro}}\text{real}[i\mathrm{e}^{it}], \qquad \tilde{w} = 0. \tag{2.29}$$

The buoyancy field at $z \to \infty$ has two components, the inviscid oscillation and the constant background stratification:

$$\tilde{b} = x + z\cot\theta - \text{real}[i\text{e}^{it}]. \tag{2.30}$$

2.1.4 Variable decomposition

To solve the viscous, diffusive governing equations for either the linear (analytical) or non-linear (numerical) forms, the flow is decomposed into components which sum to satisfy the governing equations and boundary conditions on the total flow. The decomposition has three components:

1. a steady, hydrostatic, constant stable stratification background flow that includes an along slope geostrophic velocity at finite Rossby number and does not satisfy the boundary conditions at the wall;

2. a steady boundary layer perturbation (the Phillips (1970) and Wunsch (1970) solutions) that, when summed with component 1, satisfies the boundary conditions at the wall ($z = 0$) and steady part of the flow in the far field; and

3. a velocity/buoyancy oscillation that satisfies adiabatic, no-slip, impermeable boundary conditions at the wall and satisfies the inviscid oscillation equations (the time dependent components of Equations 2.29 and 2.30) in the far field.

The sum of components 1 and 2 constitutes the SBL and RSBL for stationary and rotating reference frames, respectively, while the sum of all three components constitutes the OBL and ROBL in the same manner. Thus total velocity and buoyancy fields are decomposed into three components that when summed together satisfy Equations 2.4-2.8 and 3.58-2.30. To distinguish the components, let "H" denote the hydrostatic (and possibly geostrophic) component 1, let "S" denote the steady component 2, and let "O" denote the oscillating

component:

$$\tilde{\mathbf{u}}(x,y,z,t) = \mathbf{u}_{\mathrm{H}} + \mathbf{u}_{\mathrm{S}}(z) + \mathbf{u}_{\mathrm{O}}(x,y,z,t), \tag{2.31}$$

$$\tilde{b}(x,y,z,t) = b_{\mathrm{H}}(x,z) + b_{\mathrm{S}}(z) + b_{\mathrm{O}}(x,y,z,t), \tag{2.32}$$

$$\tilde{p}(x,y,z,t) = p_{\mathrm{H}}(x,z) + p_{\mathrm{S}}(z) + p_{\mathrm{O}}(x,y,z,t). \tag{2.33}$$

The hydrostatic component of the buoyancy field is merely the background stratification in the rotated coordinate system, $b_{\mathrm{H,d}}(x_{\mathrm{d}}, z_{\mathrm{d}}) = N^2(x_{\mathrm{d}} \sin\theta + z_{\mathrm{d}} \cos\theta)$ in dimensional form, and the hydrostatic velocity field is zero everywhere except for the finite Rossby number flow regime, in which case it is the along-slope geostrophic velocity that arises from the across-isobath pressure gradient. The buoyancy frequency N is defined in the same manner as convention,

$$N^2 = -\frac{g}{\rho_0}\partial_\eta \rho_{\mathrm{H}} = \partial_\eta b_{\mathrm{H}}, \tag{2.34}$$

where η denotes the vertical position coordinate, g is Earth's gravitational acceleration (assumed constant), and ρ is the density anomaly corresponding to the constant stable stratification, and ρ_0 is the constant reference density from which the density anomalies are defined.

Figure 2-3 shows two examples of the decomposition of the linear solutions, which are derived in Appendix A. The buoyancy field decomposition is shown at two different values of slope frequency ratio $\mathrm{C} = N \sin\theta/\omega = 1/2, 3/2$ (equivalent to $\epsilon = 1/2, 3/2$ for $\mathrm{Ro} \to \infty$) in the top and bottom rows, respectively. The first column of plots in Figure 2-3 shows a Eulerian perspective of the total buoyancy field $\tilde{b}$, the second column shows the hydrostatic background component b_{H}, the third column shows the steady boundary layer component b_{S}, and the fourth column shows the oscillating component b_{O}.

The steady and oscillating flow components can be considered as anomalies to the hydrostatic flow component that ensure the satisfaction of frictional and diffusive boundary conditions at the wall and inviscid oscillations far from the wall. It is analytically and

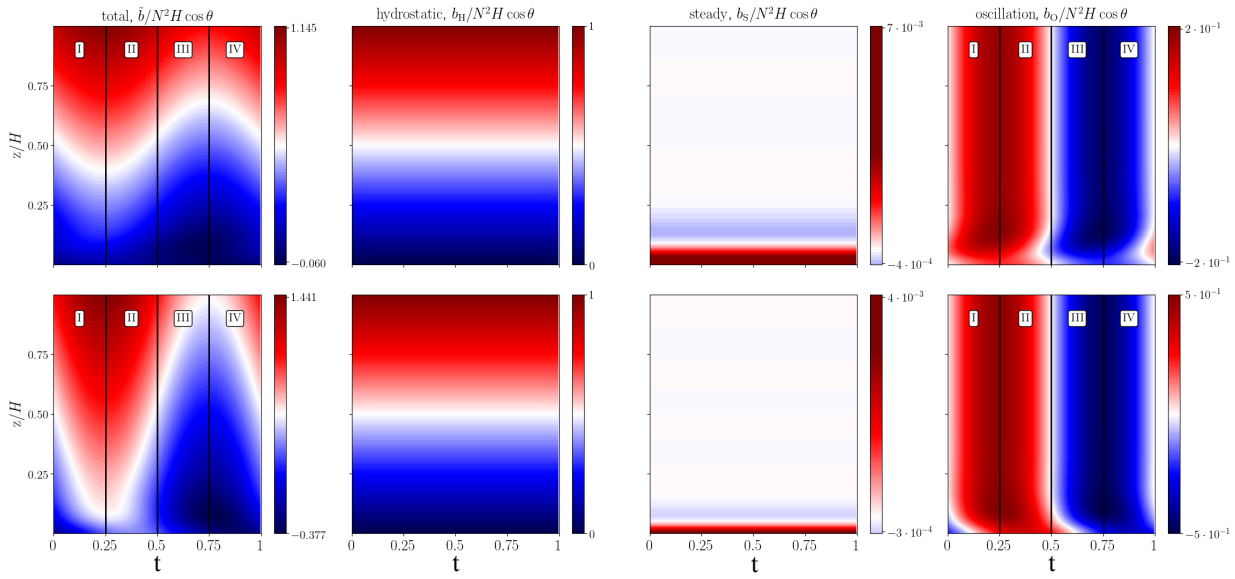

Figure 2-3: The linear decomposition of the total buoyancy field solutions. The top row shows solution components for a subcritical slope flow (C = 1/2) and the bottom row shows solution components for a supercritical slope flow (C = 3/2). In the oscillating components, four phases of the oscillation are marked with roman numerals: I) decelerating upslope flow, II) accelerating downslope flow, III) decelerating downslope flow, and IV) accelerating upslope flow.

numerically convenient to solve for the anomalies together, such that

$$\mathbf{u}(x,y,z,t) = \tilde{\mathbf{u}}(x,y,z,t) - \mathbf{u}_{\mathrm{H}} = \mathbf{u}_{\mathrm{S}}(z) + \mathbf{u}_{\mathrm{O}}(x,y,z,t), \tag{2.35}$$

$$b(x,y,z,t) = \tilde{b}(x,y,z,t) - b_{\mathrm{H}}(x,z) = b_{\mathrm{S}}(z) + b_{\mathrm{O}}(x,y,z,t), \tag{2.36}$$

$$p(x,y,z,t) = \tilde{p}(x,y,z,t) - p_{\mathrm{H}}(x,z) = p_{\mathrm{S}}(z) + p_{\mathrm{O}}(x,y,z,t), \tag{2.37}$$

because the removal of the hydrostatic background flow removes the inhomogeneity in the across-slope direction and permits periodic solutions for $\mathbf{u}$ and b. There are no magnitude restrictions for the anomalies defined in Equations 2.35, 2.36, and 2.37.

2.2 Linear flow solutions

The linear analytical solutions contain a wealth of information pertaining to the laminar, disturbed laminar, and intermittently turbulent regimes (i.e. low to moderate Reynolds

number flows) that are investigated numerically in this study. The oscillating components of the linearized forms of Equations 2.4-2.8, with no variation in the across-isobath (x) or along-isobath (y) directions, satisfy

$$\partial_t u = \frac{1}{\mathrm{Ro}} v + \frac{1}{\mathrm{Re}_L} \partial_{zz} u + \mathrm{C}^2 b + \left(1 - \frac{1}{\mathrm{Ro}^2} - \mathrm{C}^2\right) \mathrm{real}[i\mathrm{e}^{it}], \tag{2.38}$$

$$\partial_t v = -\frac{1}{\mathrm{Ro}} u + \frac{1}{\mathrm{Re}_L} \partial_{zz} v, \tag{2.39}$$

$$\partial_t b = -u + \frac{1}{\mathrm{PrRe}_L} \partial_{zz} b, \tag{2.40}$$

where the wall normal momentum vanishes by conservation of mass, and the wall normal momentum equation again reduces to a diagnostic equation for the pressure field. Note that the tildes have been dropped because Equations 2.38-2.40 govern the anomalies described by Equations 2.35-2.37. Equations 2.38-2.40 can be expressed as a single, separable high order inhomogeneous partial differential equation and subsequently solved for the linear OBL ($\mathrm{Ro} \to \infty$, solved by Baidulov (2010)) or the linear ROBL solutions (solved by Thorpe (1987)). However, Thorpe (1987) did not provide the full derivation of the linear ROBL solution. The solutions to the linear ROBL are provided in Appendix A (in a form that also readily collapses to the $\mathrm{Ro} \to \infty$ regime) to aid the reproducibility of the results: the sum of the linear solutions and small amplitude Gaussian noise serve as initial conditions for the numerical simulations in this study.

2.2.1 Phase regimes

The linear OBL/ROBL solutions are superpositions of 2/3 evanescent modes, respectively, and the particular solutions that satisfy the inviscid oscillations at $z \to \infty$. The non-dimensional imaginary and real components of the wall normal $e-$folding scales of each mode of the buoyancy solutions are shown in the top row of Figure 2-4 and the non-dimensional amplitude of each mode is shown in the bottom row. Each jth mode takes the form

$$u_j \sim \mathrm{e}^{-m_j z + it}, \tag{2.41}$$

$$b_j \sim i\mathrm{e}^{-m_j z + it}. \tag{2.42}$$

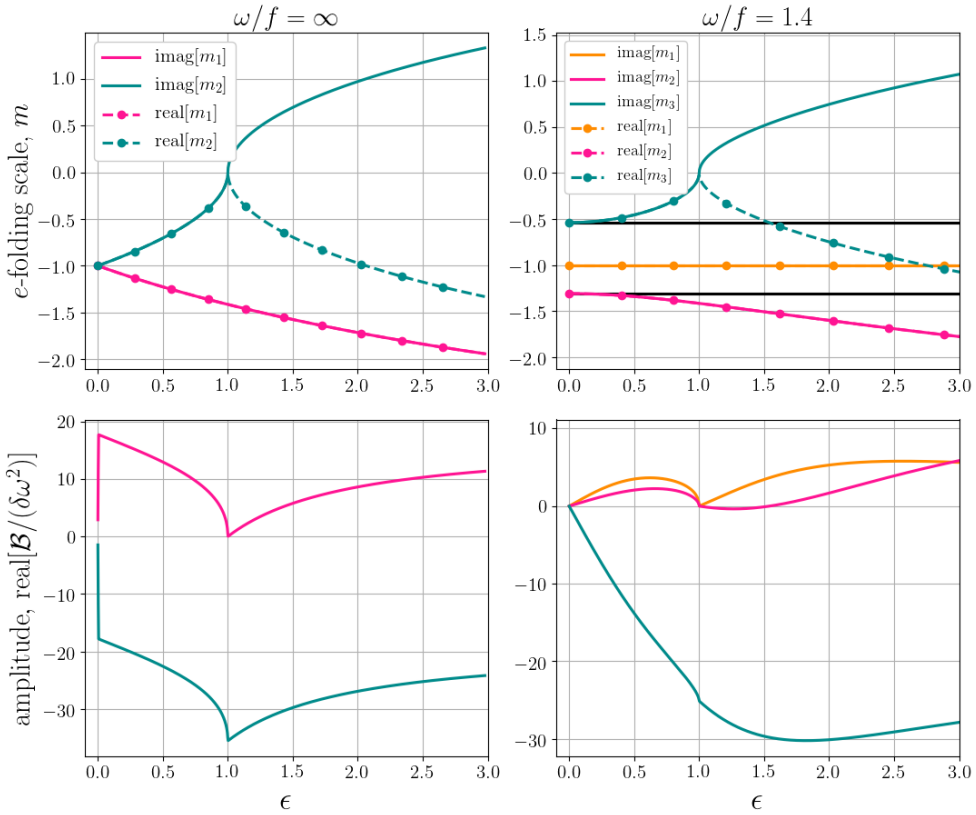

Figure 2-4: OBL/ROBL linear solution components.
Top row: the non-dimensional e-folding scales as a function of the slope parameter ϵ for non-rotating (*top left*) and rotating (*top right*) reference frames. The e-folding scales, denoted by m, are non-dimensionalized by $\delta = \sqrt{2\nu/\omega}$. The solid black lines on the rotating case e-folding scale plot are the Stokes-Ekman layer e-folding scales, $\sqrt{2\nu/|\omega \pm f|}$. *Bottom row:* the non-dimensional solution component amplitudes for the linear buoyancy solutions. The sharp pinch towards the origin in the non-rotating solution amplitudes (*bottom left*) corresponds to an asymptote as $\theta \to 0$.

The column of plots on the left of Figure 2-4 show the the OBL solutions, and the column of plots on the right show the ROBL solutions. The e-folding scales are non-dimensionalized by the Stokes layer thickness $\delta = \sqrt{2\nu/\omega}$ and the amplitude of the real component of buoyancy mode amplitudes $\mathcal{B}$ are non-dimensionalized by the Stokes layer thickness and square of the tide frequency.

The imaginary components of the mode e-folding scales, shown in Figure 2-4 as the solid lines in the plots of the top row, correspond to the boundary layer phase shifts as function of z_d in the OBL/ROBL solutions. As the ϵ is increased to greater than one, the sign of one mode's imaginary e-folding scale (the dark cyan colored lines for both OBL and ROBL plots)

changes sign, representing a shift in the solution mode from leading the far field oscillation to lagging the far field oscillation. The change in the sign of the phase shift in the solutions are visible in Figure 2-3, where the outer boundary layer buoyancy leads the far field oscillation in the subcritical slope OBL case (top row) and the entire boundary layer buoyancy lags the far field oscillation in the supercritical slope OBL case (bottom row). The real parts of the mode e-folding scales increase with increasing ϵ, which indicates that the linear boundary layer thickness decreases with slope parameter.

The boundary layer phase shifts also cause velocity "overshoots" which are defined as boundary layer velocities that exceed the maxima/minima of the far field velocity, known as Richardson's annular effect (Richardson and Tyler (1929)). Analogous to how diffusion breaks geostrophic balance in an Ekman layer, the overshoots that occur in the OBL and ROBL happen because the diffusive boundary layer breaks the pressure-buoyancy-momentum balance of the heaving flow. The overshoots occur because the decay rate of the boundary layer (set by the real part of the m) is the same magnitude as the phase shift (set by the imaginary part of the m). The boundary layer velocity overshoots in the linear solutions are interesting because they bear some resemblance to the tight beams of internal wave group velocity that propagate away from critical slopes (Balmforth et al. (2002), Gayen and Sarkar (2011b)). However, the boundary layer overshoots here are produced by linear viscous/diffusive processes, whereas the overshooting group velocity of Balmforth et al. (2002) Gayen and Sarkar (2011b) arises from largely inviscid dynamics on the scale of baroclinic tide generation.

At $\epsilon \to 0$ the normalized imaginary e-folding scales of the OBL (top left, Figure 2-4) collapse to -1, the imaginary e-folding scale for the Stokes second problem, and the normalized imaginary e-folding scales of the ROBL (top right, Figure 2-4) collapse to $\sqrt{2\nu/|\omega \pm f|}$, the imaginary e-folding scales for the two modes of the linear Stokes-Ekman layer (depicted as black lines). The amplitude of the buoyancy modes of both sets of solutions vanish as $\epsilon \to 0$, as shown in the bottom row of Figure 2-4.

The contour plots of Figure 2-5 show two sets of linear OBL solutions for the total velocity, total shear, and total buoyancy for $\mathrm{Ro} \to \infty$ and $\mathrm{C} = 1/2$ (top row, subcritical) and $\mathrm{C} = 3/2$ (bottom row, supercritical). The far field ($z/H \to 1$) velocity oscillates as -cos(t) and the

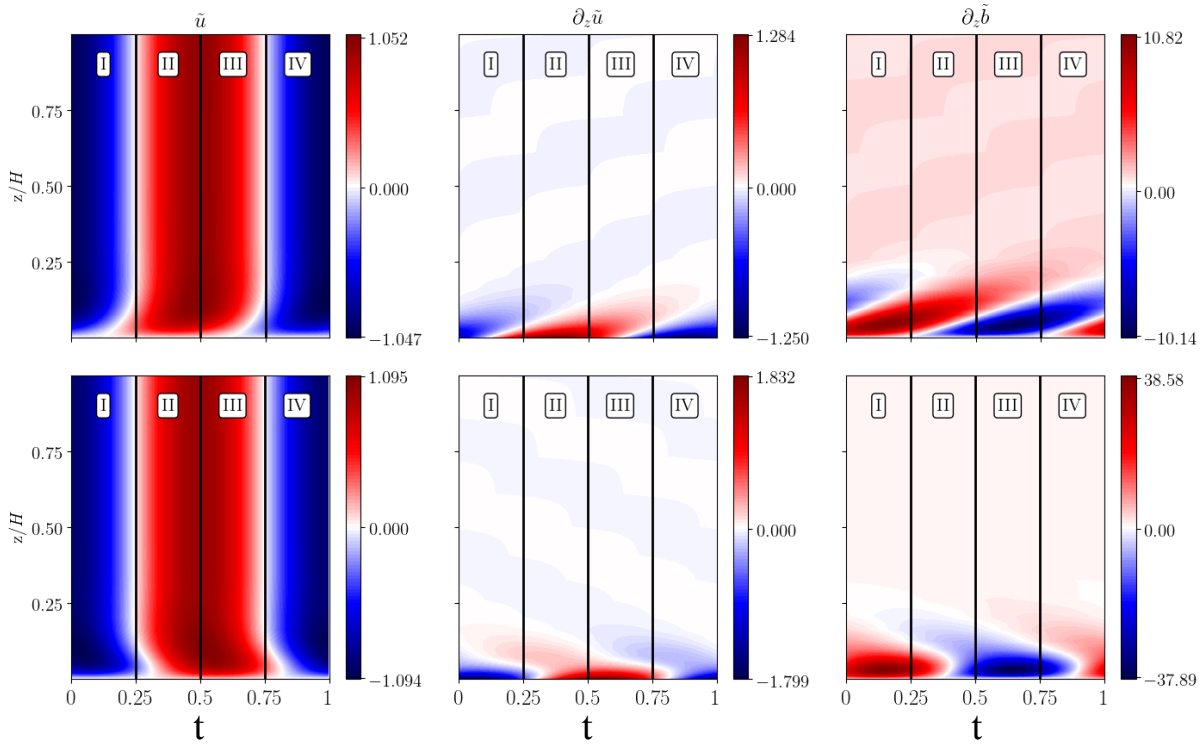

Figure 2-5: Linear solutions for velocity, shear, and stratification.
The top row is for subcritical, non-rotating solutions (C = 1/2, Ro $\to \infty$) and the bottom row is for supercritical, non-rotating solutions (C = 3/2, Ro $\to \infty$). For Ro $\to \infty$, C is equivalent to the slope parameter $\epsilon = \tan\theta / \tan\theta_c$. Plotted are exact solutions to the linearized forms of Equations 2.5-2.8, assuming no variations in x (the across-isobath direction) and no variations in y (the along-isobath direction).

far field buoyancy oscillates in tandem with the far field oscillating acceleration as $\sin(t)$. Although the velocity and buoyancy fields change continuously in time, one can identify four dynamically distinct phase regimes throughout the phase of the oscillation, labeled by numerals I-IV in Figure 2-5. The flow regimes by phase are:

I. $0 \leq$ t $<$ 0.25: the far field velocity reaches its downslope maximum and begins to decelerate (accelerate upslope), and relatively light buoyancy begins to be advected downslope.

II. $0.25 \leq$ t $<$ 0.5: the far field velocity changes sign and moves upslope while accelerating upslope, and the relatively light far field buoyancy is reduced.

III. $0.5 \leq$ t $<$ 0.75: the far field velocity reaches its upslope maximum and begins to

decelerate (accelerate downslope), and relatively heavy buoyancy begins to be advected upslope. Note that for both subcritical and supercritical flows, the boundary layer stratification is negative in this regime.

IV. $0.75 \leq \mathrm{t} < 1$: the far field velocity changes sign and moves downslope while accelerating downslope, and the relatively heavy far field buoyancy is reduced.

2.2.2 Gravitational instability

While both the SBL and RSBL feature steady, laminar baroclinic motions driven by the misalignment of the hydrostatic pressure field and the diffusion of the adiabatic boundary condition on the density field, it can be shown both are always gravitationally stable (the vertical buoyancy gradient is never negative):

$$\partial_\eta \tilde{b} = 1 - \cos^2\theta \mathrm{e}^{-\eta/\delta_\mathrm{S}} \sqrt{2} \sin\left(\frac{\eta}{\delta_\mathrm{S}} + \frac{\pi}{4}\right) \geq 0, \tag{2.43}$$

where η is the vertical coordinate ($0 \leq \eta < \infty$) and δ_S is the SBL/RSBL boundary layer thickness (Phillips (1970) and Wunsch (1970)):

$$\delta_\mathrm{S} = \left(\frac{f^2 \cos^2\theta}{4\nu^2} + \mathrm{Pr}\frac{N^2 \sin^2\theta}{4\nu^2}\right)^{-1/4} \tag{2.44}$$

However, as one might infer from the linear stratification solutions for the subcritical and supercritical OBL solutions above in Figure 2-5, the oscillating flow creates gravitationally unstable buoyancy gradients when denser fluid is advected over lighter fluid during portions of the oscillation period (in the entirety of phase regime III in Figure 2-5 in particular). Decomposing condition $\delta_\eta \tilde{b} < 0$ into the linear flow components in Equation 2.32 and rearranging yields

$$\partial_\eta b_\mathrm{H} + \partial_\eta b_\mathrm{S} < -\partial_\eta b_\mathrm{O}, \tag{2.45}$$

which, if satisfied, indicates that the minimum necessary condition for gravitational instabilities to occur at some point in time and space throughout the oscillation. For a gravitational instability to grow, the negative buoyancy gradient must be negative enough to overcome

resistance from friction. Applying equation 2.45 to the linear solutions (Appendix A) yields

$$1 < \frac{L}{\delta_b} \cot\theta \tag{2.46}$$

where δ_b is a vertical boundary layer buoyancy gradient length scale and L is the excursion length. There is no obvious choice of δ_b in the linear solutions shown in Appendix A, where there are two or three boundary layer length scales for non-rotating and rotating flows, respectively. Equation 2.46 can be geometrically interpreted as a measure of the (slope parallel) excursion length divided by the (wall normal) diffusive length scale for buoyancy if both length scales are projected onto the horizontal direction. Equation 2.46 is an approximate measure of the boundary layer momentum deficit that causes the inviscid heaving in the far field to advect fluid a greater distance than the near wall, low momentum flow. Equation **??** is a scaling for the estimation of the minimum criteria for the formation gravitational instabilities in laminar, disturbed laminar or possibly the intermittently turbulent regime, but may not be valid for high Reynolds number, fully turbulent flows, in which the boundary layer buoyancy gradients are likely to be eroded by the turbulence.

A characteristic boundary layer Rayleigh number and a ratio of the time scale of the growth of an instability to the period of the oscillation are required to estimate the minimum (quasi-steady) conditions for the *growth* of gravitational instabilities. However, the linear solutions do not readily yield a single boundary layer bouyancy gradient length scale. Let $\delta_b \sim \delta = \sqrt{2\nu/\omega}$, so that the time-dependent boundary layer Rayleigh number is defined

$$\mathrm{Ra}(t) = \frac{\delta^4 N^2}{\nu\kappa} \partial_\eta \tilde{b}(t), \tag{2.47}$$

$$= \frac{4\mathrm{Pr} N^2}{\omega^2} \partial_\eta \tilde{b}(t), \tag{2.48}$$

which only applies when $\partial_\eta \tilde{b}(t) < 0$. Assuming that the graviational instability in the boundary layer is physically similar to that of Rayleigh-Bénard instability in the case of one rigid and one stress-free boundary, then the critical Rayleigh number for the boundary layer is $\mathrm{Ra_c} \approx 1100$ (Chandrasekhar (1961)). For the chosen fluid properties, $\mathrm{Ra_c} \approx 1100$ corresponds to a critical buoyancy gradient of $\partial_\eta \tilde{b} \approx -5.4$.

To estimate the graviationally stability of the flow without explicitly accounting for the time dependence of the basic state (the quasi-steady assumption), the basic state of the flow cannot change more rapidly than the growth rate of a gravitational instability. If the instabilities are "slowly modulated" by the basic state Davis (1976)), the quasi-steady assumption is reasonable for stability analysis. The dimensional instantaneous growth rate of a gravitational instability can be estimated as

$$\sigma = \text{imag}\Big[\sqrt{\partial_\eta \tilde{b} N^2}\Big]. \tag{2.49}$$

If the basic state oscillation is slow relative to the growth of gravitational instabilities then

$$\left|\frac{\omega}{\sigma}\right| \ll 1. \tag{2.50}$$

and the modulation by the basic state is sufficiently slow for the growth of gravitational instabilities. If $\text{Ra}_\text{c} \approx 1100$, then $|\omega/\sigma| = 0.06$, therefore the quasi-steady assumption is reasonable within the parameter space of interest.

The minimum normalized buoyancy gradient of the ROBL linear solutions (holding $\text{Pr} = 1$, $f = 10^{-4}$, $N = 10^{-3}$, and $\omega = 1.4 \cdot 10^{-4}$ constant) is plotted in Figure 2-6 as a function of slope parameter and Reynolds number. The blue contour outlines $\min[\partial_\eta \tilde{b}(z,t)] = -5.4$ for both the OBL (the plot on the left) and the ROBL (the plot on the right). Note that the minimum boundary layer buoyancy gradient is less than zero for all Re and ϵ (except for at the origin) and that the minimum boundary layer buoyancy gradient is increasingly negative with increasing Reynolds number and with increasing slope parameter. The asymptote at $\epsilon = 1$ is an artifact of the linear solution breakdown near critical slope, where Equations 2.16-2.18) no longer serve as an adequate model of the oscillatory forcing by the baroclinic tide generation. The ϵ axis between the OBL and ROBL flows changes because rotation alters the angle of critical slope (both plots show $0 < \theta \leq 16°$).

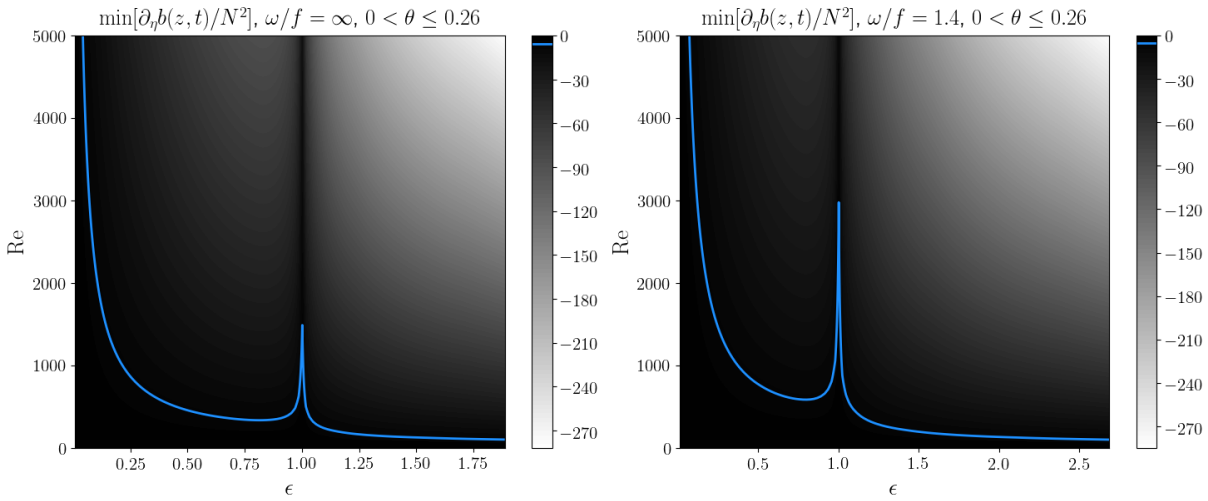

Figure 2-6: Total buoyancy gradient minima.
Both plots show the minimum value (in both time and space) of the the linear solution vertical buoyancy gradient, non-dimensionalized by N^2. Although the non-rotating reference frame case ($f = 0$, *left*) and the rotating reference frame case (*right*) appear to have a similar structure they do not overlay identically. Notice that the minimum is negative for the entire range of slope parameters $\epsilon = \tan\theta / \tan\theta_c$ and Reynolds numbers that are plotted to graphical accuracy. The blue lines correspond to a Rayleigh number of 1100.

2.3 Nonlinear flow solutions

2.3.1 Numerical implementation

The flow anomalies, as defined by equations 2.35 and 2.36, are discretized to satisfy periodic boundary conditions in the wall parallel directions via Fourier spectral bases in the across-isobath (x) and along-isobath (y) directions. Periodicity is not merely numerically convienent; it also eliminates the need to prescribe buoyancy forcing ("restratification") because the oscillating flow can advect the background field to gain or lose buoyancy. The boundary layer buoyancy can only reach steady state homogenization if the turbulence is able to consistently mix enough fluid every period. The background buoyancy gradient enters the buoyancy anomaly equation through the advection of background buoyancy by the anomalous velocity field term,

$$\mathbf{u} \cdot \nabla b_{\mathrm{H}} = u + w \cot\theta, \tag{2.51}$$

where equation 2.51 is the same term as the first term on the righthand side of equation 2.40, but here the wall normal advection is not zero as it is in the linear solutions. The sign of the anomalous velocities u and w determines the sign of the advection of background buoyancy; sustained motions that are upward will draw heavy fluid from the background up and sustained motions that are downward will draw lighter fluid from the background down. Therefore regions of sustained low momentum homogenize.

Although the planar extent of the computational domain is less than the excursion length of the tide, the domain size (Table 2.1) is justifiably sufficient because the largest eddies in oscillating boundary layers are those associated with the transverse (wall normal) length scale, which is much less than the excursion length. Indeed, at higher Reynolds number (Re = 1790), Gayen and Sarkar (2010a) found the turbulent boundary layer thickness, δ_l, was $\delta_l = 15\delta$ for the unstratified problem and $\delta_l = 17\delta$ for flat plate stratified oscillating boundary layers at the same Reynolds number. The grid resolution parameters for the two Reynolds numbers examined are shown in Table 2.1, where (L_x, L_y, H) are the domain dimensions in (x, y, z), l_{K} and τ_{K} are the Kolmogorov length and time scales, respectively, and wall units (denoted by $^+$) are scaled by the viscous length scale $\delta_v = \nu/U_*$ where U_* is the a priori estimate of the friction velocity, defined

$$U_* = \sqrt{\nu \partial_z \overline{u}}, \tag{2.52}$$

$$\sim \sqrt{\nu \frac{U_\infty}{\delta}}. \tag{2.53}$$

Re	L_x/δ,L_y/δ	H/δ	$\Delta x^+, \Delta y^+$	$\Delta z^+_{\mathrm{wall}}$	$\Delta z_{\mathrm{wall}}/l_{\mathrm{K}}$	$\Delta t_{\mathrm{d}}/\tau_{\mathrm{K}}$	$\Delta t_{\mathrm{d}}/T$
420	59.3	177.8	9.5	0.69	0.40	0.01	$2.2 \cdot 10^{-5}$
840	59.3	177.8	13.5	0.97	0.52	0.02	$2.2 \cdot 10^{-5}$

Table 2.1: Simulation parameters

Solutions to the nonlinear anomaly equations,

$$\partial_x u + \partial_y v + \partial_z w = 0, \tag{2.54}$$

$$\mathrm{d}_t u = \frac{1}{\mathrm{Ro}} v - \partial_x p + \frac{1}{\mathrm{Re}_L}\big(\partial_{xx} + \partial_{yy} + \partial_{zz}\big)u + \mathrm{C}^2 b + \Big(\mathrm{C}^2 + \frac{1}{\mathrm{Ro}^2} - 1\Big)\mathrm{real}[i\mathrm{e}^{it}], \tag{2.55}$$

$$\mathrm{d}_t v = -\frac{1}{\mathrm{Ro}} u - \partial_y p + \frac{1}{\mathrm{Re}_L}\big(\partial_{xx} + \partial_{yy} + \partial_{zz}\big)v, \tag{2.56}$$

$$\mathrm{d}_t w = -\partial_z p + \frac{1}{\mathrm{Re}_L}\big(\partial_{xx} + \partial_{yy} + \partial_{zz}\big)w + \mathrm{C}^2 b \cot\theta, \tag{2.57}$$

$$\mathrm{d}_t b = \frac{1}{\mathrm{PrRe}_L}\big(\partial_{xx} + \partial_{yy} + \partial_{zz}\big)b, \tag{2.58}$$

where the anomalies u, p and b are defined by Equations 2.35-2.37, were computed using the MPI-parallel pseudo-spectral partial differential equation solver *Dedalus* (Burns et al. (2019)) using 128^3 modes. A third-order, four-stage, implicit-explicit Runge-Kutta method derived by Ascher et al. (1997) was used for temporal integration. Chebyshev polynomial bases of the first kind were employed for spatial discretization on a cosine grid in the wall normal direction. Chebyshev polynomials permit the exact enforcement of the adiabatic wall boundary condition (Equation 2.28 minus the background component) on the buoyancy field and no-slip/impermeability wall boundary conditions on the velocities (Equation 3.58 minus the background component). The 3/2 rule dealiasing scheme is used not only for dealiasing the spatial modes online but also for dealiasing post-processed flow statistics.

At the maximum wall normal extent of the domain the boundary conditions at infinity (Equations 2.29 and 2.30) were approximated for the anomalies as free-slip, impermeable conditions

$$\partial_z u = \partial_z v = w = 0, \tag{2.59}$$

and an adiabatic condition on just the anomaly:

$$\partial_z b = 0, \tag{2.60}$$

such that the total flow buoyancy gradient at the $z = H$ is the background buoyancy gradient in that direction.

Although the impermeability condition causes the reflection of internal waves that reach

the upper boundary, the effects are assumed to be negligible because of the negligible amount of energy propagated by such high wavenumber waves in moderate Reynolds number flow. Gayen and Sarkar (2010b) found that for flat-bottomed stratified oscillatory flow at larger Reynolds number flow (Re = 1790), the vertical wave energy flux is less than 1% of the boundary layer dissipation and production rates. Indeed, small but non-zero dissipation rates of turbulent kinetic energy were found near the upper boundary in some of the simulations, presumably from subharmonic parameteric instability or other wave-wave instabilities because of the free-slip reflective upper boundary condition, but 99.9% of the shear production rate and dissipation rate occured within one Ozmidov length of the wall at the lower boundary.

The initial conditions were specified as the sum of the steady component (SBL/RSBL) and the oscillating component (OBL/ROBL at time $t = 0$) of the anomalous linear flow solutions (the sum defined by Equations 2.35-2.36) with uniformly distributed white noise corresponding to buoyancy anomaly perturbations of magnitude 10^{-10} m s^{-2}. All of the simulations that developed turbulence (wall normal integrated production rates of turbulent kinetic energy greater than 10^{-10} m^3 s^{-3}) did so within two oscillations.

ν (m^{2}s^{-1})	ω (rad s^{-1})	f (rad s^{-1})	N (rad s^{-1})
$2.0 \cdot 10^{-6}$	$1.4 \cdot 10^{-4}$	10^{-4}	10^{-3}

Table 2.2: Constant flow characteristics and fluid properties.

The fluid properties and flow characteristics shown in Table 2.2, as well as unity Prandtl number, were held constant for all simulations except $f = 0$ for the stationary reference frame simulations. Much of the abyssal ocean is filled with Antarctic Bottom Water (AABW), characterized by temperatures near 0°C and practical salinities of approximately 35 psu. At $0°C$ and 35 psu, the kinematic viscosity is 1.83×10^{-6} m^2 s^{-1} and the thermal diffusivity is 1.37×10^{-6} m^2 s^{-1} (Chen et al. (1973), Talley (2011)), therefore the kinematic viscosity of AABW is approximately 2×10^{-6} m^2 s^{-1}. Assuming that the buoyancy is only a function of temperature, the buoyancy diffusivity κ might be interpreted as a coefficient of molecular thermal diffusivity, and therefore the molecular Prandtl number for seawater at AABW

temperatures is Pr ≈ 13. A reasonable constant approximation of the background buoyancy frequency at mid latitude abyssal depths is $N = 10^{-3}$ rad s^{-1} (Thurnherr and Speer (2003)). The conventional mid-latitude value of Coriolis parameter is used, $f = 10^{-4}$ rad s^{-1}, therefore the Rossby number (equation 2.15) is near inertial, roughly 1.4. The 12.4 hr period of the M_2 tide is approximated as 44700 s, such that $\omega \approx 1.4 \cdot 10^{-4}$ rad s^{-1}, and therefore $\omega/f \approx 1.4$ and $N^2/\omega^2 \approx 50.6$.

Cases	Re	Ro	C	ϵ	θ (rad)
1,9	840,420	∞	0.25	0.25	$3.53 \cdot 10^{-2}$
2,10	840,420	∞	0.75	0.75	$1.06 \cdot 10^{-1}$
3,11	840,420	∞	1.25	1.25	$1.76 \cdot 10^{-1}$
4,12	840,420	∞	1.75	1.75	$2.47 \cdot 10^{-1}$
5,13	840,420	1.41	0.25	0.35	$3.53 \cdot 10^{-2}$
6,14	840,420	1.41	0.75	1.06	$1.06 \cdot 10^{-1}$
7,15	840,420	1.43	1.25	1.79	$1.76 \cdot 10^{-1}$
8,16	840,420	1.45	1.75	2.53	$2.47 \cdot 10^{-1}$

Table 2.3: Non-dimensional simulation parameters.
The four independent parameters are Re, Ro, C, θ, and Pr = 1. The slope parameter $\epsilon = \tan\theta / \tan\theta_c$ is also used in this study to directly connect results to internal wave parameters. The slope Burger number is $\mathrm{Bu} = \mathrm{Ro}^2\mathrm{C}^2$.

The slope Rossby number (nearly constant with slope, equation 2.15), slope frequency ratio (equation 2.14), Reynolds number (equation 2.12), slope parameter (equation 2.26), and slope angle θ for each of the 16 simulations are shown in table 2.3. The slope frequency ratio C and slope parameter ϵ are redundant for the non-rotating case, but are shown together because C $\neq \epsilon$ for the rotating flow and C appears explicitly in the forcing of the across-isobath (x) momentum equation. Baroclinic tide amplitudes of $U_\infty \approx 1$ cm s^{-1} are routinely observed near abyssal slopes (Simmons et al. (2004), Carter et al. (2008), Goff and Arbic (2010), Turnewitsch et al. (2013)) away from critical slopes, hydraulic spills, and other "hot spots", therefore a characteristic baroclinic tide Stokes layer Reynolds number is Re ≈ 840. 500 m resolution single beam sonar measurements by Becker and Sandwell (2008) indicate that the distribution of global mean (area averaging over $0.1^\circ \times 0.1^\circ$ grid cells) slopes is dominated by the smaller-scale abyssal hill topography and fracture zones. They showed that the mean slopes lie between 0.00 and 0.10 over the vast majority of the seafloor below

2000 m, and that up to 15% of the slopes are super critical with respect to the M_2 tide. Here a range of subcritical and supercritical slopes are investigated to illucidate the Re $\leq$ 840 flow regimes that may occur on low excursion parameter $\mathcal{E} \ll 1$, extra-critical slopes in the abyssal ocean.

2.3.2 Intermittent turbulent bursts

The integrated turbulent kinetic energy (TKE) budget of each simulation was computed in order to distinguish the laminar and turbulent regimes and to determine the mechanisms of turbulence production. The planar mean TKE is defined as

$$K(z,t) \equiv \frac{1}{2}\big(\overline{u'^2} + \overline{v'^2} + \overline{w'^2}\big), \tag{2.61}$$

where the planar mean operator and variable decomposition are defined:

$$\overline{\phi}(z,t) = \frac{1}{L_x L_y}\int_{-L_x/2}^{L_x/2}\int_{-L_y/2}^{L_y/2} \phi(y,z,t)\,\mathrm{dy}\,\mathrm{dx}, \tag{2.62}$$

$$\phi(x,y,z,t) = \overline{\phi}(z,t) + \phi'(x,y,z,t), \tag{2.63}$$

and ϕ is any of the anomalous variables defined by Equations 2.35-2.37. The planar mean TKE evolution equation is

$$\partial_t K + \partial_z \mathcal{T} = \mathcal{P} + \mathcal{B} - \varepsilon \tag{2.64}$$

The TKE transport term $\partial_z \mathcal{T}$ includes all TKE flux divergences (mean, turbulent, pressure, diffusion), which vanish upon wall normal integration of equation 2.64. The rate production of TKE by mean shear is $\mathcal{P}$ (production in the sense that, generally, $\mathcal{P} > 0$), and it is defined as

$$\mathcal{P}(z,t) = -\overline{u'w'}\partial_z\overline{u} - \overline{v'w'}\partial_z\overline{v}, \tag{2.65}$$

$$\mathcal{P}_{13} = -\overline{u'w'}\partial_z\overline{u}, \tag{2.66}$$

$$\mathcal{P}_{23} = -\overline{v'w'}\partial_z\overline{v}. \tag{2.67}$$

The buoyancy flux $\mathcal{B}$ is typically downgradient ($\mathcal{B} < 0$ amidst $\partial_z \bar{b} > 0$ or $\mathcal{B} > 0$ amidst $\partial_z \bar{b} < 0$), in which case it represents the conversion of TKE into potential energy, and it is defined as

$$\mathcal{B}(z,t) = \overline{w'_\eta b'} = \overline{u'b'} \sin\theta + \overline{w'b'} \cos\theta, \tag{2.68}$$

$$\mathcal{B}_1 = \overline{u'b'} \sin\theta, \tag{2.69}$$

$$\mathcal{B}_3 = \overline{w'b'} \cos\theta, \tag{2.70}$$

in the rotated reference frame (where $w_\eta = \mathrm{d}_t \eta$ is the velocity in the vertical, not the wall normal velocity w). Defined in this manner a downgradient buoyancy flux may be reversible, so the term $\mathcal{B}$ includes both the turbulent stirring of and turbulent diffusion of buoyancy. A reversible buoyancy flux may be thought of as a buoyancy flux that converts turbulent kinetic energy into potential energy through stirring alone. Finally, the dissipation rate of turbulent kinetic energy,

$$\varepsilon(z,t) = \nu\big(\overline{(\partial_x u')^2} + \overline{(\partial_x v')^2} + \overline{(\partial_x w')^2} + \overline{(\partial_y u')^2} + \overline{(\partial_y v')^2} + \overline{(\partial_y w')^2} + \overline{(\partial_z u')^2} + \overline{(\partial_z v')^2} + \overline{(\partial_z w')^2}\big) \tag{2.71}$$

is positive definite and therefore the last term of equation 2.64 is always a sink of TKE.

The wave mean, planar mean, wall normal integrated TKE budget statistics for Re = 840 are shown in figure 2-7. The statistics were wave averaged over 5-10 oscillations. All of the integrated TKE budgets at Re = 840, with the exceptions of case 5 and arguably case 7, possess a single burst of turbulence characterized by a rapid increase in the production rate of the TKE from the across-slope shear, $\mathcal{P}_{13}$, the component of shear parallel to the direction of the oscillating body force. The turbulent bursts, which occur shortly after $t/T \approx 0.5$, preferentially select the phase regime during which the velocity is upslope but decelerating and the sign of the oscillating buoyancy changes from positive to negative (phase regime III in Figure 2-5).

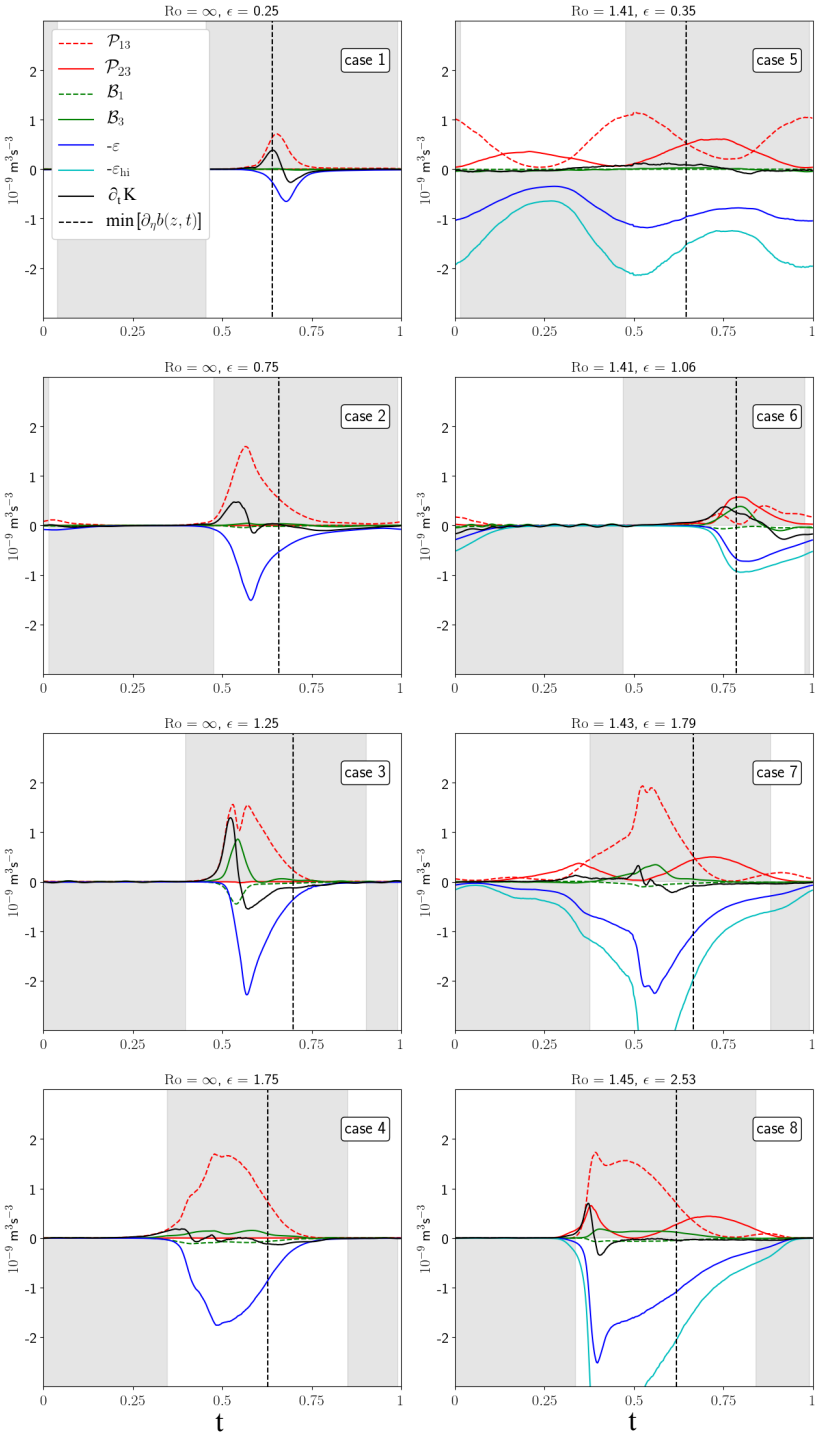

Figure 2-7: Wall-normal integrated, planar mean TKE budgets.
The gray shading corresponds to the sign of the stratification thickness (negative represents enhanced bulk boundary layer stratification, postive represents weakened and/or negative bulk boundary layer stratification. The dashed lines correspond to the time of the minimum total vertical buoyancy gradient in the linear solutions.

Bypass transition induced by gravitational instability

To elucidate the role of the linear buoyancy dynamics in the formation of the turbulent bursts in Figure 2-7, the time of the minimum total vertical buoyancy gradient in the linear solutions, which the reader may recall is negative for all of the considered parameter space as shown in figure 2-6, is plotted as the vertical dashed black line in the integrated TKE budget plots of figure 2-7. The maximum TKE production rate by the mean shear approximately coincides with the time of the minimum total vertical buoyancy gradient for cases 1 and 6, the smallest intensity turbulent bursts shown in Figure 2-7. The timing of the maxima for cases 1 and 6 suggests that the bursts of TKE production rate by the mean shear are modulated by the buoyancy dynamics, despite the fact that the buoyancy fluxes in case 1 appear to be negligible, and the buoyancy fluxes in case 6 become non-zero only *after* the TKE is produced by the mean along-isobath shear represented by the dashed red line.

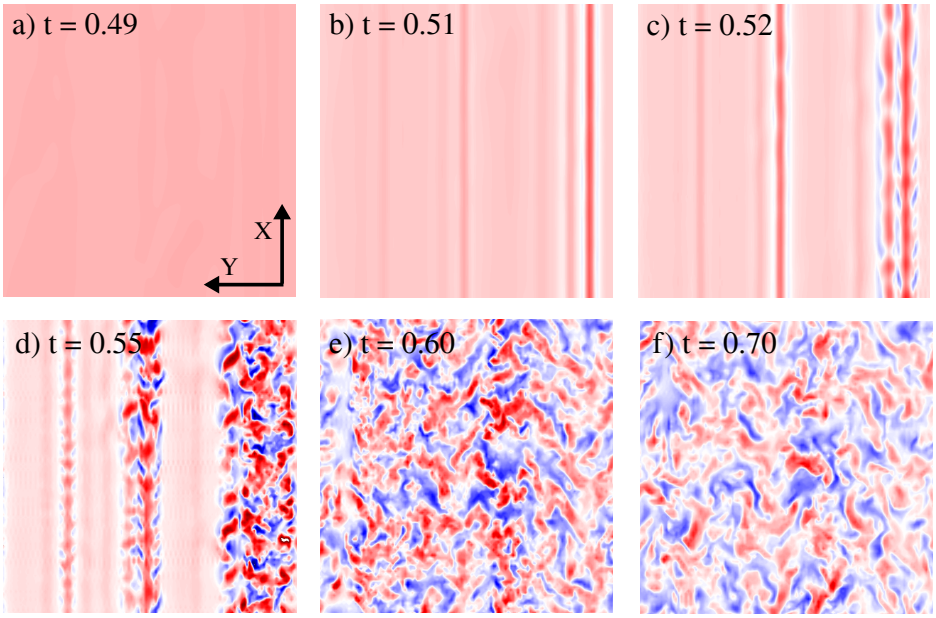

Figure 2-8: Contours of the vertical velocity, w, for case 2.
The contour plots show the vertical velocity at a fixed distance (roughly δ) in the wall normal direction at six consecutive times. $w > 0$ is colored red, while $w < 0$ is colored blue. At $t = 0.5$ the across-isobath velocity is positive but begins to decelerate. Simultaneously, two dimensional rolls form (see plot b)) in the $y-z$ plane, as heavier fluid is advected over lighter fluid trapped near the wall by the friction.

The turbulent bursts in cases 1 and 2 are initiated by gravitational instabilities. The instantaneous vertical velocity of case 2 is plotted in Figure 2-8. In Figure 2-8, red approx-

imately corresponds to upward motions and blue approximately corresponds to downward motions. The generation of two-dimensional convective rolls in the along-isobath / wall-normal (y-z) plane are visible just prior to the begining of a burst. At time $t = 0.51$ the rolls appear and by $t = 0.55$ the rolls have begun to shear apart, erupting into the three-dimensional turbulence at the time of increase in TKE production by mean shear at $t = 0.55$.

The rolls formed by gravitational instabilities in Figure 2-8 are consistent with rolls observed in OBL experiments (Hart (1971)). To verify the hypothesis that gravitational instabilities spawn the rolls, which in turn spawn the turbulent burst, an additional simulation with the same parameters as that of case 2, but with no nonlinear terms in the buoyancy equation, was executed. The simulation of the linearized buoyancy equation version of case 2 had no turbulent bursts after 10 cycles (all other simulations with bursts developed a burst within 2 cycles). The rolls are a bypass transition mechanism, lifting low momentum fluid up and bringing high momentum fluid down into the near wall flow, and so they are effective at destabilizing the shear. The transient gravitationally unstable buoyancy gradients, discussed previously, can trigger OBL turbulent bursts even if the buoyancy fluxes are a negligible source of TKE.

Although the streamwise rolls are initially two dimensional, they inherently produce a three dimensional vorticity field. The inherent three dimensionality of the gravitational instability is evident in the Boussinesq baroclinic production of vorticity term ($\nabla \times \tilde{b}_{\mathrm{d}}$) in the absolute vorticity budget for OBLs and ROBLs,

$$\text{baroclinic production} = \mathrm{C}^2\big(\underbrace{\partial_y \tilde{b} \cot\theta}_{\text{rolls}}\,\mathbf{i} + (\partial_x \tilde{b}\cot\theta - \underbrace{\partial_z \tilde{b}}_{\text{linear flow}})\mathbf{j} - \underbrace{\partial_y \tilde{b}}_{\text{rolls}}\,\mathbf{k}\big). \tag{2.72}$$

The linear OBL vorticity field has only one vorticity component, the spanwise vorticity in the y direction, and the linear ROBL vorticity field is comprised of the spanwise vorticity and the streamwise vorticity in the x direction. In either case, only the $\partial_z \tilde{b}\mathbf{j}$ term in Equation 2.72 is non-zero. However, the rolls produce gradients in the buoyancy field in the y direction. The first and last terms on the righthand side of equation 2.72 indicate that the rolls in the $y - z$ plane will inevitably generate vorticity in the streamwise and wall normal directions, therefore the rolls must induce three-dimensional motion in OBLs or ROBLs. Therefore the

coherent structures shown in figure 2-8, which facilitate the transition to turbulence, must initiate secondary instabilities through three-dimensional baroclinic production of vorticity. Therefore the instabilities are inherently three dimensional, a phenomena that is widely observed in other stratified shear flow instabilities (Peltier and Caulfield (2003)).

The bursts can arise at other times in the oscillation than the time of the maximum negative buoyancy gradient of linear problem, for at least three reasons. First, the re-laminarization phase (the post-burst portions of the phase during which the TKE budgets collapse back to zero) may not relaminarize the flow completely back to the linear solution, depending on the intensity and duration of the turbulent burst. Second, gravitational instabilities must overcome friction to grow (i.e. exceed a critical Rayleigh number); therefore, bursts can occur as soon or as late as friction permits. Hövmuller plots of buoyancy and momentum fluxes of case 1 (Figure 2-9) show the growth of the negative mean buoyancy gradient (the blue region of the plot on the bottom right) propagating out from the wall. The burst, characterized by negative $\overline{u'w'}$ (Figure 2-9, the upper right plot), occurs only after the negative mean buoyancy gradient has reached a certain thickness. Finally, the transient behavior of the mean shear affects its susceptibility to perturbations: shear increasing over time is more stable than steady state shear, which is more stable than decelerating shear (Gad-El-Hak et al. (1984)). In Figure 2-9 in the middle right plot, the mean shear decreases prior to the burst, which is characterized by the patches of non-zero buoyancy flux, negative stress $\overline{u'w'}$, and the erosion of the negative stratification and positive shear.

Boundary layer turbulence is inherently anisotropic and the boundary layers investigated here are no exception. As rolls in case 2 break apart after $t = 0.55$ in Figure 2-8, the Reynolds stresses that are generated are anisotropic; the streamwise-wall normal Reynolds stress $\overline{u'w'}$ is an order of magnitude larger than $\overline{v'w'}$ and $\overline{u'v'}$. The anisotropy of the boundary layer turbulence is also relevant on the smallest turbulent length scales. The majority of abyssal turbulence measurements measure the fluctuations of the vertical shear of the horizontal velocities (Polzin and Montgomery (1996), St.Laurent et al. (2001)). The fluctuations of the vertical shear of the horizontal velocities are used to estimate the dissipation rate of TKE

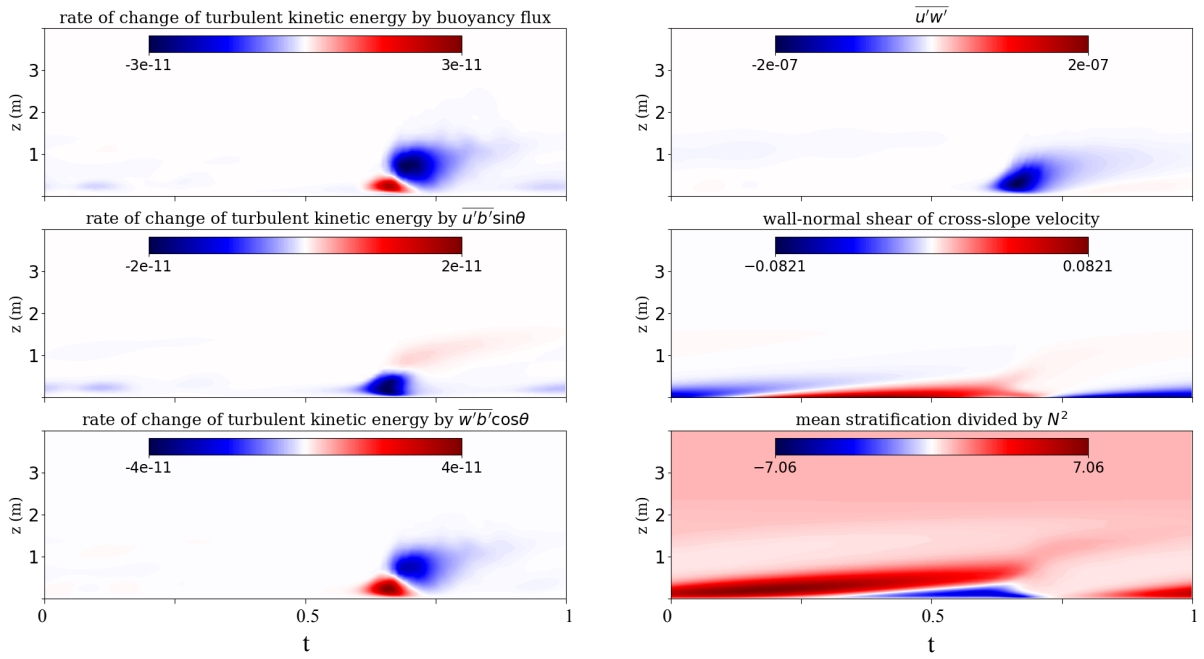

Figure 2-9: Case 1 Hövmuller plots of buoyancy & momentum fluxes.
The fluxes are dimensional (units $\mathrm{m^2 s^{-3}}$) while the wall-normal shear of the across-slope velocity, u, is non-dimensionalized by ω and the stratification by N^2.

for isotropic, homogeneous turbulence (Taylor (1935)), defined as

$$\varepsilon_{\mathrm{hi}} = \frac{15}{4}\nu \cos^2\theta \left(\overline{(\partial_z u')^2} + \overline{(\partial_z v')^2}\right). \tag{2.73}$$

The wall normal integrated form of $\varepsilon_{\mathrm{hi}}$ are plotted for the rotating reference frame cases in Figure 2-7 to illustrate that the assumption of anisotropy for near wall abyssal flows may lead to overpredictions of the dissipation rate of TKE on the order of 100%, regardless of slope angle. The danger of assuming isotropic homogeneous turbulence for analysis of abyssal boundary layers is further compounded if the buoyancy flux model of Osborn (1980),

$$\overline{w'_\eta b'} \approx -0.2\varepsilon_{\mathrm{hi}}, \tag{2.74}$$

is used to estimate the boundary layer buoyancy fluxes. At the wall, the no-slip/impermeable boundary conditions cause the dissipation rate to reach its maximum value and cause the buoyancy flux to vanish, and the error of Equation 2.74 becomes catastrophic.

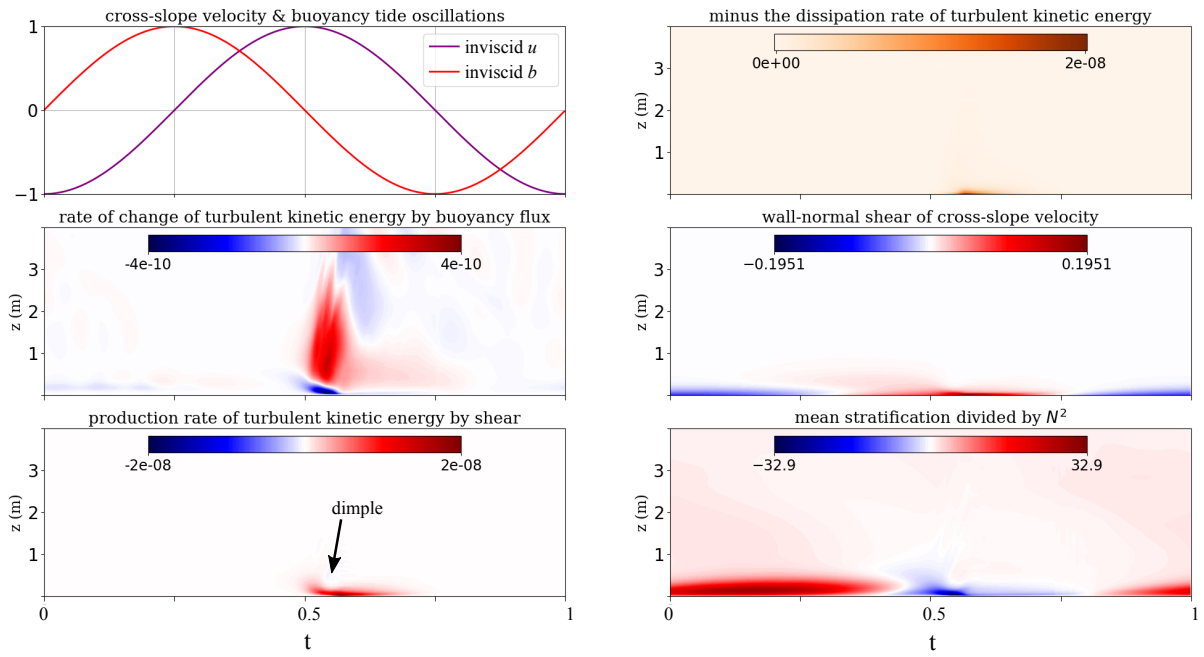

Figure 2-10: Case 3 TKE budget Hövmuller plots.
TKE budget terms are dimensional (units $\mathrm{m^2 s^{-3}}$) and the shear is non-dimensionalized by ω and the stratification is non-dimensionalized by N^2. The inviscid velocity and buoyancy plotted in the top left are the solutions to the inviscid problem (Equations 2.16-2.18) which are the far field boundary condition for the viscous/diffusive problem.

The turbulent bursts in the supercritical OBL cases at $\mathrm{Re} = 840$ (cases 3 and 4) are also triggered by gravitational instabilities (shear production of TKE begins as the buoyancy gradient becomes negative), but the negative buoyancy gradients are persistent enough and strong enough to produce turbulent buoyancy overturns. In case 3, TKE is produced by the mean across-slope shear at $t = 0.5$, followed rapidly by a burst of overturning buoyancy flux in the upper boundary layer as the heavier interior fluid moves over the boundary layer. This is shown in the Hovmöller plots of TKE budget terms for case 3 in Figure 2-10, where the signature of the overturning burst (the positive buoyancy fluxes) can be seen as a dimple in the contours of the mean shear production rate, mean shear, and mean stratification, as well as seen by the large bump in positive $\mathcal{B}_3 = \overline{w'b'}\cos\theta$ in Figure 2-7. The total buoyancy flux for the bump is positive, $\mathcal{B} = \mathcal{B}_1 + \mathcal{B}_3$, which indicates that the mean negative buoyancy gradient near the wall in the stratification Hovmöller plot in Figure 2-10 is strong enough to *produce* TKE in the region above it, behavior akin to a heat source. Comparison of case 3 in

Figure 2-7 and Figure 2-10 shows that the positive buoyancy flux then erodes the negative buoyancy gradient, followed by a period of TKE production by mean shear - dissipation balance. The destruction of negative mean buoyancy gradients by positive buoyancy fluxes during phase III also occured in large eddy simulations by Slinn and Levine (1997).

The linear solutions not only indicate that the magnitude of the minimum negative buoyancy gradient increases with slope parameter (as shown in Figure 2-6), but also that the gradient is confined to a narrower and narrower region adjacent to the wall (as shown by the real components of the linear solution e-folding scales shown in Figure 2-4). The shear in the linear solutions also increases with slope parameter, but to a lesser extent than the buoyancy gradients. Holding all other parameters constant, an optimal slope parameter exists at which the negative buoyancy gradient and its thickness yield the largest possible Rayleigh number for the flow. Indeed, the integrated buoyancy fluxes in case 4 are smaller than those for case 3 in Figure 2-7, despite the fact that the mean negative stratification near the wall is stronger for case 4 than for case 3 (see Hovmöller plots of mean stratification shown in Figure 2-11), because the transverse lengthscale of the linear solution for the stratification decreases with slope parameter. Note that the phase shift in the linear solutions for the boundary layers that occurs between subcritical and supercritical slopes means that the upper boundary layer buoyancy gradient leads the lower boundary layer buoyancy gradient as can be seen in the buoyancy gradient Hovmöller plots of Figure 2-11. The phase shift in the linear solution that occurs between subcritical in supercritical slopes is correlated with the increase in buoyancy fluxes (approximately zero in the subcritical cases in Figure 2-7) to appreciable values (the green lines in Figure 2-7 for cases with $\epsilon > 1$). The non-zero buoyancy fluxes for cases with $\epsilon > 1$ occur because the boundary layer stratification increases with increasing slope, as predicted in the linear solutions (Appendix A) and shown by the color bar axes in Figure 2-11, which increase with θ.

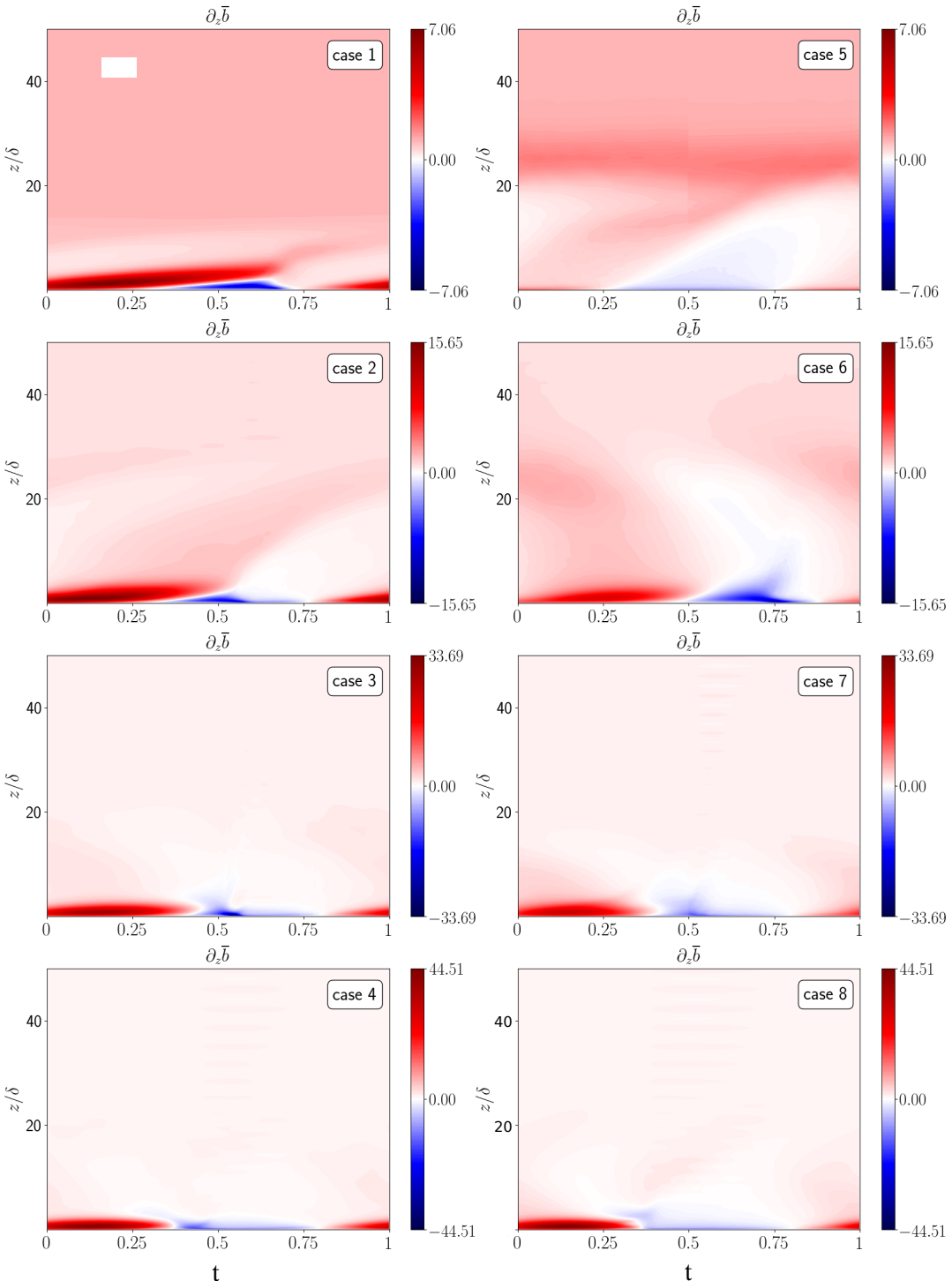

Figure 2-11: Re = 840 Hövmuller plots of mean stratification.
The total wall normal buoyancy gradients are non-dimensionalized by N^2. The color bar axes show that the boundary layer stratification maxima/minima increase/decrease with increasing slope.

Modulation of turbulence by stratification

While the OBL turbulent bursts are produced by the breakdown of the mean shear initiated by gravitational instabilities, gravitational instabilities are not the only way in which the buoyancy field alters the production of turbulence. The temporal asymmetry of the bursting is remarkably coherent: for all of simulations, if bursts occured, they occured during the same phase for every simulated cycle (predominately phase III, with some in late phase II and one in phase IV). The consistency contrasts the intermittent turbulence regime of Stokes' second problem, in which a single burst occurs per oscillation, corresponding to the random selection of one of two shear maxima that occur within one period (Spalart and Baldwin (1987)). Additional DNS computed for this study, of Stokes second problem, verified the results of Spalart and Baldwin (1987), which also showed a random selection of one of the two shear maxima for a larger burst at Re = 840.

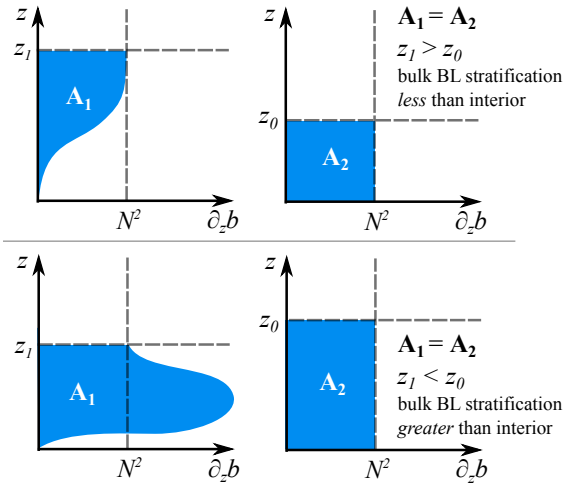

Figure 2-12: Stratification thickness concept.

To obtain an integral quantity for estimating the stabilizing/destabilizing effects of the boundary layer buoyancy gradient, the logic behind the concept of boundary layer displacement thickness is borrowed from boundary layer theory (Monin and Yaglom (1971)) and applied to sloping diffusive boundary layers of stratified flows. The quantity measures the boundary layer stratification and shall be referred to as the stratification thickness, δ_s. The basic concept: if the total buoyancy field is not constant over small distance in the wall normal direction z_1, then it can be approximated as constant over some distance z_0 from the

wall, such that

$$N^2 z_0 = \int_0^{z_1} \partial_z \tilde{b} \, \mathrm{dz}, \tag{2.75}$$

therefore

$$\delta_s = z_1 - z_0 = \int_0^{z_1} \left(1 - \frac{\partial_z \tilde{b}}{N^2}\right) \mathrm{dz}. \tag{2.76}$$

Equation 2.75 is the calculation of the areas $\mathbf{A}_1$ in Figure 2-12. $\delta_s > 0$ indicates that the bulk boundary layer stratification is less than the background stratification, N^2, and $\delta_s < 0$ indicates that the bulk boundary layer stratification is greater than the background stratification (see figure 2-12). The stratification thickness concept implicitly relies on the fact that the diffusive flows of interest have a constant farfield stratification solution; therefore stratification thickness concept cannot be applied to the flat bottom ($\theta = 0$) case. $\delta_s < 0$ for both the SBL and RSBL flows, consistent with the fact that the steady laminar flows increase the positive stratification near the boundary. The inviscid regime with heaving isopycnals and no boundary layer described in inviscid forcing equations, Equations 2.16-2.18, has exactly zero stratification thickness for all time because the isopycnals do not bend to meet the wall.

The sign of the stratification thicknesses for Re = 840 cases (cases 1-8) is illustrated in the integrated TKE budget plots of Figure 2-7 as the gray shaded areas and plotted in the left column of Figure 2-13. The maximum rate of production of TKE by the mean shear occurs during the phase of $\delta_s > 0$ for all simulations (even for case 5, which will be discussed in detail later), corresponding to boundary layer stratification that is less than the far field stratification for all cases. The stratification thickness in Figures 2-7 and 2-13 also indicates a phase shift in the boundary layer stratification with increasing slope parameter that is consistent with the linear solution modes shown in Figure 2-4. During the phase of strong boundary layer stratification, $\delta_s < 0$ (approximately phases I and II), the boundary shear instabilities must overcome not only the stabilizing effect of increased stratification but also the stabilizing presence of the wall that is present regardless of phase. Linear stability analysis by Schlichting (1935) yielded a critical gradient Richardson number of 1/24 for a stratified Blasius boundary layer, notably lower than the Miles-Howard theorem threshold for inviscid stratified shear. In the context of the OBL/ROBL, Schlichting (1935) analysis

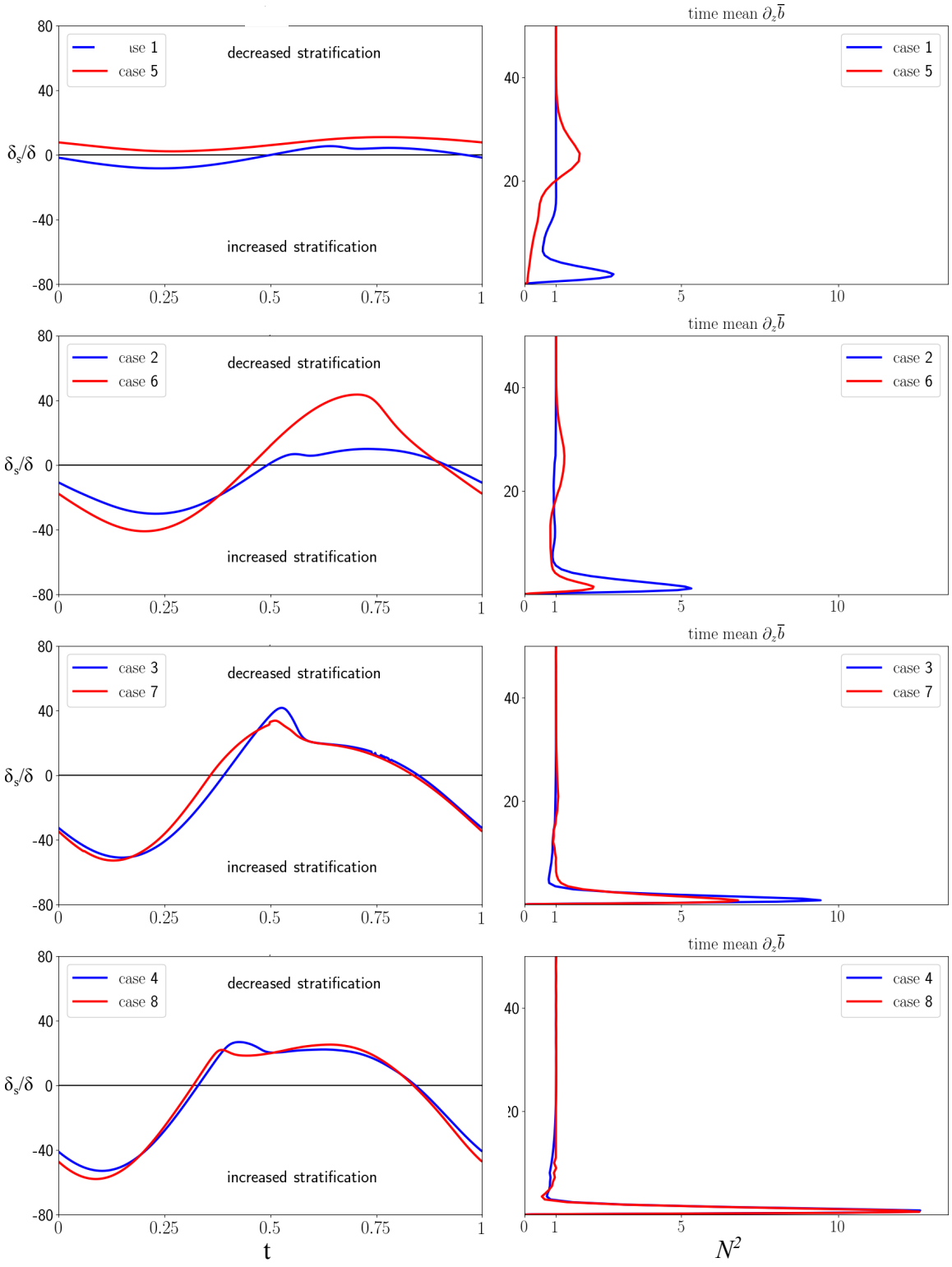

Figure 2-13: Re = 840 stratification thickness and time mean stratification.

indicates that the flow is more significantly stable with respect to shear perturbations during $\delta_s < 0$. However, if the flow is turbulent during the phase of $\delta_s < 0$, the simulations of Umlauf and Burchard (2011) suggest mixing is much more efficient, presumably because the turbulence intensity required to overcome the strengthened boundary layer stratification must be considerable. Therefore the sign of the stratification thickness can be interpreted as whether or not the stratification will have a destabilizing effect on the boundary layer or a stabilizing effect that correlates with more efficient mixing if the mean shear is producing turbulent kinetic energy.

At least three mechanisms aid in the decay of and relaminarization of the turbulent bursts. First, the turbulent burst diffuses the mean shear and thus its primary energy source. Second, the tidal acceleration opposes the mean shear during $t = [1/2 - 1]$ (phases III and IV), and so the decay and reversal of the shear amplitude means that less mean flow kinetic energy is available. Third, once the flow reverses the outer boundary layer becomes increasingly stratified, as mentioned previously, when $\delta_s < 0$. Therefore, for a burst to persist across the entire phase it must have a constant source of mean shear of large enough magnitude to sustain production of TKE throughout flow reversals and increased stratification.

Slope Burger number

The ROBL cases 6,7, and 8 exhibit similar turbulent bursts as cases 1 through 4, while case 5 features shear production rate - dissipation rate balance throughout the period. To discern why cases 6,7, and 8 feature turbulent bursts whereas case 5 features a fully turbulent (fully turbulent is defined here as turbulent throughout the period) the Burger number is a useful metric. All of the boundary layers examined in this study are modulated on superinertial time scales ($\omega > f$), therefore Ekman shut down / buoyancy arrest is not relevant because the boundary layers oscillate too fast for Ekman transport to be significant. The slope Burger number is defined as

$$\mathrm{Bu} = \mathrm{Ro}^2\mathrm{C}^2, \tag{2.77}$$

$$= \frac{N^2 \tan^2\theta}{f^2}. \tag{2.78}$$

The Burger number is the ratio of inertial period to the time scale associated with the buoyancy force. The slope Burger number (Equation 2.78) accounts for the effect of the slope on the boundary layer by indicating that at large slope angles the buoyant restoring force will dominate the Coriolis force, because the component of the Coriolis force projected onto the wall normal direction decreases with increasing slope. In the non-rotating reference frame the slope Burger number is infinite because there is no Coriolis force present.

Case	Bu
5,13	0.124
6,14	1.127
7,15	3.173
8,16	6.347

Table 2.4: Simulation slope Burger numbers.

Table 2.4 shows the Burger number for the ROBL flows, cases 5-8 and 13-16. The lowest slope Burger number cases, 5 and 13, are influenced the most by rotation. In all of the rotating flows, the mean shear can produce turbulence throughout the period because the velocity field oscillates in a Stokes-Ekman layer manner. However, at larger slope angles the slope Rossby number and slope Burger numbers, which indicates that the dynamics will be controlled primarily by the balance between the relative vorticity (i.e. the tidal forcing) and the buoyant restoring force. Case 5 will be discussed in the next section, *Stratified Stokes-Ekman layers on slopes*. In cases 6 and 14, the slope angle θ is the same as that for case 2, but the inviscid flow is near critical $\epsilon \approx 1$ and therefore the linear inviscid flow solutions for the far field begin to break down as $A \to 0$ and the forcing no longer adequately describes the baroclinic tide. Therefore the applicability of cases 6 and 14 is limited.

The integrated TKE budgets shown in Figure 2-7 indicates that the large slope Burger number cases do indeed behave more like the non-rotating problem, at least at the Reynolds numbers investigated in this study. Cases 7 and 8 are both supercritical and have Bu > 1. Their dynamics resemble the OBL solutions in cases 3 and 4, with bursts of turbulence that occur during the phase of weak boundary layer stratification ($\delta_s > 0$) and relaminarization processes during the phase of strong boundary layer stratification ($\delta_s < 0$). The

ROBL turbulent bursts resemble the OBL bursts more closely with increasing supercriticality. However, in case 7, the oscillations of the tidal ellipse are apparent in the along-slope shear production $\mathcal{P}_{23}$ but not in the across-slope shear production $\mathcal{P}_{13}$, which suggests that highly supercritical flows characterized by Bu > 1, $\epsilon > 1$ feature TKE production by the rotating mean shear in the along-slope direction and TKE production that is controlled by the boundary layer stratification in the across-slope direction. Increasing Bu and ϵ further, as in case 8, appears to increase the control of TKE production by the BL stratification, but during the phase of weak boundary layer stratification ($\delta_s > 0$), the along-slope shear production $\mathcal{P}_{23}$ appears to be unaffected (note the nearly identical shape and size of the bump in $\mathcal{P}_{23}$ between cases 7 and 8). The wave-mean stratification of case 8 also closely resembles that of case 4 (see Figure 2-11). To summarize: the low slope Burger number boundary layers can more readily sustain turbulence throughout the tide period and the *turbulence* of the Bu > 1 boundary layers is primarily controlled by the stratification, similar to what was observed in the non-rotating boundary layer dynamics.

Critical Rayleigh number

Since the turbulent bursts of the OBL and small time scale ratio ROBL flows appear to be triggered by gravitational instabilities, lower Reynolds number simulations at Re=420 (cases 9-16) were computed to estimate a critical Rayleigh number for the approximately linear flow. All of the simulations at Re=420 remained laminar except for cases 9,15, and 16, which feature small bursts of TKE production, shown in Figure 2-14.

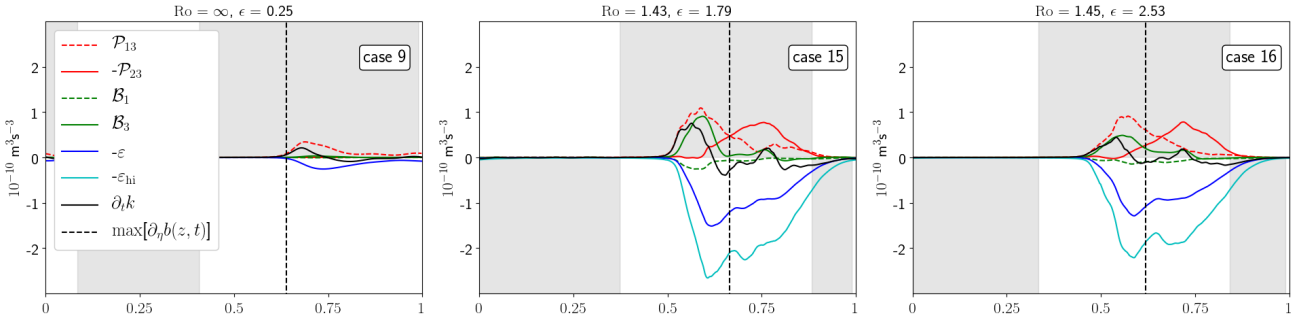

Figure 2-14: Re = 420 integrated TKE budgets.

Case 9 (Re = 420, $\epsilon = 1/4$, Ro $= \infty$) indicates an upper bound for the critical Rayleigh

number of Ra ≈ 500 based on the definition of the Rayleigh number above (Equation 2.48) and the minimum total buoyancy gradient contours of Figure 2-6. Curiously, the larger slope parameter, Re = 420, OBL cases (cases 10,11, and 12) remained laminar, which is counter to the hypothesis that the flow is primarily gravitationally unstable, because the minimum total buoyancy gradient contours in the linear solutions, shown in Figure 2-6, predict larger gravitational instabilities with increasing slope parameter for both OBLs and ROBLs. Streamwise vorticity disturbances are known to grow at low Reynolds number in gravitationally unstable Couette flow, and it is possible that a velocity inflection-point instability may be work in case 9. However, the rotating cases at Re = 420, cases 15 and 16, are consistent with the gravitational instability hypothesis.

2.3.3 Stratified Stokes-Ekman layers on slopes

The tidal ellipse

The integrated TKE budget of case 5 shown in Figure 2-7 is characteristic of a Stokes-Ekman boundary layer. For constant density, Stokes-Ekman boundary layers are fully turbulent for Re > 800 (Salon and Armenio (2011)). The velocity oscillates at the tide frequency in the plane of the slope, resulting in the tidal elipse shown in the hodograph in Figure 2-15. The TKE budget is dominated by two mean shear production rate components $\mathcal{P}_{13}$ and $\mathcal{P}_{23}$, which oscillate with the tide and are suppressed during the phase of strong stratification ($\delta_s < 0$) visible in Figures 2-7 and 2-11.

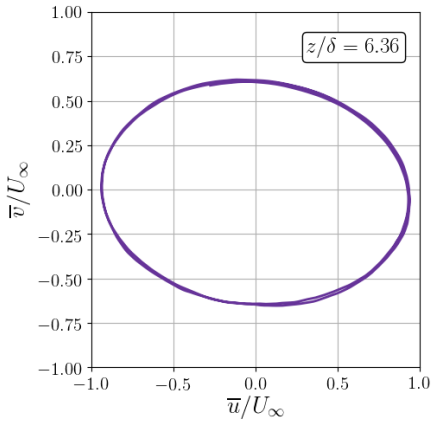

Figure 2-15: Hodograph of the case 5 mean velocity at $z/\delta = 6.4$.

The law of the wall

Figure 2-16 shows that the velocity profiles in the stratified Stokes-Ekman layer at Re = 840 do not adhere to the law of the wall throughout the majority of the phase of the oscillation, though a viscous sublayer occurs universally. The profiles of $u^+(z^+)$, as defined by

$$u^+ = \frac{\sqrt{\overline{u}^2 + \overline{v}^2}}{u_*}, \qquad z^+ = \frac{z u_*}{\nu}, \tag{2.79}$$

where the friction velocity is defined

$$u_* = \sqrt{\nu \sqrt{(\partial_z \overline{u})^2_{z=0} + (\partial_z \overline{v})^2_{z=0})}}, \tag{2.80}$$

are steeper (more laminar-like) than the log-law, shown with the dashed black line beginning at the top of the buffer region at $z^+ = 10$ in Figure 2-16, for the majority of the period. Simulations of stratified Stokes layers at Re = 1790 by Gayen and Sarkar (2010a) indicate that the velocity profile exceeds the law of the wall if the flow is stratified, and that the range of phases where the logarithmic law is valid decreases with increasing stratification. Since stratified Stokes-Ekman layers on flat plates may be Reynolds number critical at a higher Reynolds number than the unstratified case, the steeper slopes of u^+ than the law of the wall shown in Figure 2-16 may be due to the fact that the Reynolds number (Re = 840) barely exceeds the known critical Reynolds number for the homogeneous density flat plate Stokes-Ekman layers. This suggests that the lack of fit to the wall of the law shown in Figure 2-16 occurs because the flow is transitional and the dissipative and large eddy scales are not separated enough to permit a significant inertial subrange.

A notable exception occurs at $t = 3/4$ in Figure 2-17, where a log layer forms approximately between $30 < z^+ < 400$ with a *intercepta* of ≈ 4 (lower than the conventional value of ≈ 5 for smooth surfaces). $t = 3/4$ is the point in the phase at which the far field velocity shifts from upslope flow to downslope flow (the transition from phase regime III to phase regime IV in Figure 2-5) and the TKE production rate is dominated by the shear production in the along slope direction (see Figure 2-7). Taken together with the fact that the boundary layer stratification was weak during this portion of the phase ($\delta_s > 0$), it is clear that the flow

reversal amidst weakened stratification increased the production of TKE by mean shear. In the opposite case ($t = 1/4$) no log layer appeared, presumably because the turbulence during the reversal from downslope flow to upslope flow was suppressed by the increased boundary layer stratification ($\delta_s < 0$).

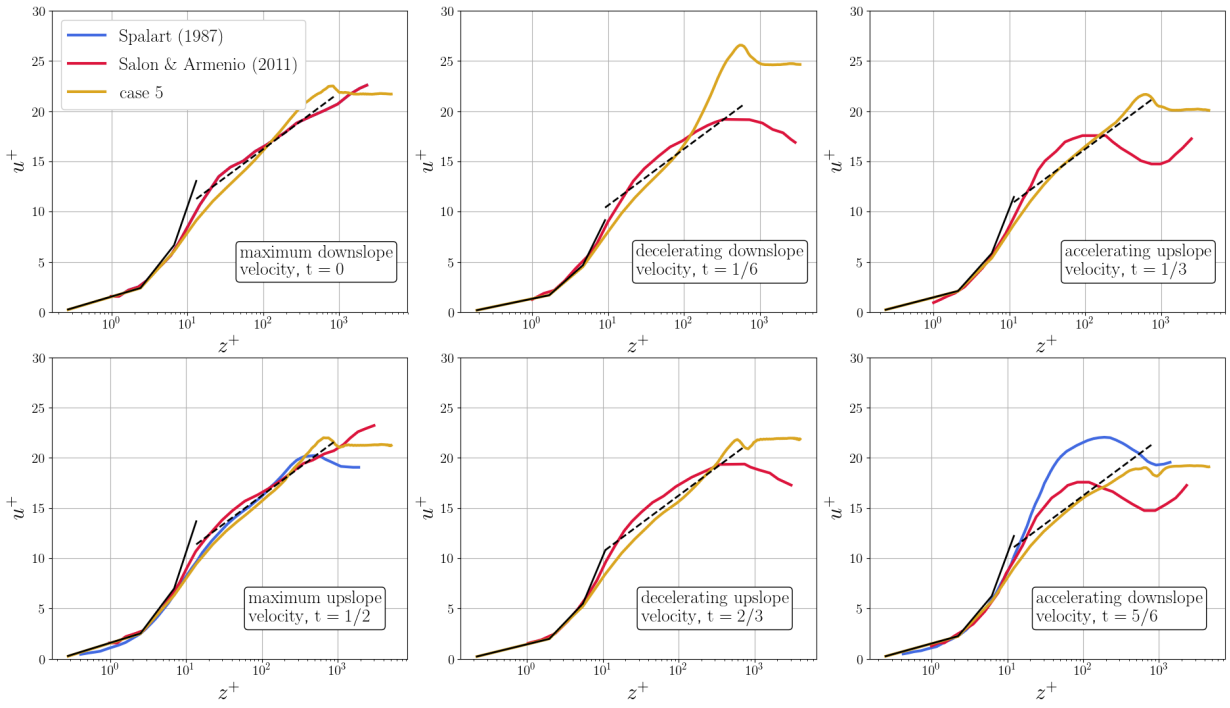

Figure 2-16: The law of the wall in a turbulent, stratified, Stokes-Ekman layer on a slope. DNS velocity profiles of Stokes' second problem by Spalart and Baldwin (1987) and Salon and Armenio (2011) are shown for comparison. The dashed black line is the law of the wall and the solid line is the viscous sublayer.

Curiously, the u^+ profiles in Figure 2-16 are more symmetric between accelerating and decelerating phases than the cases of Stokes' second problem (Re = 1000, Spalart and Baldwin (1987)), stratified Stokes second problem ($0 \leq \mathrm{C}^2/\sin^2\theta \leq 2500, \mathrm{Re} = 1790$ Gayen and Sarkar (2010a)), or even the Stokes-Ekman layer (Re = 1790, Salon and Armenio (2011)). This suggests that the energy supplied by the mean shear is more consistent in the stratified Stokes-Ekman layer than in stratified Stokes' layers or Stokes-Ekman layers.

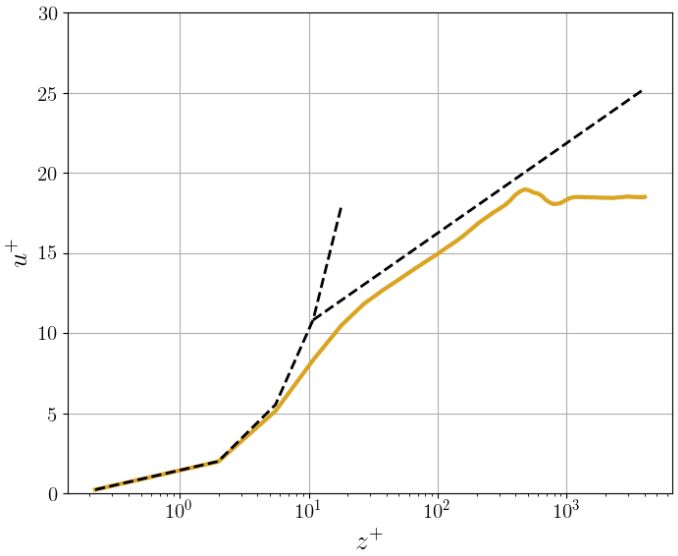

Figure 2-17: The law of the wall for case 5 at $t = 0.75$.

Turbulent equilibrium

The sustained turbulence did not resonate with the baroclinic oscillation. Since turbulence generates advective motions and waves at a spectrum of frequencies, it is conceivable that the fully turbulence regime might excite frequencies lower than the tide. Decomposing C and Ro and rearranging the non-dimensional amplitude (Equation 2.20) yields the expression

$$\omega^2(1 + A) = N^2 \sin^2\theta + f^2 \cos^2\theta, \tag{2.81}$$

where criticality slope is defined by $A = 0$, such that

$$\omega^2 = N^2 \sin^2\theta + f^2 \cos^2\theta, \tag{2.82}$$

where A is non-dimensional. However, that definition of criticality pertains to the criticality of the tidal forcing at frequency ω. However, if turbulent motions occur within the boundary layer that sustain motions at frequencies of ω', the motions at the frequency ω' can be resonant even when the tidal forcing is not (i.e. $|A| > 0$). Resonant turbulent motions are therefore described by

$$\omega'^2 = N^2 \sin^2\theta + f^2 \cos^2\theta. \tag{2.83}$$

Dividing Equation 2.83 by the tidal forcing frequency yields an expression for the resonance condition of turbulent fluctuations as a function of the non-dimensional ratios

$$\frac{\omega'^2}{\omega^2} = \left(\frac{1}{\mathrm{Ro}^2} + \mathrm{C}^2\right). \tag{2.84}$$

For case 5 this suggests that turbulent motions that are roughly 3/4 the tide frequency ($\omega' \approx 0.76\omega$, so the resonant period is $\approx 1.3T$.) could excite resonance with the tide. No discernable sub-tidal resonant behavior occured in the Stokes-Ekman layer Figure 2-18, the temporal evolution of the integrated TKE budget of case 5, because 1) the turbulence production time scale $k/\varepsilon \ll \omega^{-1}$ and 2) the modulation of the peaks in Figure 2-18 is clearly traceable to the oscillating stratification, as mentioned above.

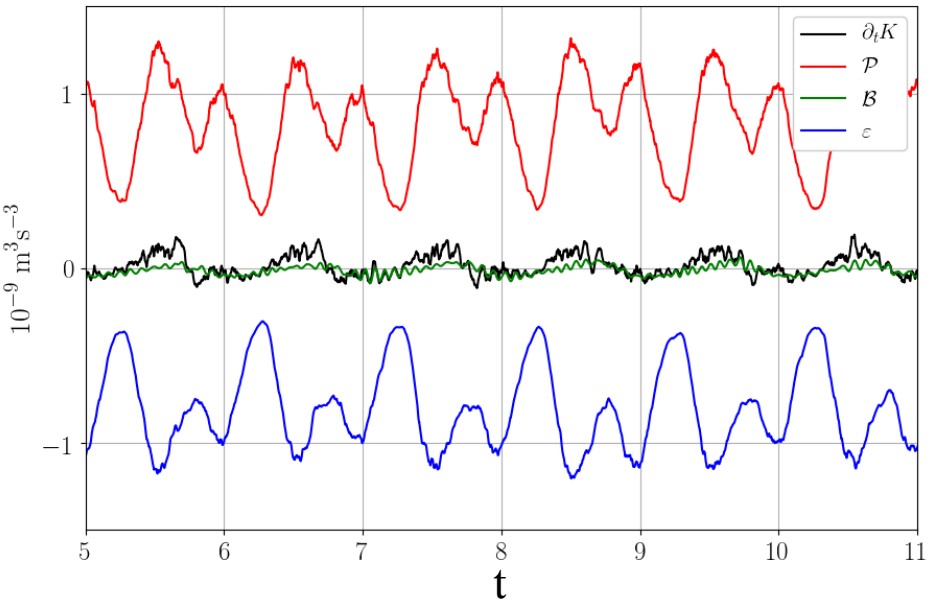

Figure 2-18: The evolution of the wall normal integrated TKE budget for case 5.

2.3.4 Irreversible mixing efficiency

The irreversible mixing efficiency (Peltier and Caulfield (2003)) is a measure of the amount of irreversible loss of kinetic energy to potential energy done by turbulence relative to the amount of irreversible loss of kinetic energy to dissipation. Since the turbulence in case 5 is fully developed (in the sense that it occurs throughout the phase), the irreversible mixing

efficiency was estimated by assuming that the irreversible change in the vertically integrated potential energy is approximately equivalent to the wall normal integrated difference in potential energy between the time mean of the turbulent flow and the laminar (RSBL) flow. The wave period is the appropriate time scale for and the rate of potential energy change because, if the potential energy change occured over a longer time scale, the flow would necessarily restratify due to the advection of the background buoyancy gradient. Under the above assumptions, the rate of potential energy change is defined as

$$\Delta P = -\frac{1}{T}(\bar{b}_d(\eta) - b_{d,\mathrm{S}}(\eta))\eta, \tag{2.85}$$

where $\bar{b}_d$ is the time mean dimensional buoyancy anomaly and $\bar{b}_{d,\mathrm{S}}$ is the steady, linear component of the anomaly (see Equation 2.36) and the irreversible mixing efficiency for case 5 is

$$\frac{\int \Delta P \, d\eta}{\int \Delta P \, d\eta + \int \varepsilon \, d\eta} = 0.14. \tag{2.86}$$

The mixing efficiency estimate in Equation 2.86 may seem small given the small magnitude of the wall-normal integrated total buoyancy fluxes relative to the dissipation rate of Figures 2-7 and 2-18, but the buoyancy fluxes change sign with height, so the vertical integration of the buoyancy fluxes can obscure the details of mixing.

2.3.5 Diapycnal transport

To quantify the rate of water mass transformation, the Eulerian diapycnal velocity $\overline{\mathbf{u}}_\mathrm{e}$ (Marshall et al. (1999), Ferrari et al. (2016)) was calculated. It is defined as the steady state velocity component normal to the time mean isopycnal contours:

$$\overline{\mathbf{u}}_\mathrm{e} = (\overline{\mathbf{u}} \cdot \mathbf{n}_b)\mathbf{n}_b - \overline{\mathbf{u}}_b = \frac{\overline{\nabla \cdot \mathbf{F}_b}}{|\nabla \bar{b}|}\mathbf{n}_b - \frac{1}{|\nabla \bar{b}|}\partial_t \bar{b}\mathbf{n}_b, \tag{2.87}$$

where $\mathbf{n}_b$ is the unit vector normal to the surface of constant buoyancy. Assuming the isopycnals are in steady state (time mean denoted by overbar), the last term on the RHS (the movement of isopycnal surfaces) is zero ($\partial_t \bar{b} = 0$ by definition of the steady state). The unit vector normal to surfaces of constant buoyancy (antiparallel to the unit vector normal

to isopycnals) is defined by

$$\mathbf{n}_b = \frac{\nabla \bar{b}}{|\nabla \bar{b}|}, \tag{2.88}$$

such that positive $\mathbf{n}_b$ points in the direction of increasing buoyancy / decreasing density. Therefore the projection of Eulerian time-mean velocity vector onto the diapycnal coordinate is

$$\overline{\mathbf{u}}_\mathrm{e} = \frac{\nabla \cdot \mathbf{F}_b}{|\nabla b|}\mathbf{n}_b = U_\mathrm{e}\mathbf{n}_b \tag{2.89}$$

Therefore if $U_\mathrm{e} > 0$, the diapycnal velocity represents the buoyancy flux convergence (the density within the control volume is decreased) and $U_\mathrm{e} < 0$ represents buoyancy flux divergence (the density within the control volume is increased).

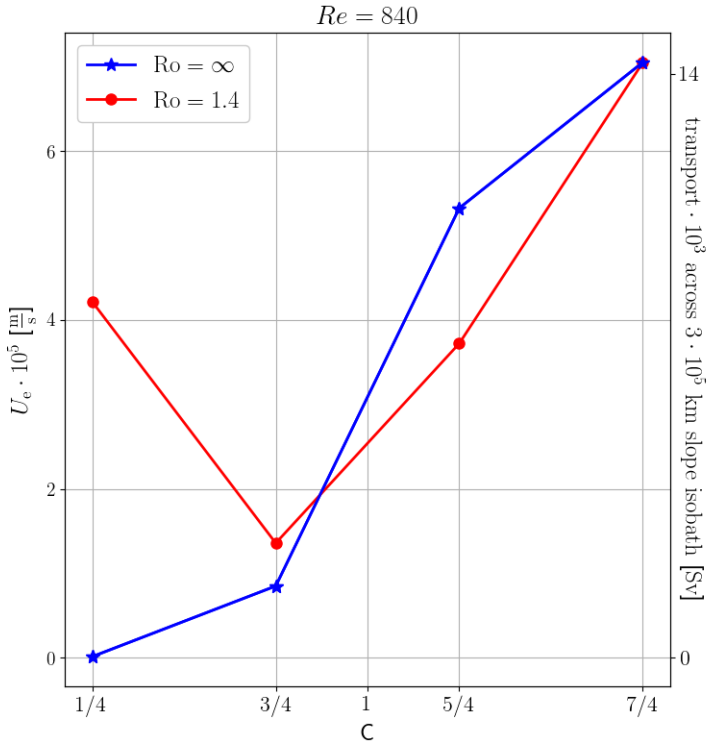

Figure 2-19: Diapycnal transport for Re = 840.

As expected, the diapycnal transport is upward, corresponding to a decrease in local potential energy, and it is of small magnitude. Assuming the flows simulated here are valid over 300,000 km abyssal slopes in the along slope direction, globally, figure 2-19 shows that the boundary layers would produce only $\sim$ 0.014 Sv of abyssal water mass transformation

compared to ~ 0.002 Sv of abyssal water mass transformation by the laminar flow alone and compared to the approximately 20 Sv of abyssal water mass transformation required to conserve mass in the abyssal ocean.

2.3.6 The dissipation rate of TKE

Frictional dissipation of the tide is often estimated from the relation $c_D|U|U^3$, where c_D is the dimensionless drag coefficient and U is an estimate of the bulk velocity (Jayne and St. Laurent (2001), St.Laurent and Garrett (2002)). For flat plate boundary layers, the transitional flow regime is characterized by drag coefficients in the range $0.001 \leq c_D \leq 0.005$, for $1 < \mathrm{Re} < 10^3$ or equivalently $1 < \mathrm{Re}_L < 10^6$ (Hoerner (1965)). The drag coefficients for the boundary layers in this study were calculated using the equation

$$c_D = U_\infty^{-3} \int_0^H \overline{\varepsilon}\, \mathrm{dz}, \tag{2.90}$$

where $\overline{\varepsilon}$ is the time mean dissipation rate of TKE with dimensions $\mathrm{m^2 s^{-3}}$.

The drag coefficients are shown in Table 2.5. The drag coefficient values shown in Table 2.5 mostly fall within the expected range for flat plate boundary layers, with the exception of the steepest slope case at Re = 840, case 8. The drag coefficients are small at Re = 420 for all but the steepest slope angles in the rotating reference frame (cases 15 and 16). Here ~ 0 indicates that the drag coefficient was zero to machine precision (purely laminar flow). The drag coefficients increase with slope at constant Reynolds number, and they effectively vanish somewhere in the range $420 < \mathrm{Re} < 840$ on lower slopes were the flow is in the laminar or disturbed laminar regime.

Despite the fact that the turbulence is intermittent in all of the cases except for case 5, the time mean dissipation rates exceed that of the oceanic background level of TKE dissipation, $\varepsilon_0 \approx 10^{-10}$ $\mathrm{m^2 s^{-3}}$ (St.Laurent et al. (2001), Mashayek et al. (2017)). The profile maxima of the time mean dissipation rate of TKE and the time mean rate of TKE production by mean shear, shown in Figure 2-20, are $\varepsilon = \mathcal{O}(10^{-9})$ $\mathrm{m^2 s^{-3}}$ for Re = 840 and $\varepsilon = \mathcal{O}(10^{-10})$ $\mathrm{m^2 s^{-3}}$ for Re = 420. The increase in dissipation rate with $\mathrm{C} = N \sin\theta/\omega$ is due to the fact that as the slope increases, the turbulence production rate is primarily supplied with energy

Case	Re	c_D
1,9	840,420	$1.8 \cdot 10^{-4}$, $8.8 \cdot 10^{-5}$
2,10	840,420	$9.7 \cdot 10^{-4}$, ~ 0
3,11	840,420	$1.6 \cdot 10^{-3}$, ~ 0
4,12	840,420	$3.5 \cdot 10^{-3}$, ~ 0
5,13	840,420	$4.7 \cdot 10^{-3}$, ~ 0
6,14	840,420	$5.1 \cdot 10^{-4}$, $1.6 \cdot 10^{-8}$
7,15	840,420	$5.0 \cdot 10^{-3}$, $1.5 \cdot 10^{-3}$
8,16	840,420	$5.4 \cdot 10^{-3}$, $1.4 \cdot 10^{-3}$

Table 2.5: Drag coefficients estimated from simulation time mean dissipation rates.

from the mean shear at low slope angles and is supplied with energy from the mean shear and buoyancy fluxes at larger slope angle. As mentioned above, the weak turbulence for the C = 3/4 Ro $\approx$ 1.4 case arises from the fact that it is critical and the linear forcing decays in the asymptote of criticality.

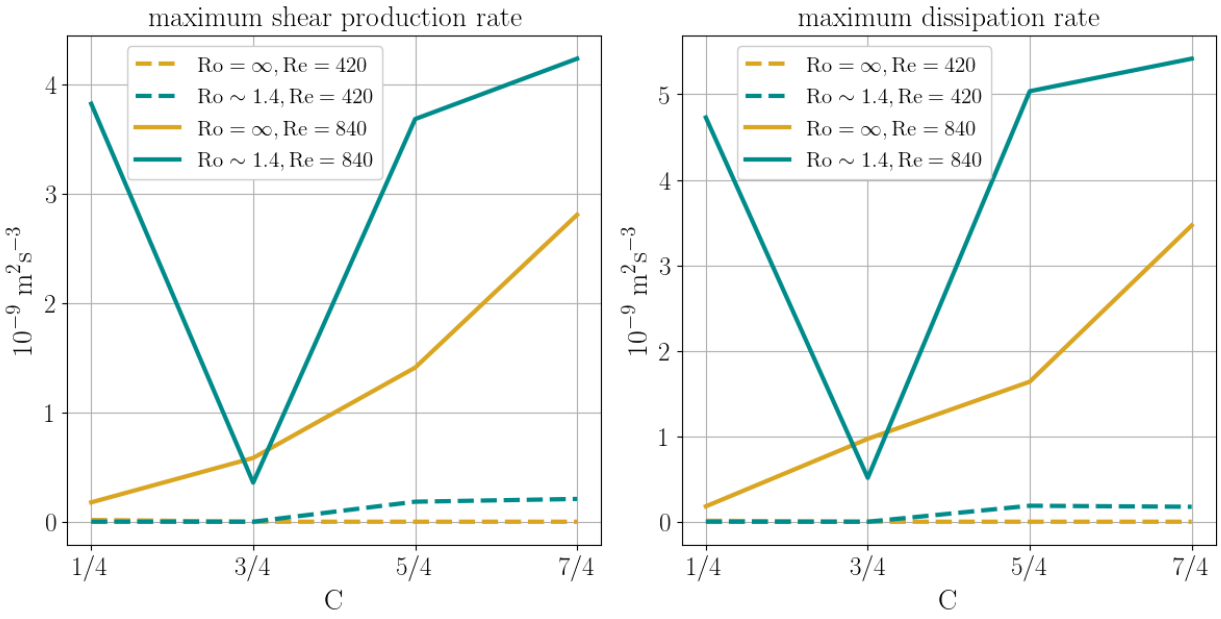

Figure 2-20: Time mean shear production & dissipation rate maxima.

2.4 Discussion

2.4.1 High Reynolds numbers

The simulations at Re $= 420,840$ suggest that deep ocean M_2 tide boundary layers on sloping topography are more unstable in the low Burger number limit (Figure 2-7), i.e. the stratified Stokes-Ekman boundary layer on a slope is more unstable than the ROBL. Presumably, holding all other parameters constant, as the Reynolds number increases the ROBL will transition to the fully turbulent regime.

Observations by Moum et al. (2004) of a subcritical slope, low Burger number, high Reynolds number boundary layer across the continental shelf off Oregon at 45°N depict a stratified Stokes-Ekman boundary layer on a slope remarkably similar to case 5. Although depth is shallow (50-150m) relative to abyssal depths, and therefore subject to surface effects, the non-dimensional parameter space of the boundary layer observed by Moum et al. (2004) is arguably close enough to a high Reynolds number version of case 5 for comparison. The values of the relevant non-dimensional parameters shown in Table 2.6 are estimated from the data reported by Moum et al. (2004) ($\nu = 1.0 \cdot 10^{-6}$ m^{2}s^{-1}, $\omega = 1.4 \cdot 10^{-4}$ s^{-1}, $f = 1.0 \cdot 10^{-4}$ s^{-1}, $N = 7.0 \cdot 10^{-3}$ s^{-1}, $U_\infty = 0.025$ ms^{-1}, and $\theta = 0.00670$).

Case	Re	Ro	C	ϵ	Bu	δ_{ul}/δ	N/N_{BL}
Moum et al. (2004)	3000	1.4	0.33	0.47	0.22	92	9.2
5	840	1.4	0.25	0.35	0.12	20	1.4

Table 2.6: Comparison of case 5 and Moum et al. (2004) parameters.

Figure 2-21 shows comparisons of the time mean law of the wall scaling for the dissipation rate of TKE , $\epsilon \approx u_*^3/(\kappa_{\mathrm{V}} z)$, and of time mean boundary layer anomalies in case 5 with ensemble means for the same quantities from Moum et al. (2004). As discussed in *The law of the wall* section, and evident in Figure 2-21, case 5 does not satisfy the wall law scaling for ϵ because Re $= 840$ appears to be on the cusp of the fully turbulent regime. The wall scaling for the dissipation rate for case 5 (the black solid line) is overpredicted because the log layer, or lack thereof, is not as turbulent as is implicitly assumed in the empirical scaling

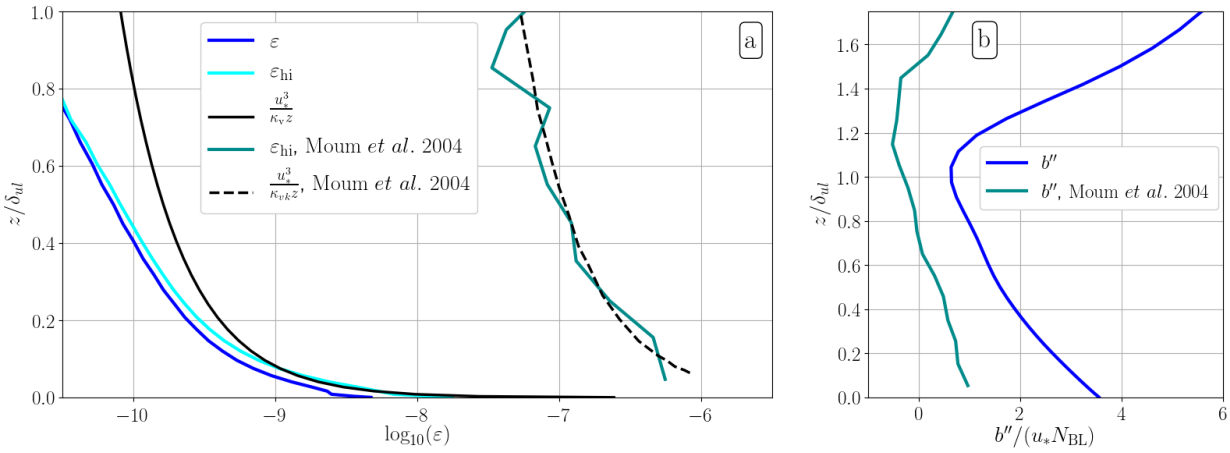

Figure 2-21: Comparison with observations by Moum et al. (2004). Despite three orders of magnitude difference between the dissipation rate (plot a), the boundary layer buoyancy anomaly structure is qualitatively similar (plot b).

relationship. The homogeneous, isotropic form of the dissipation rate of case 5 (the cyan line) disagrees with the true dissipation rate of case 5 near the wall, where the anisotropy of the boundary layer cannot be ignored. Moum et al. (2004) estimated the friction velocity via fitting to the dissipation rate curve; therefore, the agreement of the measured homogeneous, isotropic form of the dissipation rate of Moum et al. (2004) and the wall scaling near the wall ($z/\delta_{ul} < 0.4$, where δ_{ul} is the thickness of the "unstable layer") suggests that the law of the wall applies over some region within the observed boundary layer, but it is not clear how well the scaling is satisfied because the boundary layer anisotropy at z/δ_{ul} must produce ϵ measurment overpredictions by at least as much as the lower Reynolds number flow in case 5.

The plot b) of Figure 2-21 compares the buoyancy anomaly within the "unstable layer" at the bottom of the boundary layer. Here the buoyancy anomaly b'' is defined as the anomaly from the boundary layer ensemble mean buoyancy field, and N_{BL} is the ensemble mean boundary layer stratification. Both curves include the signature of a continual source of overturning: the fluid below $z/\delta_{ul} = 1.0, 1.2$ for case 5, Moum et al. (2004), respectively is lighter than the fluid above it. The anomalies are preserved because the density homogenization by the turbulence is not 100% efficient; indeed, the efficiency of the turbulence in case 5 is only 14%. Moum et al. (2004) argued that the observed boundary layer is generated by the downwelling associated with the surface Ekman transport, but also reports that there are

significant along- and across-slope semidiurnal tides that modulate the unstable temperature profiles and suggests that an Ekman response to the tidal period (a shorter time scale than the inertial period) is not expected. The dynamics of the stratified Stokes-Ekman layer on a slope in case 5 are a counter example to that argument: Ekman layer -type responses to the semidiurnal can form and generate gravitational instabilities.

2.4.2 Parameter space map

Figure 2-22 is a map of the dynamics that occurred in the Re = 840 simulations as a function of slope Burger number and slope parameter. In the lower left quadrant (Bu $< 1, \epsilon < 1$) is the fullly turbulent regime of case 5, in which the turbulence extracts energy from the mean shear throughout the entire period. At low slope Burger number, the buoyant restoring force projects primarily onto the vertical and therefore does not restore across- and along-isobath disturbances (e.g. u', v') as readily as it does at high slope Burger number, where the stratification stabilizes the shear of the boundary layer. At low Reynolds number (Re = 420, case 13) the fully turbulent layer did not develop in the simulations, therefore the fully turbulent region presumably shrinks/enlarges with decreasing/increasing Reynolds number. The experiments of MacCready and Rhines (1991) agree with the DNS in this study that, in general, the low Burger number regime is more unstable than the high Burger number regime. However, low slope Burger number flows on supercritical slopes were not examined in this study. At critical slope, the energy supplied to the BL is strongly nonlocal, and more directly tied to the baroclinic tide generation scales. Critical slope boundary layers were not investigated in this study, the interested reader is referred to the review of Sarkar and Scotti (2017).

The slope Burger number is the related to the ratio of baroclinic vorticity production to the planetary vorticity term in the vorticity budget of the ROBL linear flow solutions,

$$\frac{\partial \boldsymbol{\zeta}}{\partial t} = \mathrm{Ro}^{-1}(\zeta_2 \mathbf{i} - \zeta_1 \mathbf{j}) - \mathrm{C}^2 \partial_z b \mathbf{j} + \mathrm{Re}^{-1} \nabla^2 \boldsymbol{\zeta}. \tag{2.91}$$

Note that Equation 2.91 for the non-rotating case (Ro $\to \infty$) is purely one-dimensional: only the along-isobath vorticity, ζ_2, evolves. Rotation introduces a second component of

vorticity in the across-isobath direction, ζ_1. The ratio of the second term on the righthand side of Equation 2.91 to the first term on the righthand side of Equation 2.91 is BuRo^{-1}, which suggest that for constant, finite Rossby number and constant buoyancy frequency, increasing the slope angle (which increases $\mathrm{Bu} = N^2 \tan^2\theta / f^2$) makes the linear vorticity budget increasingly one-dimensional. This suggests that, holding all else constant, at large slope angle the along-isobath mean shear of linear flow is weaker and therefore less available for the production of turbulence. Indeed, the along-isobath velocity is proportional to the across-isobath velocity by the factor $\mathrm{Ro}^{-1} = f \cos\theta / \omega$, which also decreases with increasing θ.

While the shear instability the drives the fully turbulent boundary layer in case 5 (the low slope Burger number, $\mathrm{Re} = 840$, case), the boundary layer under the same conditions except for decreased Reynolds number (case 13) did not become turbulent. Perhaps unsurprisingly, this suggests that at low slope Burger numbers the turbulence strongly depends on the Reynolds number. The large slope Burger number cases are more stable to shear disturbances than the low slope Burger number cases, but presumeably also become fully turbulent at a critical Reynolds number that is larger than the Reynolds numbers investigated in this study. Gravitational instabilities are expected for a broad range of Reynolds numbers, but at low Reynolds numbers are not expected (for unity Prandtl number) because the negative boundary layer buoyancy gradient that gives rise to gravitational instabilities (Figure 2-6) is a function of the momentum deficit between the near wall flow and the flow just above it.

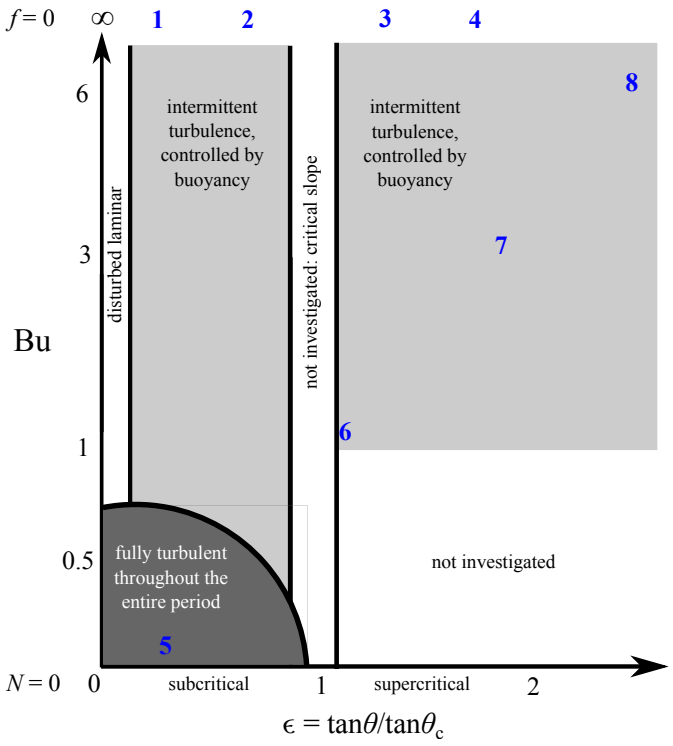

Figure 2-22: BTBL dynamical map at Re = 840.
The blue numbers correspond to the simulations of the same number.

2.5 Conclusions

In this chapter, a numerical investigation of the oscillating, stratified, viscous, diffusive boundary layers on infinite slopes in both rotating and non-rotating reference frames have been presented and discussed. The non-dimensional parameter space was chosen to make the study of interest to the oceanographic community, and the boundary layer anisotropy was calculated to provide the observational community an error estimate for conventional microstructure measurements within a meter of the seafloor.

The simulations and a quasi-steady boundary layer Rayleigh number estimate (see Figure 2-6) suggest that the OBLs and ROBLs are gravitationally unstable for much of the abyssal ocean slopes parameter space, excluding $\epsilon \lesssim 0.25$ and $\mathrm{Re} \lesssim 420$. The gravitational instabilities for rolls resemble the convective rolls of diabatic Couette flow and their formation can be attributed to the linear viscous/diffusive upslope flow dynamics. The boundary layer stratification significantly controls the transitional and intermittent regimes within $420 \lesssim \mathrm{Re} \lesssim 840$ by suppressing turbulence during the downslope flow phase to an extent that relaminarization

occurs and by triggering TKE production by the mean shear during the upslope flow phase. Increasing the slope parameter ϵ resulted in increases in turbulent burst intensity and also resulted in the growth of gravitational instabilities into positive turbulent buoyancy fluxes. The positive turbulent buoyancy fluxes eroded negative buoyancy gradients and thus acted as Fickian diffusive processes (a.k.a. downgradient). The turbulent bursts of the ROBL (Ro = 1.4) were found to be similar to the OBL bursts (although characterized by slightly larger turbulence intensities), except that at low Burger number ($\mathrm{Bu} = N^2 \tan^2\theta / f^2 \ll 1$) the fully turbulent boundary layers (turbulent throughout the entire period) formed, which bore many of the characteristics of observations of M_2 tide boundary layers.

The intermittent turbulent burst cases relaminarize before bursting at approximately the same time each oscillation, and therefore do not produce appreciable irreversible buoyancy flux convergence. However, the low Burger number case at Re = 840 (case 5), corresponding to a M_2 tide amplitude of just $U_\infty = 1$ cm s^{-1} in the abyss, steadily did work on the buoyancy field to raise the potential energy. The irreversible mixing efficiency was estimated for this case by calculating the potential energy change between the laminar flow (estimated by the linear solution) and the turbulent mean, and it was approximately 14%. While a 14% mixing efficiency does not stand out from other potential energy generating turbulent processes in the abyss, what is noteworthy is that the process occurs at a relatively low Reynolds numbers and low slope angles, which suggests that it may be applicable to large swaths of abyssal slopes. On the other hand, the diapycnal transport results suggest that the low Burger, low Reynolds number boundary layers have a negligible effect on the global overturning circulation because the boundary layers are $\mathcal{O}(1\text{ m})$ thick and therefore mix only a relatively small volume fluid.

The dissipation rates of TKE and drag coefficients increased with increased slope parameter, more for the OBL than the ROBL. The drag coefficient is dramatically reduced for Re < 840 flows on low angle slopes. The timing of the beginning of the burst was linked to decelerating, upslope, unstably stratified flow for all of the extra-critical Re = 840 flows. The majority of the turbulence in all cases was supplied with energy from the mean shear as opposed to the unstable stratification. The ROBL cases produced and dissipated more TKE because the mean flow tidal ellipse permitted the extraction of kinetic energy from

mean shear in the along-slope direction, in which there were no mean buoyancy gradients. It was also shown that calculations of the homogeneous, isotropic form of the dissipation rate of TKE may cause overpredictions of the true dissipation rate of roughly 100%, which demonstrates the significance of anisotropy in abyssal boundary layers, particularly in the near wall region of the flow.

Drag coefficients (Table 2.5), for the prediction of bottom grid cell dissipation in numerical models, were calculated for all simulations. The coefficients become quite small as the Reynolds number is decreased from 840 to 420, which suggests that a low Reynolds number cutoff threshold might be appropriate for numerical models that parameterize integrated boundary layer dissipation as $\epsilon \approx c_D|U|U^2$. In addition, the drag coefficients increased with slope angle, although the steepest slopes in this study are not found in the ocean at large scales (scales equal to or greater than k^{-1}).

Finally, although the boundary layers investigated here and other turbulence production mechanisms in the deep ocean are likely to interact in a nonlinear manner, the salient features of the boundary layers permit some speculation as to how the boundary layers might respond to turbulence produced by other sources. In general, events that weaken the stratification will make the value of C and the slope Burger number decrease, which increases the likelihood that turbulence will be sustained throughout the tidal cycle (viz. case 5) and decreases the intensity of the gravitational instability triggered burst of turbulence if $f \rightarrow 0$ (viz. case 1). Increasing the background stratification will have the opposite effect. The effect of strong mean flows (western boundary currents, hydraulic spills, etc) is too complicated for speculation.

Chapter 3

Floquet stability analysis

Gravitationally unstable boundary layers

In the direct numerical simulations (DNS) of the previous chapter, gravitational instabilities initiated two dimensional rolls that subsequently sheared apart into bursts of three-dimensional, shear driven turbulence. It was argued that the rolls were dynamically akin to the rolls that form from linear instabilities in gravitationally unstable Couette flow (Bénard and Avsec (1938), Chandra (1938), Brunt (1951), Deardorff (1965), Gallagher and A. Mercer (1965), Ingersoll (1966)), in which the boundary layer shear does not restrict gravitational instabilities seeded by disturbances in the plane perpendicular to the plane of the shear, and it was found that the bursts did not occur in the simulations if the nonlinear terms in the buoyancy equation were removed. In this chapter, the linear stability of the non-rotating boundary layers is calculated to determine if the gravitational instability is the primary linear instability across a much broader region of parameter space than can be sampled by DNS, and to determine the neutral stability curves for the gravitational instability.

Floquet instability theory versus instantaneous instability theory

The linear stability of oscillatory fluid flows is usually studied by introducing infinitesimal disturbances to the flow and then linearizing the governing equations about the oscillatory base flow to form governing equations for the growth of the infinitesimal disturbances. Since the base flow is mathematically represented as time-periodic coefficients in the disturbance

equations, spectral methods cannot be simply applied to determine the growth or suppression of disturbance modes. Instead, the linear stability is determined by applying instantaneous instability theory (IIT) or Floquet global instability theory.

IIT is the *ad hoc* application of conventional linear instability theory to examine the stability of the base flow at a discrete time (Von Kerczek and Davis (1976)). For example, in the case of Stokes' second problem (SSP, sometimes referred to as Stokes layers), the Orr-Sommerfeld equation is solved for the growth rates of disturbances to base flow at a chosen instant in the period. To evaluate the global stability, or stability over the entire period, the instantaneous stability calculation must be performed over many instants within the period. If one or more instantaneous modes exhibit positive growth rates throughout the period, then the flow is globally unstable according to IIT Luo and Wu (2010). However, the validity of the IIT approach rests on the assumption that the instantaneous growth rates are much larger than the frequency of the base flow, i.e. the quasi-steady flow assumption. Dwoyer and Hussaini (1987) showed that IIT is justifiable for the stability calculations for high Reynolds number, constant density flows because the instantantenous growth rates increase as a function of Reynolds number. However, low to moderate Reynolds number Stokes layer calculations by Luo and Wu (2010) showed that global stability estimates from IIT, which by definition fail to represent linear energy exchanges between instantaneous modes, are not predictive of linear global instabilities.

Floquet instability theory (Floquet (1883)) pertains to the net growth or suppression of instabilities over the course of one period. All periodic instantaneous globally unstable modes are unstable Floquet modes (Luo and Wu (2010), Dwoyer and Hussaini (1987)), but the opposite is not true: an unstable Floquet mode can correspond to linear energy exchange between two or more instantaneous modes that do not produce IIT global stability. Therefore the evolution of a Floquet mode over a period does not necessarily correspond to the evolution of an instantaneous instability that occurs during that period, but it does represent the global effect of linear instantaneous instabilities.

3.1 Floquet theory applied to vectors and tensors

In this section, the application of Floquet theory to vectors is summarized. The reader is referred to Iooss and Joseph (2012) for a complete explanation.

The principal fundamental solution matrix

In Floquet theory for vectors or tensors, the principal fundamental solution matrix is a mapping of the state vector $\mathbf{x}$ at time $t = 0$ to one period, $t = T$. Consider the non-autonomous system,

$$\frac{\mathrm{d}\mathbf{x}}{\mathrm{dt}} = \mathbf{A}(t)\mathbf{x}(t), \tag{3.1}$$

where $\mathbf{x}(t)$ is a vector and the operator $\mathbf{A}(t)$ is periodic

$$\mathbf{A}(t+T) = \mathbf{A}(t). \tag{3.2}$$

For a state vector $\mathbf{x}(t)$ of shape $[M \times 1]$, where M is the number of variables times the number of grid points, there exists a fundamental solution matrix $\mathbf{\Phi}(t)$ of shape $[M \times M]$ and coefficient vector $\mathbf{c}$ of shape $[M \times 1]$, such that

$$\mathbf{x}(t) = \mathbf{\Phi}(t)\mathbf{c}. \tag{3.3}$$

The fundamental solution matrix is a non-unique matrix in which the columns are the structure of the linearly independent solutions. The magnitude of the elements in $\mathbf{\Phi}$ depend on the choice of $\mathbf{c}$, and the only restriction to the choice of a tenable $\mathbf{c}$ is that $\mathbf{\Phi}$ be invertible. In that case, at time $t = 0$,

$$\mathbf{c} = \mathbf{\Phi}(0)^{-1}\mathbf{x}(0) \tag{3.4}$$

Substitution of Equation 3.4 into Equation 3.3 yields

$$\mathbf{x}(t) = \mathbf{\Phi}(t)\mathbf{\Phi}(0)^{-1}\mathbf{x}(0). \tag{3.5}$$

The principal fundamental solution matrix $\mathbf{\Phi}^*$ is just a fundamental solution matrix chosen such that at $t = 0$ it is an identity matrix:

$$\mathbf{\Phi}^*(0) = \mathbf{I}. \tag{3.6}$$

Substitution of Equation 3.6 in Equation 3.5 yields

$$\mathbf{x}(T) = \mathbf{\Phi}^*(T)\mathbf{x}(0); \tag{3.7}$$

therefore, the principal fundamental solution matrix at time $t = T$ maps the initial state $\mathbf{x}(0)$ to the final state after one period, $\mathbf{x}(T)$. By definition, Equation 3.1 can be written in terms of the principal fundamental solution matrix,

$$\frac{\mathrm{d}\mathbf{\Phi}^*}{\mathrm{dt}} = \mathbf{A}(t)\mathbf{\Phi}^*(t), \tag{3.8}$$

and so $\mathbf{\Phi}^*(T)$ can be obtained directly by integrating Equation 3.8 forward in time one period. The direct application of Floquet theory to a state vector describing a fluid flow has been used by Noack and Eckelmann (1994), Robichaux et al. (1999), and Barkley and Henderson (1996) to study instabilities in the periodic von Kármán vortex streets that develop in the wakes of cylinders.

Floquet stability

The innovation of Floquet (1883) was the recognition that, without a loss of generality, the initial conditions $\mathbf{x}(0)$ (Equation 3.7), can be expressed in terms of the eigenvectors of the principal fundamental solution matrix at time $t = T$, $\mathbf{\Phi}^*(T)$.

$$\mathbf{\Phi}^*(T)\mathbf{v}(0) = \boldsymbol{\mu}\mathbf{I}\mathbf{v}(0) \tag{3.9}$$

where $\boldsymbol{\mu}$ is a vector of the eigenvalues of $\mathbf{\Phi}^*(T)$ and $\mathbf{v}(0) = \mathbf{x}(0)$. By declaring the initial conditions in this manner, it follows that $\mathbf{v}(T) = \mathbf{x}(T)$. $\mathbf{v}(t)$ are the Floquet modes and $\boldsymbol{\mu}$

are the Floquet multipliers. Therefore,

$$\mathbf{v}(T) = \boldsymbol{\mu}\mathbf{I}\mathbf{v}(0), \tag{3.10}$$

is equivalent to Equation 3.7. The stability of the system in terms of Floquet multipliers is:

(a) If $\mu < 1$, then the Floquet mode decays as $t \to \infty$. If all of the multipliers $\boldsymbol{\mu}$ satisfy this property then the system is **stable**.

(b) If $\mu = 1$, then the Floquet mode is periodic, although not necessarily oscillating at the base freqency. If $\mu \pm 1 + 0i$ the mode is periodic with exactly the base period. If all modes in the system satisfy this property, then the system is **purely periodic**, for all time.

(c) If $\mu > 1$, then the Floquet mode will grow in amplitude as $t \to \infty$. If any of the multipliers $\boldsymbol{\mu}$ satisfies this property, then the system is **unstable** and initial disturbances will become infinitely large as $t \to \infty$.

Floquet multipliers are generally complex. For fluid flows, however, the component of interest is the real part of μ. The Floquet solutions are the columns of the principal fundamental solution matrix while the Floquet modes are defined by the Floquet exponents

$$\gamma = \frac{\log \mu}{T}, \tag{3.11}$$

where exponents are complex. The Floquet modes are defined

$$\mathbf{v}(t) = \mathrm{e}^{\mathrm{real}[\boldsymbol{\gamma}]t}\mathbf{P}(t)\mathbf{v}(0), \tag{3.12}$$

where $\mathbf{P}(t)$ are periodic Floquet mode components (harmonics of the base frequency). The real part of the Floquet exponents corresponds to the growth or decay of the mode as $t \to \infty$ and the imaginary part of the Floquet exponent determines the frequency of the Floquet mode.

3.1.1 Floquet modes & solutions

A state vector comprised of two variables, ζ and b, that are discretized onto a grid of two points, for example, takes the form

$$\mathbf{x}(t) = \begin{bmatrix} \zeta^{n=1}(t) \\ \zeta^{n=2}(t) \\ b^{n=1}(t) \\ b^{n=2}(t) \end{bmatrix}, \tag{3.13}$$

where the superscripts n denote the grid point of each variable. The principal fundamental solution matrix is

$$\mathbf{\Phi}^*(T) = \begin{bmatrix} \zeta^{n=1}_{m=1}(T) & \zeta^{n=1}_{m=2}(T) & \zeta^{n=1}_{m=3}(T) & \zeta^{n=1}_{m=4}(T) \\ \zeta^{n=2}_{m=1}(T) & \zeta^{n=2}_{m=2}(T) & \zeta^{n=2}_{m=3}(T) & \zeta^{n=2}_{m=4}(T) \\ b^{n=1}_{m=1}(T) & b^{n=1}_{m=2}(T) & b^{n=1}_{m=3}(T) & b^{n=1}_{m=4}(T) \\ b^{n=2}_{m=1}(T) & b^{n=2}_{m=2}(T) & b^{n=2}_{m=3}(T) & b^{n=2}_{m=4}(T) \end{bmatrix}, \tag{3.14}$$

where m denotes each column of linearly independent solutions.

The principal fundamental solution matrix at time $t = T$ can be analyzed to determine the variable and grid location of the fastest growing solution. At time $t = 0$ the principal fundamental solution matrix is an identity matrix (Equation 3.6). Since the initial disturbances occur only in the diagonal elements of $\mathbf{\Phi}^*(T)$, the grid location of the initial condition that gives rise to the fastest growing solution can be obtained by finding the initial condition of the column of maximum element at time T. For example, if $\max[|\mathbf{\Phi}^*(T)|] = b^{n=1}_{m=2}(T)$, then the mode with the most growth over one period is the second mode (column). The second column was initialized by a disturbance at the second grid point in ζ, therefore the maximum of that column, $b^{n=1}_{m=2}(T)$, occurred because of a initial disturbance at $\zeta^{n=2}_{m=2}(T)$.

3.2 Problem formulation

The Floquet stability of two vorticity components, the streamwise (ζ_1, pointing in the across-isobath x direction) and spanwise (ζ_2, pointing in the along-isobath y direction), are investigated in this study. The coordinate system, rotated angle θ counterclockwise from horizontal, and the vorticity components are shown in Figure 3-1. The streamwise vorticity "rolls," characterized by $|\zeta_1| > 0$, that appeared in the direct numerical simulations of the non-rotating oscillating boundary layer motivate an investigation of the stability of the streamwise vorticity, which appeared in all of the simulated bursts at Re = 840. For completeness, the stability of the spanwise vorticity is also investigated, because it collapses to the stability problem for Stokes' second problem as $C \to 0$.

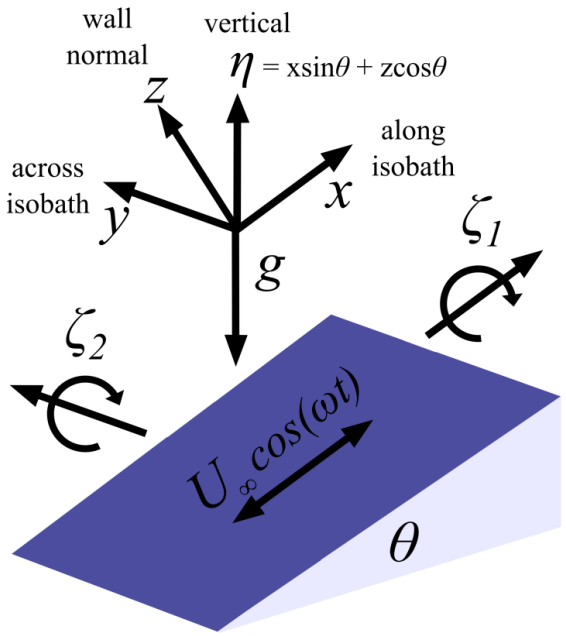

Figure 3-1: Coordinate system and vorticity components.

3.2.1 The base flow

The base flow is comprised of the oscillating components of the linear flow solutions discussed in the previous chapter and derived in the appendix. However, oscillatory boundary layers on adiabatic slopes oscillate relative to a non-zero steady flow. The steady flow can be

neglected in the stability analysis if the rate of modulation of the oscillating base flow is much faster than the spin up time of the steady component of the base flow. The ratio of the set up time scale of steady flow to the oscillation period indicates the significance of the steady flow regarding stability calculations of the oscillating component (Davis (1976)).

The transverse (i.e. diffusive) time scale of the steady laminar flow is the principle time scale of the base flow because the diffusion of the adiabatic boundary condition into the interior induces the boundary layer baroclinic vorticity and momentum. Following Dell and Pratt (2015), the transverse time scales of the non-rotating and rotating steady flows are

$$\tau_\kappa \sim \delta_0^2/\kappa, \tag{3.15}$$

$$\sim \frac{\sqrt{\mathrm{Pr}}}{N\sin\theta} \qquad \text{stationary reference frame,} \tag{3.16}$$

$$\sim \frac{2\mathrm{Pr}}{\sqrt{\mathrm{Pr}N^2\sin^2\theta + f^2\cos^2\theta}} \qquad \text{rotating reference frame,} \tag{3.17}$$

where the boundary layer thicknesses of the non-rotating steady boundary layer and the rotating steady boundary layer are, respectively:

$$\delta_0 = \left(\mathrm{Pr}\frac{N^2\sin^2\theta}{4\nu^2}\right)^{-1/4} \qquad \text{stationary reference frame,} \tag{3.18}$$

$$= \left(\frac{f^2\cos^2\theta}{4\nu^2} + \mathrm{Pr}\frac{N^2\sin^2\theta}{4\nu^2}\right)^{-1/4} \qquad \text{rotating reference frame.} \tag{3.19}$$

Therefore the modulation ratio (Davis (1976)) is

$$\mathcal{T}_M \sim \frac{\tau_\kappa}{\tau_\omega} = \frac{\omega\delta_0^2}{\kappa}. \tag{3.20}$$

In the limit of $\mathcal{T}_M \to \infty$, the time scales of the steady component of the base flow and the oscillating component of the base flow are sufficiently separated to be analyzed separately. If $\mathcal{T}_M \to 0$, the oscillating component varies so slowly relative to the steady flow set up time that the steady flow component may alter the instabilities of the oscillating component.

Typical abyssal parameter magnitudes for the M_2 tide are shown in Figure 3-2 for the oscillating base flow, using Equation 3.20, which shows that as $\theta \to 0$ the steady flow time scale is exceedingly long relative to the oscillating period. The plotted modulation ratio

for infinite Rossby number, Pr = 1 in Figure 3-2 indicates that the non-rotating oscillating boundary layer oscillates sufficiently fast relative to the steady flow, such that the steady flow component can be neglected in the Floquet analysis of the base flow. The modulation ratios for the rotating reference frame cases shown in Figure 3-2 indicate that the steady component of the flow may not be neglected in Floquet analysis of rotating reference frame cases.

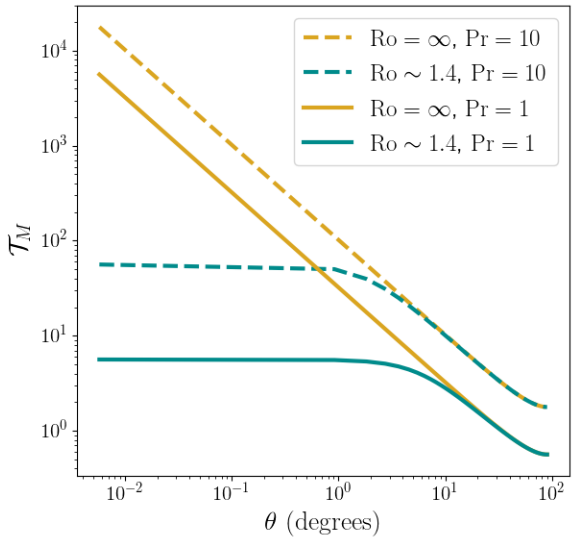

Figure 3-2: Modulation ratios.

3.2.2 Along-isobath vorticity governing equations

The derivation of the along-isobath (spanwise) vorticity governing equations follows that of Blennerhassett and Bassom (2002), except that new terms and an equation are added to include the effects of buoyancy. The total flow variables (denoted with tildes) are non-dimensionalized as follows:

$$\mathbf{x} = \frac{\mathbf{x}_\mathrm{d}}{\delta}, \quad \tilde{\mathbf{u}} = \frac{\tilde{\mathbf{u}}_\mathrm{d}}{U_\infty}, \quad t = \omega t_\mathrm{d}, \quad \tilde{p} = \frac{\tilde{p}_\mathrm{d}}{U_\infty^2}, \quad \tilde{b} = \frac{\omega \tilde{b}_\mathrm{d}}{N^2 U_\infty \sin\theta}, \tag{3.21}$$

where subscript d denotes dimensional variables, where $\tilde{p}$ is the mechanical pressure divided by the reference density ρ_0, and the buoyancy is $b = g(\rho_0 - \rho)/\rho_0)$. Note that the Eulerian time scale is not necessarily the same as the advective time scale (i.e. $U_\infty/\delta \neq \omega$). De-

composing the total prognostic variables into the basic (periodic, denoted by capitalization) state and infinitesimal disturbances (lower case, hatted):

$$\tilde{\mathbf{u}} = \mathbf{U} + \epsilon_0 \hat{\mathbf{u}}, \quad \tilde{b} = B + \epsilon_0 \hat{b}, \quad \tilde{p} = P + \epsilon_0 \hat{p}, \tag{3.22}$$

where

$$\epsilon_0 \ll 1, \tag{3.23}$$

and the basic state is comprised of the laminar flow solutions (see the Appendix). The two-dimensional flow governing equations for mass, momentum, and thermodynamic energy (buoyancy) for the disturbances in the $x - z$ plane are

$$0 = \partial_x \hat{u} + \partial_z \hat{w}, \tag{3.24}$$

$$\partial_t \hat{u} = -\frac{U\mathrm{Re}}{2}\partial_x \hat{u} - \frac{\hat{w}\mathrm{Re}}{2}\partial_z U - \frac{\mathrm{Re}}{2}\partial_x \hat{p} + \frac{1}{2}(\partial_{xx} + \partial_{zz})\hat{u} + \mathrm{C}^2 \hat{b}, \tag{3.25}$$

$$\partial_t \hat{w} = -\frac{U\mathrm{Re}}{2}\partial_x \hat{w} - \frac{\mathrm{Re}}{2}\partial_z \hat{p} + \frac{1}{2}(\partial_{xx} + \partial_{zz})\hat{w} + \mathrm{C}^2 \hat{b}\cot\theta, \tag{3.26}$$

$$\partial_t \hat{b} = -\frac{U\mathrm{Re}}{2}\partial_x \hat{b} - \frac{\partial_z B\mathrm{Re}}{2}\hat{w} + \frac{1}{2\mathrm{Pr}}(\partial_{xx} + \partial_{zz})\hat{b}, \tag{3.27}$$

where the Prandtl number, the Reynolds number, Stokes layer thickness, and slope frequency ratio are defined as they were in the direct numerical simulation chapter:

$$\mathrm{Pr} = \frac{\nu}{\kappa}, \tag{3.28}$$

$$\mathrm{Re} = \frac{U_\infty \delta}{\nu}, \tag{3.29}$$

$$\delta = \sqrt{\frac{2\nu}{\omega}}, \tag{3.30}$$

$$\mathrm{C} = \frac{N\sin\theta}{\omega}. \tag{3.31}$$

The vorticity component normal to the plane of the shear (i.e. in the along-isobath or y direction, see Figure 3-1) is defined

$$\hat{\zeta}_2 = \partial_z \hat{u} - \partial_x \hat{w}. \tag{3.32}$$

Let the infinitesimal disturbances take the form of a normal mode decomposition in the across-isobath (streamwise) direction:

$$\hat{\zeta_2}(x,z,t) = \zeta_2(z,t)\mathrm{e}^{ikx} \; + \; \text{complex conjugate}, \tag{3.33}$$

$$\hat{b}(x,z,t) = b(z,t)\mathrm{e}^{ikx} \; + \; \text{complex conjugate}, \tag{3.34}$$

where the modal streamfunction ψ, modal velocities, and across-isobath (streamwise) disturbance wavenumber are defined:

$$\zeta_2 = (\partial_{zz} - k^2)\psi, \tag{3.35}$$

$$(u,w) = (\partial_z\psi, -ik\psi), \tag{3.36}$$

$$k = k_\mathrm{d}\delta = \frac{2\pi}{\lambda}\delta, \tag{3.37}$$

where k is the non-dimensional wavenumber, k_d is the dimensional wavenumber, and λ is the dimensional wavelength of the infinitesimal amplitude disturbance. The vorticity equation for the spanwise vorticity disturbance modes

$$\partial_t\zeta_2 = \underbrace{\frac{\left(\partial_{zz} - k^2\right)}{2}\zeta_2}_{\substack{\text{diffusion}}} - \underbrace{\frac{Uik\mathrm{Re}}{2}\zeta_2}_{\substack{\text{base}\\\text{advection}}} + \underbrace{\frac{(\partial_{zz}U)ik\mathrm{Re}}{2}\psi}_{\substack{\text{advection of base}\\\text{vorticity by disturbances}}} + \underbrace{\mathrm{C}^2\left(\partial_z - ik\cot\theta\right)b}_{\substack{\text{baroclinic}\\\text{production of vorticity}}}, \tag{3.38}$$

is obtained by taking the curl of the momentum (Equations 3.25 and 3.26) and by substitution of disturbance modes (Equations 3.33 and 3.34). In the same manner, the buoyancy equation for the buoyancy disturbance modes

$$\partial_t b = \underbrace{\frac{\left(\partial_{zz} - k^2\right)}{2\mathrm{Pr}}b}_{\substack{\text{diffusion}}} - \underbrace{\frac{Uik\mathrm{Re}}{2}b}_{\substack{\text{base}\\\text{advection}}} + \underbrace{\frac{(\partial_z B)ik\mathrm{Re}}{2}\psi}_{\substack{\text{advection of}\\\text{base buoyancy}}}. \tag{3.39}$$

Note that if $\mathrm{C} \to 0$, then Equation 3.38 is identical to the vorticity mode equation for Stokes' second problem (Blennerhassett and Bassom (2002)). The evolution equations for the spanwise vorticity disturbance modes (Equations 3.38 and 3.39) can be expressed in the

form of the non-automous system in Equation 3.1. In that case, the state vector is

$$\mathbf{x} = \begin{bmatrix} \zeta_2 \\ b \end{bmatrix}, \tag{3.40}$$

and the dynamical operator is

$$\mathbf{A} = \begin{bmatrix} \frac{(\partial_{zz}U)ik\mathrm{Re}(\partial_{zz}-k^2)^{-1}}{2} - \frac{Uik\mathrm{Re}}{2} + \frac{(\partial_{zz}-k^2)}{2} & \mathrm{C}^2(\partial_z - ik\cot\theta) \\ \frac{(\partial_z B)ik\mathrm{Re}(\partial_{zz}-k^2)^{-1}}{2} & -\frac{Uik\mathrm{Re}}{2} + \frac{(\partial_{zz}-k^2)}{2\mathrm{Pr}} \end{bmatrix}, \tag{3.41}$$

where the inversion of the discrete matrix $(\partial_{zz} - k^2)$ is used to calculate the steamfunction from vorticity in the state vector. The ∂_{zz} matrix is formed by using central finite differences to generate a mostly tridiagonal matrix (except for the boundary conditions, which have off-diagonal terms) and the discrete matrix for the given wavenumber k is just k times an identity matrix. Both the discrete matrices for ∂_{zz} and k have the dimensions $[N_z \times N_z]$, where N_z is the number of grid points in z. Therefore $\mathbf{A}$ has the dimensions $[M \times M]$ where $M = N_z \cdot N_v$ and where N_v is the number of variables. Since are just two variables, ζ_2 and b, $\mathbf{A}$ has the dimensions $[2N_z \times 2N_z]$.

3.2.3 Across-isobath vorticity governing equations

The procedure for the derivation of evolution of streamwise vorticity modes is nearly identical to that for spanwise vorticity modes, except that the spanwise component of momentum $\hat{v}$ has been substituted for the streamwise component of momentum $\hat{u}$. The governing equations for the disturbances are

$$0 = \partial_y \hat{v} + \partial_z \hat{w}, \tag{3.42}$$

$$\partial_t \hat{v} = -\frac{\mathrm{Re}}{2}\partial_y \hat{p} + \frac{1}{2}(\partial_{yy} + \partial_{zz})\hat{v}, \tag{3.43}$$

$$\partial_t \hat{w} = -\frac{\mathrm{Re}}{2}\partial_z \hat{p} + \frac{1}{2}(\partial_{yy} + \partial_{zz})\hat{w} + \mathrm{C}^2\hat{b}\cot\theta, \tag{3.44}$$

$$\partial_t \hat{b} = -\Big(\frac{\mathrm{Re}\partial_z B}{2}\Big)\hat{w} + \frac{1}{2\mathrm{Pr}}(\partial_{yy} + \partial_{zz})\hat{b}. \tag{3.45}$$

Note that if $\partial_x = 0$, then the disturbance governing equations above are valid for three dimensional flow and a purely diagnostic governing equation for u is valid as well,

$$\partial_t \hat{u} = \frac{1}{2}(\partial_{yy} + \partial_{zz})\hat{u} + \mathrm{C}^2 \hat{b}. \tag{3.46}$$

The streamwise vorticity component (see Figure 3-1) is defined:

$$\hat{\zeta}_1 = \partial_y \hat{w} - \partial_z \hat{v}. \tag{3.47}$$

Let the infinitesimal disturbances take the form of a normal mode decomposition in the spanwise (y) direction:

$$\hat{\zeta_1}(y,z,t) = \zeta_1(z,t)\mathrm{e}^{ily} \ + \ \text{complex conjugate}, \tag{3.48}$$

$$\hat{b}(y,z,t) = b(z,t)\mathrm{e}^{ily} \ + \ \text{complex conjugate}, \tag{3.49}$$

where the modal streamfunction ψ and modal velocities are defined

$$\zeta_1 = (\partial_{zz} - l^2)\psi, \tag{3.50}$$

$$(v, w) = (-\partial_z \psi, il\psi). \tag{3.51}$$

Finally the governing equation for the evolution of the streamwise vorticity modes is

$$\partial_t \zeta_1 = \underbrace{\frac{(\partial_{zz} - l^2)}{2}\zeta_1}_{\text{diffusion}} \ + \ \underbrace{il\mathrm{C}^2 \cot\theta b}_{\substack{\text{baroclinic} \\ \text{production of vorticity}}}, \tag{3.52}$$

and the governing equation for the evolution of the associated buoyancy is

$$\partial_t b = \underbrace{\frac{\left(\partial_{zz} - l^2\right)}{2\mathrm{Pr}} b}_{\text{diffusion}} - \underbrace{\frac{(\partial_z B) il \mathrm{Re}}{2}\psi}_{\substack{\text{advection of} \\ \text{base buoyancy}}}. \tag{3.53}$$

There are no terms representing the advection of disturbances by the base flow in Equations 3.52 and 3.53, nor the advection of base vorticity by vorticity disturbances. The basic

state flow enters the equations only through the advection of base buoyancy by the buoyancy disturbances; therefore, disturbance vorticity can only be produced by gravitational instabilities. The state vector for Equations 3.52 and 3.53 is

$$\mathbf{x} = \begin{bmatrix} \zeta_1 \\ b \end{bmatrix}, \tag{3.54}$$

and the dynamical operator is

$$\mathbf{A} = \begin{bmatrix} \frac{(\partial_{zz} - l^2)}{2} & \mathrm{C}^2 il \cot\theta \\ -\frac{(\partial_z B) il \mathrm{Re}(\partial_{zz} - l^2)^{-1}}{2} & \frac{(\partial_{zz} - k^2)}{2\mathrm{Pr}} \end{bmatrix}. \tag{3.55}$$

3.2.4 Boundary conditions

The oscillatory forcing was imposed by imposing a "moving wall" boundary condition rather than apply a body force directly on the evolving modes. At the moving wall, the total flow boundary conditions on the momentum are no-slip and impermeable; therefore, at $z = 0$

$$\tilde{\mathbf{u}} = U\mathbf{i} + \epsilon_0 \hat{\mathbf{u}} = \cos(t)\mathbf{i}, \tag{3.56}$$

where by definition of the basic flow

$$U(0,t) = \cos(t), \tag{3.57}$$

therefore

$$\partial_z \psi = 0, \tag{3.58}$$

is required to satisfy the no-slip condition at $z = 0$ for either definition of the streamfunction. The streamfunction must be constant along an impermiable wall; therefore,

$$\psi = 0, \tag{3.59}$$

at $z = 0$ will satisfy $w = \partial_x \psi = 0$ for the spanwise vorticity - streamfunction approach or $w = \partial_y \psi = 0$ for the streamwise vorticity - streamfunction approach.

The wall is adiabatic; therefore,

$$\partial_z \tilde{b} = \partial_z B + \epsilon_0 \partial_z \hat{b} = 0. \tag{3.60}$$

Since the basic state stratification satisfies

$$\partial_z B = 0, \tag{3.61}$$

then the disturbance stratification must satisfy

$$\partial_z \hat{b} = 0, \tag{3.62}$$

at $z = 0$.

At $z \to \infty$, the conventional boundary conditions for SSP are parallel and irrotational flow. Parallel flow is ensured if

$$\psi = 0, \tag{3.63}$$

at $z \to \infty$. The flow is irrotational if

$$\zeta_1 = 0, \quad \text{or} \quad \zeta_2 = 0, \tag{3.64}$$

at $z \to \infty$ for the streamwise and spanwise vorticities, respectively. The background stratification is not adiabatic in the far field but the disturbance stratification can be adiabatic because the basic flow gradients exist only in the boundary layer. Therefore, at $z \to \infty$

$$\partial_z b = 0. \tag{3.65}$$

3.3 Numerical procedures

3.3.1 Discretization schemes

As described in the *Floquet modes & solutions* section, the discrete principal fundamental solution matrices are dimensioned $N_v \times N_z$, where N_v is the number of variables and N_z is the

number of grid points. In both streamfunction-vorticity formulations in this study $N_v = 2$ for vorticity and buoyancy. The number of grid points in z, the wall-normal direction, for all calculations was $N_z = 200$. The variables were computed at the cell centers of a uniform grid of height $H/\delta = 32$, where the non-dimensional grid encompassed $z = [0, H/\delta]$. Previous studies found that Floquet stability calculations for SSP were unaffected by an upper domain boundary as long as it was located at $H/\delta = 32$ or greater (Blennerhassett and Bassom (2006), Luo and Wu (2010)).

Centered second-order finite difference schemes were used to compute the discrete forms of all first and second derivatives and the vorticity inversions that appear the dynamical operator $\mathbf{A}$ for the spanwise vorticity formulation (Equation 3.41) and the streamwise vorticity formulation (Equation 3.55). To implement the no-slip, impermeable boundary conditions at the wall (Equations 3.58, 3.59), the streamfunction and its z derivative were set to zero. However, to guarantee unique solutions at second-order accuracy, the vorticity at the wall was required to compute the second derivatives of the vorticity. The second-order accuracy was confirmed with grid convergence tests shown in Appendix B. A second-order accurate extrapolation of the vorticity at the wall that accounts for no-slip and impermeable boundary conditions was derived by (Woods (1954)) for this purpose. The Woods (1954) boundary condition is:

$$\zeta^{n=0} = \frac{3}{\Delta z^2}\psi^{n=1} - \frac{1}{2}\zeta^{n=1}, \tag{3.66}$$

where the superscript $n = 0$ denotes the variable is located at the wall and the superscript $n = 1$ denotes that the variable is located at the first cell center. All of the other boundary conditions (Equations 3.62, 3.63, 3.64, and 3.65) were readily implemented into the discrete derivatives within the discrete operators $\mathbf{A}$. Finally, test functions were used to ensure that the truncation error for all discrete derivative and inversions decreased with $(\Delta z)^{-2}$, where Δz is the height of a grid cell.

To obtain the principal fundamental solution matrix at time $t = T$, Equation 3.8 was integrated over one period with the standard explicit fourth order Runge-Kutta time advancement method, equivalent to simultaneously solving the evolution of the state vector in Equation 3.1 in which each linearly independent solution begins with a different initial con-

dition. The method for computing the principal fundamental solution matrix in this study is formally second-order accurate.

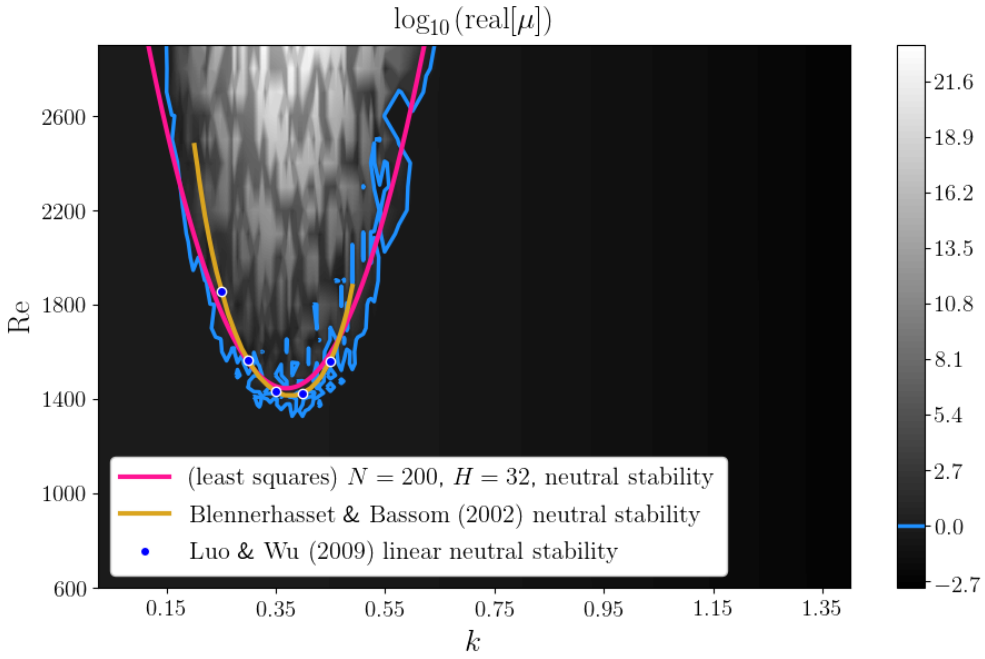

Figure 3-3: The neutral stability curve for Stokes' second problem. Verification of spatial discretization, temporal discretization, and eigenvalue calculation. The computed Floquet multipliers are shown by the gray shading, and the calculated real$[\mu] = 1$ contour is represented with the blue line.

The neutral stability curve for SSP was computed as a code verification test, shown in Figure 3-3. In Figure 3-3 the blue line is the computed stability curve, and the pink line is a least squares fit of the computed stability curve. The yellow line is a least squares fit of the computed stability curve by Blennerhassett and Bassom (2002), who used a spectral method for the computation, and the blue dots were calculated by linearized direct numerical simulations by Luo and Wu (2010). The variations in the neutral stability curve about the pink line can be attributed to the spatial discretization method. This was proved by computing the neutral stability curve for Mathieu's equation (Figure 3-4, the zero contour lies beneath the curve of Kovacic et al. (2018)), which has no spatial derivatives and was computed to graphical accuracy using the same code for time integration and eigenvalue calculation.

The variations of the neutral stability curve in Figure 3-3 occur because of the initialization of the principal fundamental solution matrix as an identity matrix. In the first time

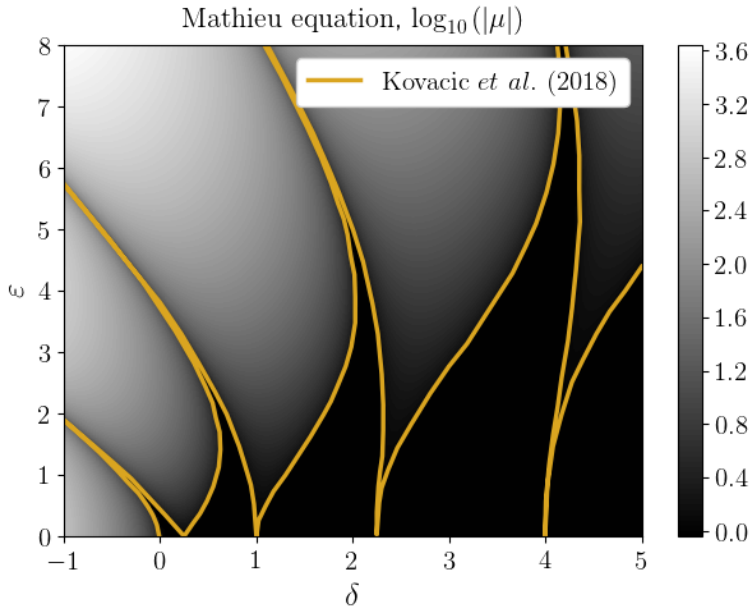

Figure 3-4: The neutral stability curve for Mathieu's equation.
Verification of the temporal discretization scheme and the eigenvalue calculation. The computed Floquet multipliers are shown by the gray shading, and the real$[\mu] = 1$ contour lies under the yellow line of Kovacic et al. (2018) to graphical accuracy.

step of the calculation, the finite differencing of discontinuous functions (specifically Dirac delta functions) introduces discretization errors that do not converge with increased grid resolution. To check this, the stability of SSP was computed for varied Reynolds number and grid resolution at $k = 0.35$, shown in Figure 3-5. The Floquet multipliers in Figure 3-5 that correspond to stable points in the neutral stability plot of Figure 3-3 converge quickly with increasing grid resolution. However, for $\mathrm{Re} \geq 1400$, $k = 0.35$ (inside the unstable region of Figure 3-3) the multipliers in Figure 3-5 do not converge with increasing grid resolution. Luo and Wu (2010) pointed out that SSP stability calculations are extremely sensitive to transient noise that occurs during the course of the oscillation, which suggests that small round-off errors and other numerical noise may explain the variations of the stability curve fit calculated by Blennerhassett and Bassom (2002). Figure 3-5 indicates that the primary culprit for transient noise in the present study is the introduction of discretization errors at the first time step. Therefore the $N_z = 200$ was deemed sufficient grid resolution, and the calculated neutral stability curves from a finite difference method must be considered approximate rather than exact.

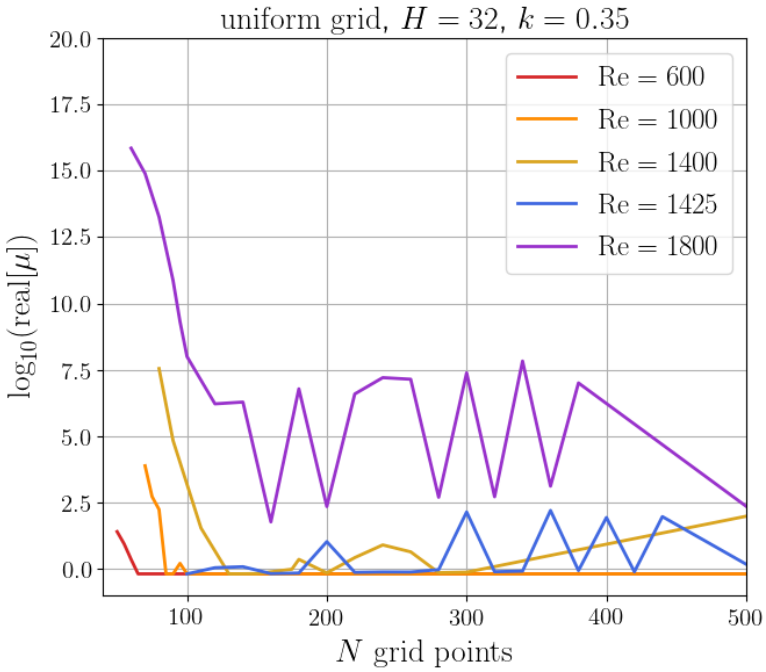

Figure 3-5: Grid convergence occurs only for stable calculations.
Stable Floquet multiplier calculations achieve grid convergence. Near the neutral stability curve, the Floquet multiplier calculations fail to acheive grid convergence because finite differences of the identity matrix initial condition of the principal fundamental solution matrix introduce grid independent noise. Therefore the "wiggles" of the blue curve in Figure 3-3 are due to the sensitivity of the multiplier value to noise introduced at just after $t = 0$ when finite differences are taken of discontinuities in the principal fundamental solution matrix.

3.4 Results and discussion

3.4.1 The along-isobath vorticity component

For the along-isobath (spanwise) disturbance vorticity, ζ_2, and accompanying disturbance buoyancy, the Floquet neutral stability curves transition from a curve resembling that of SSP at low $\mathrm{C} = N \sin\theta/\omega$ to that of a curve for a low Reynolds number instability at large subcritical slopes (as $\mathrm{C} \to 1$ from below) and finally to that of a curve for a large disturbance wavelength instability at supercritical slopes ($\mathrm{C} > 1$). Figure 3-6 shows the subcritical slope stability curves (where the neutral curve is the zero contour of the log of the largest real Floquet multipliers, shown in pink) as functions of streamwise wavenumber k and Stokes Reynolds number, Re. At $\mathrm{C} = N \sin\theta/\omega = 1/8$ the minimum of the approximately parabolic neutral stability curve appears at $\mathrm{Re} \approx 1400$, $k \approx 0.35$, similar to the stability curve for SSP

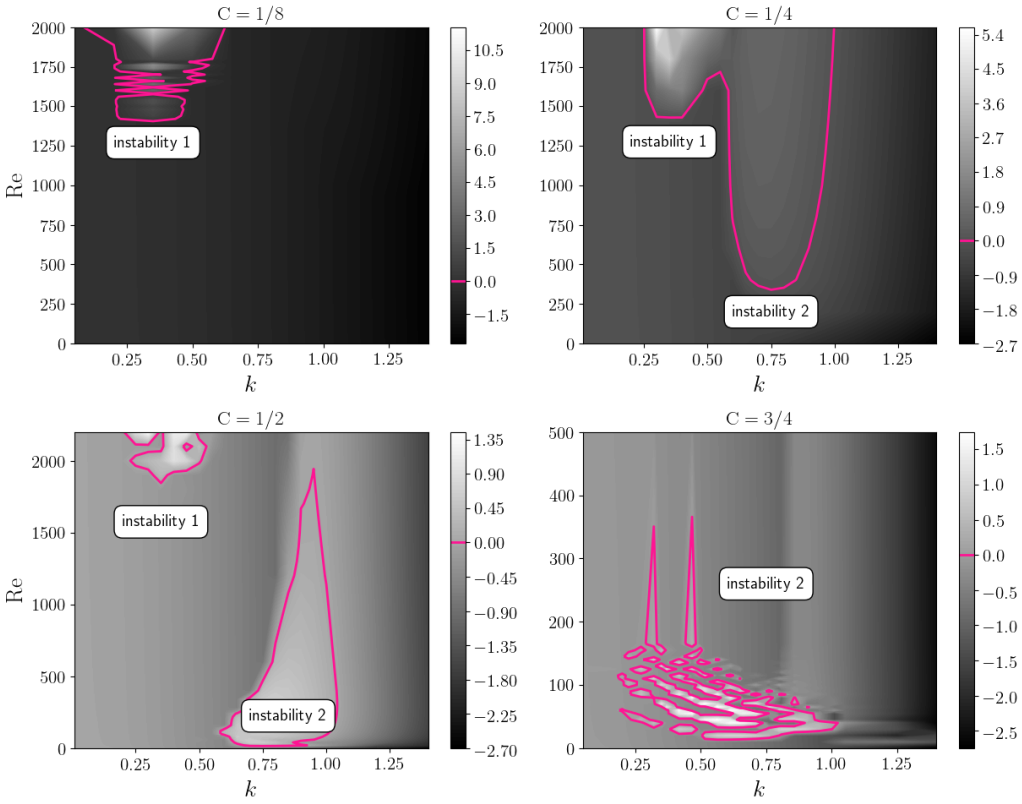

Figure 3-6: $\log_{10}(\text{real}[\mu])$ for ζ_2, subcritical slopes.

shown in Figure 3-3. A second instability forms as C increases, and can be seen dripping down from high Reynolds number to low Reynolds number as C increases 1/4 to 3/4 above $k \approx 0.75$ in Figure 3-6.

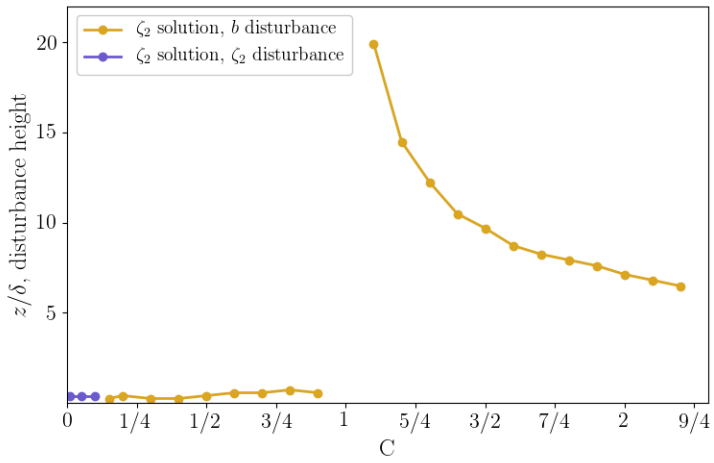

Figure 3-7: Initial conditions of the fastest growing solutions.

To illustrate the connection of the low C cases to the SSP stability curve, the height (z) and variable (ζ_2 or b) of the initial disturbance of the absolute largest real element of the solution matrix are shown in Figure 3-7 for Re $= 1300$, $k = 0.35$. The height and initial variable that produced the solution that grew the fastest was determined by the location of the maximum value in the solution matrix, as described previously in the *Floquet modes & solutions* section. For all cases in Figure 3-7, the spanwise vorticity ζ_2 is the most amplified solution component, and for most of the range of C evaluated, the solution that grew the most was seeded by a buoyancy disturbance. However, as C $\to 0$, the initial disturbance that gave rise to the largest amplitude solution is also the spanwise vorticity. The evolution of normalized spanwise vorticity budget terms and relevant base flow terms for C $= 0.01, \mathrm{Re} = 1300, k = 0.35$ are plotted as contours in Figure 3-8, which shows that the baroclinic production of vorticity is 1/100 the magnitude of the advection of vorticity by the base flow. In addition, the amplification by the advection of vorticity occurs during the flow reversal in the outer boundary layer, which is known to occur in SSP (Luo and Wu (2010)). In summary, the buoyancy disturbance becomes passive as the vorticity and buoyancy uncouple in the limit as C $\to 0$.

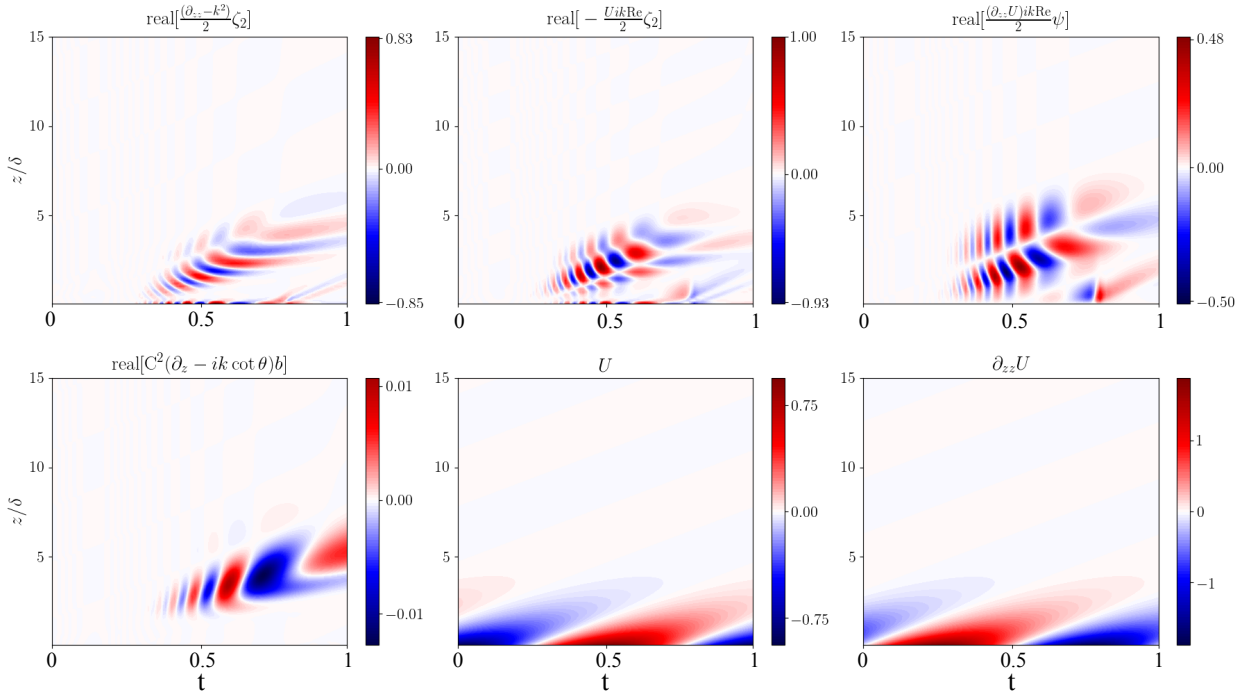

Figure 3-8: ζ_2 budget terms and base flow for C $= 0.01, \mathrm{Re} = 1300, k = 0.35$.

Since Floquet modes can represent superpositions of instantaneous linear modes, the direct interpretation of individual Floquet modes can be ambiguous. Therefore, to interpret the dynamics of the instabilities present in Figure 3-6, temporally and spatially integrated diagnostics may mitigate the interpretation problem. Figure 3-9 shows the time- and z-integrated vorticity budget (left, Equation 3.38) and buoyancy budget (right, Equation 3.39) terms for $\mathrm{Re} = 1300, k = 0.35$. The absolute value of each term in each budget is divided by the largest absolute term in order to plot each term's relative contribution to the Floquet modes. The vorticity budget in Figure 3-9 suggests that the two instabilities shown in the neutral stability curves of Figure 3-6 are not dynamically distinct from SSP for $\mathrm{C} < 3/4$. In that range, the fastest growing mode is vorticity and its growth is attributable primarily to the base advection of vorticity disturbances and the advection of base vorticity by the disturbances; baroclinic production of vorticity is weak. At $\mathrm{C} = 3/4$ the base advection is still the dominant term in the budget of the dominant variable, but the baroclinic production of vorticity is significant. The plot on the right of Figure 3-9 suggests that for subcritical flows where $\mathrm{C} > 1/4$, the dominant buoyancy Floquet modes are those that correspond to the advection of the base flow stratification by the disturbances. Figure 3-9 indicates that the two instabilities that are apparent in Figure 3-6 are in fact a continuum from a SSP boundary layer to a SSP-like boundary layer in which the vorticity modes are increasingly stabilized by buoyancy with increasing slope.

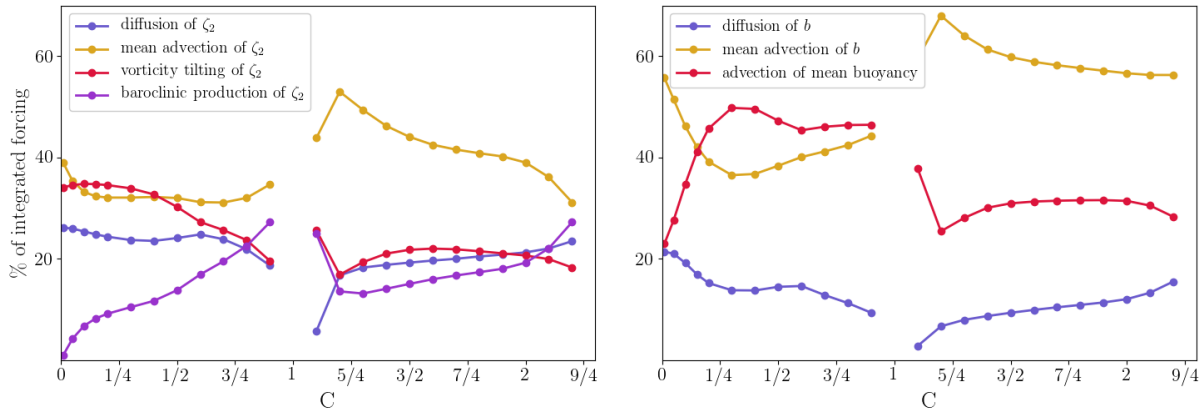

Figure 3-9: Integrated ζ_2, b, budgets for $\mathrm{Re} = 1300, k = 0.35$.
Percentages are calculated from the sum of all space and time integrated budget components for a given C (the sum of all terms at each C is 100).

For supercritical slopes, the low Reynolds number pocket of instability visible in the case of C = 3/4 in Figure 3-10 becomes an instability that nearly encompasses all of the parameter space of $k < 1$ for all Reynolds numbers investigated. The most unstable solutions are the vorticity solutions (Figure 3-7), and the advection of the disturbances by the base flow dominates both budgets (Figure 3-9). Since the supercritical flow instability is primarily forced by the base flow velocity U (e.g. the advection of disturbances by the base flow is the largest vorticity budget term in Figure 3-8 and in the supercritical regime of Figure 3-9), nearly independent of Reynolds number, and preferentially selects low wavenumbers, the instability may be of inviscid (inflectional) origin.

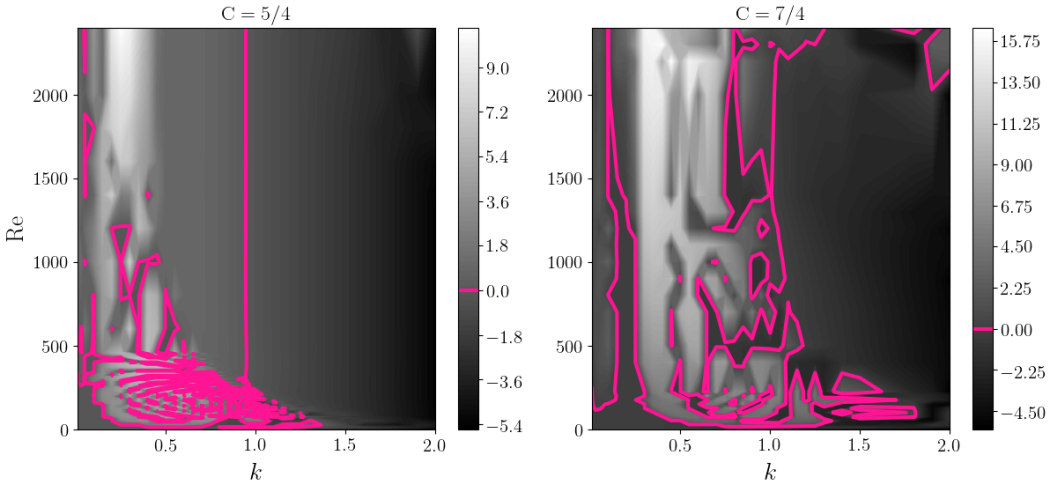

Figure 3-10: $\log_{10}(\text{real}[\mu])$ for ζ_2, supercritical slopes.

3.4.2 The across-isobath vorticity component

The Floquet neutral stability curves for the across-isobath (streamwise) disturbance vorticity, ζ_1, and accompanying disturbance buoyancy, outline broader regions of unstable parameter space than the spanwise vorticity disturbances in the previous section. Figures 3-11 and 3-12 show the stability curves for subcritical and supercritical slopes, respectively. However, the minima of neutral stability curves are significantly higher than the approximate stability criteria of Hart (1971):

$$\frac{2\mathrm{Re}}{\sqrt{|1-\mathrm{C}^2|}} \ll 1, \tag{3.67}$$

presumably because the criteria of Hart (1971) was derived for oscillating stratified boundary layer laboratory experiments at $\mathrm{Pr} \ll 1$. Indeed, the spanwise vorticity disturbance equations (Equations 3.52 and 3.53) indicate that for $\mathrm{Pr} \ll 1$ the instability can only be seeded by vorticity disturbances and can only be suppressed by the diffusion of vorticity. The only component of the base flow that appears in the disturbance equations (Equations 3.52 and 3.53) is the oscillating base flow stratification, $\partial_z B$, so the only source term for the growth of instabilities is the term in the buoyancy equation that represents the advection of the base flow buoyancy by a wall-normal disturbance, $w\partial_z B$. The wall-normal structure of the base flow stratification is independent of the Reynolds number, but its amplitude is not, hence the Floquet multiplier variation as a function of Reynolds number in Figures 3-11 and 3-12.

Note that in the limits of $N/\omega \to 0$ and/or $\theta \to 0$ the baroclinic production of vorticity term in the streamwise vorticity equation vanishes. In that limit, the disturbance equations uncouple and the flow must be Floquet stable, regardless of the base flow magnitude. This is the case in Figure 3-14, which shows the temporally and spatially integrated streamwise vorticity and buoyancy budget terms as percentages of the total forcing of disturances. For both $\mathrm{C} < 1$ and $\mathrm{C} > 1$, the integrated buoyancy budget is dominated by the advection of the base flow buoyancy, the vorticity budget is dominated by the baroclinic production terms, and as $\mathrm{C} \to 0$ diffusion stabilizes both vorticity and buoyancy disturbances.

The origin of the fastest growing solutions are shown in Figure 3-13 for $\mathrm{Re} = 420$, $l = 1.0$, which shows that the fastest growing solutions for subcritical slopes are buoyancy solutions

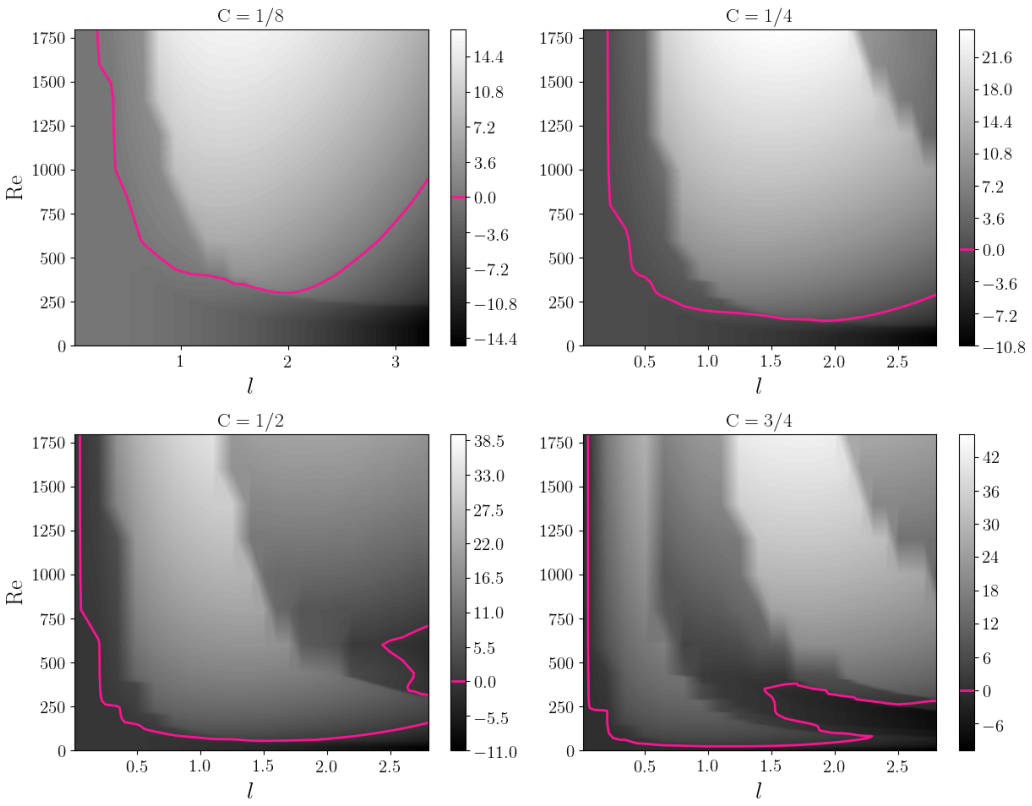

Figure 3-11: $\log_{10}(\text{real}[\mu])$ for ζ_1, subcritical slopes.

arising from initial buoyancy disturbances. This suggests that for small C, Re = 420, and $l = 1.0$, as an initial buoyancy disturbance associated with the most unstable mode diffuses, it produces a small but sufficient amount of baroclinic vorticity to produce a global instability associated with the advection of the base flow buoyancy by the disturbance.

The fastest growing solutions in Figure 3-13 also indicate that as C increases, so does the coupling of the buoyancy instability and the baroclinic production of vorticity. The fastest growing solutions for supercritical slopes shown in Figure 3-13 are streamwise vorticity solutions seeded by vorticity disturbances because the base flow stratification $\partial_z B$ undergoes a rapid jump in amplitude during the transition from subscritical to the supercritical slope and continues to increase with increasing supercriticality. For constant N/ω, constant disturbance wavenumber l, and constant base flow amplitude $\partial_z B$, the non-dimensional scale the baroclinic production of vorticity , $\mathrm{C}^2 \cot\theta = N^2\omega^{-2}\sin\theta\cos\theta$, is largest at $\theta = \pi/4$, so over the range of slope angles considered in this study (approximately $0 < \theta \leq \pi/12$) the

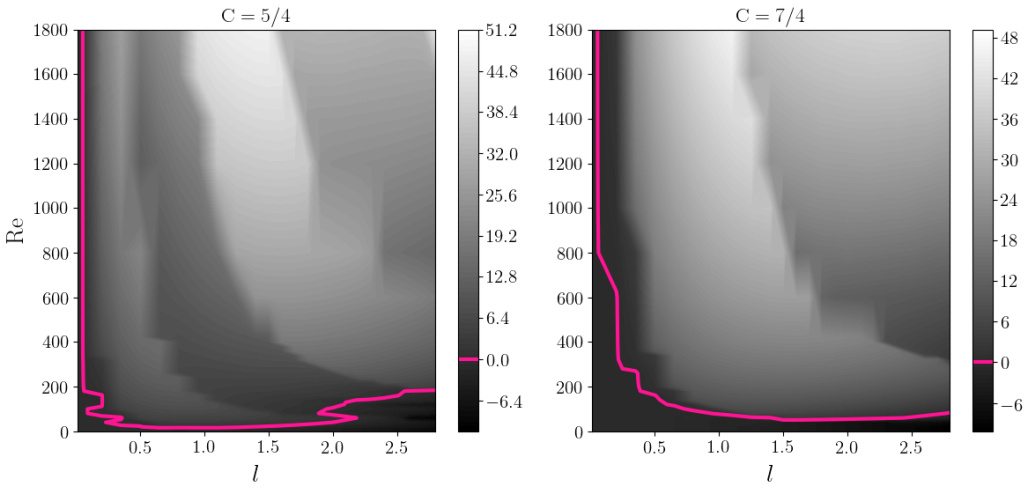

Figure 3-12: $\log_{10}(\text{real}[\mu])$ for ζ_1, supercritical slopes.

coefficient of baroclinic production increases with slope angle. However, the neutral stability curves in Figures 3-11 and 3-12 approach the origin as C approaches critical from above and below because the amplitude and thickness of the base flow boundary layer increases as $\text{C} \to 1$, particularly when C approaches unity from above. Increasing C and/or θ increases the coupling of the disturbance equations, and the global instability is most pronounced where the base flow stratification amplitudes are largest.

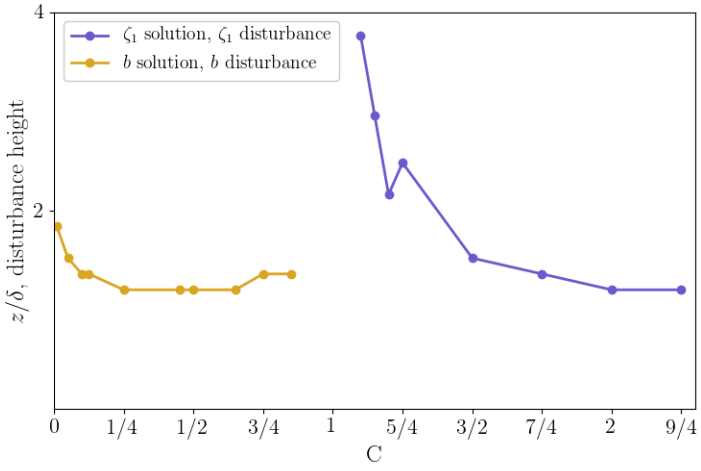

Figure 3-13: Initial conditions of the fastest growing solutions.

The DNS of $\text{C} = [1/4, 3/4, 5/4, 7/4]$ at $\text{Re} = 420$ were found to be globally stable and only the $\text{C} = 1/4$ simulation developed a transient instability. The DNS was seeded with three-dimensional white noise disturbances to the buoyancy field at the grid scale, characterized

by the Nyquist spanwise and streamwise wavenumbers of $k = 0.92$ and $l = 0.92$. However, the neutral stability curves in Figures 3-11 and 3-12 indicate global instabilities should occur at Re $= 420$, $l = 0.92$ for C $= [1/4, 3/4, 5/4, 7/4]$. The disagreement between the DNS and the Floquet results at Re $= 420$ may be attributed to at least two reasons, 1) the decay of DNS disturbances due to three dimensional dissipative effects, and/or 2) the neutral stability curves may be underpredicted due to the additional noise that is introduced at the beginning of the stability calculations by taking finite differences of Dirac delta functions at time $t = 0$, as discussed previously in the *Numerical procedures* section. However, the instabilities that develop into rolls and later bursts of turbulence in the DNS at Re $= 840$, C $= [1/4, 3/4, 5/4, 7/4]$, as discussed in the previous chapter, appear to be predicted by the neutral stability curves in Figures 3-11 and 3-12 because the source of the instability is the same: the advection of the laminar flow stratfication by a wall normal disturbance. However, the bursts of turbulence in the DNS at Re $= 840$ relaminarize, which suggests that three-dimensional dissipative effects produce global stability at Reynolds numbers at least as large as Re $= 840$.

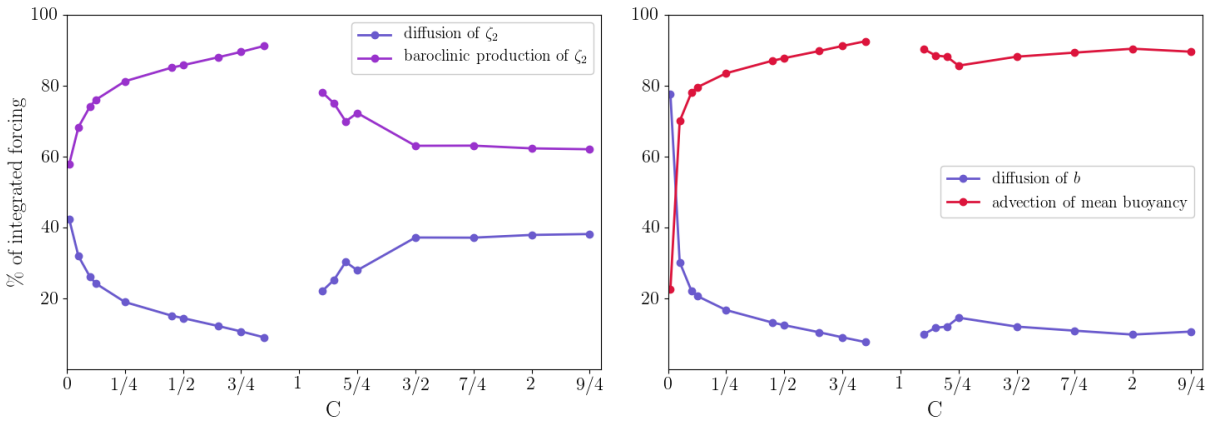

Figure 3-14: Integrated ζ_1, b, budgets for Re $= 420, l = 1.0$.
Percentages are calculated from the sum of all space and time integrated budget components for a given C (the sum of all terms at each C is 100).

3.5 Conclusions

In this chapter, Floquet global stability theory was applied to laminar, oscillating, stratified, viscous diffusive boundary layers on infinite slopes in non-rotating reference frames. Two disturbance scenarios were examined: a two-dimensional disturbance in the $x-z$ plane (described by the spanwise vorticity ζ_2) and a two-dimensional disturbance in the $y-z$ plane (described by the streamwise vorticity ζ_1). The former case was examined because it collapses to the Floquet stability problem for Stokes' second problem in the limit as $\mathrm{C} \to 0$, and the latter case was examined because experiments by Hart (1971) and the DNS results of the previous chapter suggest that the optimal disturbance mode for the boundary layers is on the $y-z$ plane.

Three separate instability mechanisms have been identified. For the $x-z$ plane (spanwise vorticity) calculations, as $\mathrm{C} \to 0$ the Floquet instabilities are primarily controlled by the advection of vorticity disturbances by the base flow and by the advection of base vorticity by the disturbances. The buoyancy disturbances may seed the growth of unstable vorticity disturbances but are otherwise unimportant, and the neutral stability curve resembles that of Stokes' second problem. As C increases the $x-z$ plane calculations suggest that growing instabilities are primarily associated with the interaction of the spanwise vorticity disturbances and the base flow velocity. For the $y-z$ plane (streamwise vorticity) calculations, the instabilities can only be attributed to the oscillating base flow stratification. Therefore the neutral stability curves reflect the changes in the amplitude of the base flow stratification with C and Re. Except for low wavenumber supercritical slopes, the $y-z$ plane calculations are generally unstable at lower Reynolds numbers than the $x-z$ plane calculations, which was expected from the previous DNS study in Chapter 1 and experiments Hart (1971). The $y-z$ plane equations and stability calculations imply that the instablity of gravitationally unstable Couette flow, which is unaffected by the shear, is the dominant instability mechanism for stratified, oscillating, viscous, diffusive boundary layer flows for all values of $\mathrm{C} = N \sin\theta/\omega$ investigated. The disturbance equations also indicate that the flow likely becomes more susceptible to the $y-z$ plane instability with increasing Prandtl number.

It was also confirmed that Floquet stability calculations for oscillating boundary layers are sensitive to transient numerical noise, in agreement with the conclusions of Luo and Wu (2010) for Stokes' second problem calculations. While the transient noise can represent actual physical processes, the statistical characteristics are not readily discernable, which makes the disturbance conditions of the numerical calculations impossible to replicate in laboratory experiments, which may include other sources of transient noise. It was shown that the transient noise cannot be eliminated by increasing the numerical accuracy, therefore the results of this study support the conclusion that numerical Floquet stability calculations must be considered approximate, rather than exact, estimates.

Chapter 4

Data-driven probabilistic finescale parameterization

4.1 Introduction

Three-dimensional, finescale turbulence is difficult to measure in the ocean (Thorpe (2007)). The notion of the "finescale" pertains to vertical motions of length scale $\mathcal{O}$(10-100 m), approximately the largest eddy scales of turbulence produced by an internal-wave-induced overturn. The most common direct turbulence measurements are made with microstructure profilers, which measure high frequency velocity and temperature fluctuations while sinking at terminal velocity. Raw profiler data is then processed to obtain dissipation rates of turbulent kinetic energy, ε, and dissipation rates of temperature variance, assuming that the measured turbulence is statistically homogeneous and isotropic.

Measurements of the dissipation rate are useful for at least two reasons: 1) closing the kinetic energy budget of the ocean; and 2) inferring diapycnal mixing. The mixing is inferred by using the Osborn (1980) model, which is a simple algebraic relationship between the dissipation rate and the rate of conversion of turbulent kinetic energy into potential energy (a.k.a. buoyancy flux), assuming that a) the turbulence is in steady state equilibrium, b) the turbulent transport is negligible, and c) that the flux Richardson number (the ratio of the conversion rate to potential energy to the production rate of turbulence by mean shear) is fixed at a value of approximately 1/6. Despite the seemingly restrictive assumptions

and a lack of a rigorous justification (Gregg et al. (2018)), the constant-coefficient Osborn (1980) model has prevailed as a tool for inferring diapycnal water mass transformation from observations.

4.1.1 Finescale parameterization

The importance of diapycnal water mass transformation to the global overturning circulation and the sparsity of in situ measurements of the dissipation rate relative to coarser resolution measurements of current velocity, shear, and standard hydrographic variables, such a temperature and salinity, has motivated the development and use of finescale parameterizations. The industry standard finescale parameterization was created cumlatively by several authors based on the premise that in the open ocean, the dissipation rate is spatio-temporally correlated with finescale shear and strain (isopycnal spreading) variances (Gregg (1989); Polzin et al. (1995)) as predicted by theories of wave-wave interaction cascade that ultimately leads to "breaking" and turbulence (McComas (1981); Henyey et al. (1986)), such that the internal wave energy cascade is proportional to the energy cascade of the turbulence (i.e. the dissipation rate) generated by the wave breaking. This standard parameterization will be referred to in this study as the Gregg-Henyey-Polzin (GHP) model. For a comprehensive discussion of the relevant physics, restrictions, and assumptions of the GHP model, the reader is referred to Polzin et al. (2014b). In addition Whalen et al. (2015) reviews the performance and limitations of the GHP model in practice, that is, as it relates to inferences of diapycnal mixing via observations. Gregg et al. (2003) added a correction to the standard for equatorial predictions, while St.Laurent and Garrett (2002) and Polzin (2009) developed separate dissipate rate models of internal tide breaking near internal tide generation sites that are used in ocean general circulation models in tandem with the Osborn (1980) model to estimate abyssal diapycnal mixing (Simmons et al. (2005); Melet et al. (2013)).

Thurnherr et al. (2015) develop different approach to finescale parameterization based solely on the vertical kinetic energy at finescale, p_0 (taken as 6 vertical resolution in Thurnherr et al. (2015)). Finding a mutually agreeable power law fit for ε in terms of p_0 between two data sets with separate ranges of ε, Thurnherr et al. (2015) proposed the simple finescale

parameterization

$$\varepsilon = \left(\frac{p_0 m_0^2}{c}\right)^2, \tag{4.1}$$

where $m_0 = 1$ rad m^{-1} is the finescale vertical wavenumber and the constant is determined by the power law fit to the data as $c \approx 0.0215$ s$^{-1/2}$. Notably, the model does not require corrections for latitude, shear-to-strain ratio, and buoyancy frequency that the GHP model requires nor does its validity rest upon assumptions about the local internal wave field. Thurnherr et al. (2015) argued that the single parameter model for ε is possible because they observed that the spectra of internal wave VKE has a spectral slope of m^{-2} across five dynamically and geographically disparate data sets examined (the same five data sets are used in this study). The Thurnherr et al. (2015) model, Equation 4.1, performed approximately as well as the GHP model for data set averaged dissipation rate estimation. It is tempting, but presently speculative, to explain the apparent single-parameter dependency of ε on the finescale VKE as indicative of the finescale VKE being the appropriate measure of the energy of the largest eddy in a turbulent event. The Ozmidov scale, or the approximate vertical scale of the largest eddies that can overturn in a stably stratified flow, is a parameter that could affect VKE at the finescale.

4.1.2 Dissipation range intermittency

Intermittency measured in the dissipation range, or at the spatio-temporal scales of Kolmogorov eddies, such as might be recorded by a microstructure profiler, is inherently intermittent. Even in homogeneous-density statistically stationary equilibrium turbulence, the flow at the dissipation scales is spatio-temporally intermittent (Batchelor and Townsend (1949)). Theoretical arguments by Frisch and Morf (1981) and Kraichnan (1967) articulated that intermittency in the dissipation range is consistent with Kolmogorov (1941) theory. Gurvich and Yaglom (1967) showed that, for statistically homogeneous and isotropic turbulence, the turbulence cascade leads to lognormal probability density functions (PDFs) of the dissipation rate (i.e. $\log_{10}\varepsilon$ is a normal distribution). Lognormal distributions are characteristic of positive definite variables created by the repeated multiplicative application of a random process to the positive definite variable (a.k.a. multiplicative noise). Multiplicative

noise is a classification of forcing terms in stochastic differential equations, in which the variable that is evolving in time is multiplied by a random sample of a distribution (e.g. Gaussian noise if the random sample is taken from a Gaussian distribution) at each time step. Gurvich and Yaglom (1967) also argued that the standard deviation of $\log_{10}\varepsilon$ is a measure of the intermittence of turbulent events, and therefore indicative of the difficulty of acquiring enough samples for accurate identification of the underlying PDF.

Turbulence generation mechanisms in the ocean are often strongly intermittent in amplitude, time, and space (Baker and Gibson (1987); Gibson (1998)). Oceanic internal waves oscillate over a spectrum of frequencies bounded by the buoyancy frequency N and the Coriolis parameter (inertial frequency) f, and thus typically have time scales on the order of hours. Away from sources of sustained turbulence, such as the surface boundary layers or regions where the internal wave activity is exceptionally intense, turbulence produced by the breaking of internal waves is a intermittent process in both time and space (Thorpe (2007)). Even in a region where the internal wave activity is both intense and sustained, a fracture zone on the western flank of the Mid-Atlantic Ridge in the South Atlantic Ocean, Toole (2007) found significant variability in dissipation rate on a range of time scales, including frequencies as low as fortnightly periods, attributed to a variety of shear production mechanisms. Gregg et al. (1993) observed lognormal distributions of the dissipation rate in observations of the North Pacific, while Pearson and Fox-Kemper (2018) found lognormal distributions of the dissipation rates in numerical simulations of the global ocean up to horizontal scales of 10 km.

4.1.3 A probabilistic representation of the dissipation rate

Finescale parameterizations of the dissipation rate and microstructure measurements of the dissipation are measurements of distinctly different quantities. The time and length scales of the finescale parameterizations are larger than that of microstructure measurements; therefore, finescale parameterization estimates can be thought of as the dissipation rate averaged over many wave periods (Whalen et al. (2015)). However, the mean of lognormal distribution is not equivalent to the mode, which is the value corresponding to the peak of the PDF and therefore the value that is most likely to be measured. The mean of a lognormal distribution

is larger than the mode. Therefore 1) an empirical finescale parameterization must account for the lognormal distribution or risk predicting a value greater than actually occurs most often in a data set, and 2) a finescale parameterization that accounts for the lognormal PDF characteristics of the dissipation rate could be used to include the effects of intermittent turbulence in time-dependent numerical simulations.

A mixture density model is a probabilistic tool for making statistical inferences about the properties of the sub-populations given only observations on the total population, without sub-population identity information (McLachlan and Basford (1988)). A mixture density network (MDN) is a mixture density model that is optimized by a neural network (Bishop (1994)). If properly trained, the MDN model can make statistical inferences about the properties of a single data set (a.k.a. sub-population) given only samples from the entire pool of data, without any explicit information regarding data set identity. Here the objective is to train the MDN model with observational data to predict the PDF of ε, $P(\varepsilon)$, for each data set, conditional upon the finescale VKE p_0, the square ratio of the buoyancy frequency to the inertial frequency $N^2 f^{-2}$, and both p_0 and $N^2 f^{-2}$. If the conditional PDF of ε is well described by the marginal PDFs of p_0 and/or $N^2 f^{-2}$, then the MDN will find the underlying conditional PDF of ε. Random samples drawn from the output PDF of ε can be regarded as instantaneous measurements of ε for the input p_0 and/or $N^2 f^{-2}$.

Multivariate regressions are often discussed as an alternative to employing a supervised representative machine learning algorithm. However, a multivariate fit of the data implicitly requires assumptions regarding the presence of Gaussian noise in the data, and in this case a model is sought that makes no assumptions about the PDF of the target variable.

4.2 Data

The processed data of Thurnherr et al. (2015) are used in this study. The physics and salient technical details of each of the five data sets (from four different cruises) are discussed in this section; the reader is referred to Thurnherr et al. (2015) for a complete discussion of the acquisition and processing of the raw data.

All of the data sets of Thurnherr et al. (2015) contain estimates of internal vertical

kinetic energy (VKE) from lowered acoustic Doppler current profilers (LADCPs), estimates of the buoyancy frequency from conductivity- temperature-depth (CTD) measurements, and estimates of the homogeneous, isotropic dissipation rate of turbulent kinetic energy from microstructure shear measurements by various microstructure profilers. The entire data set includes upwards of 250 profiles, each separated by at minimum several hundred meters in the horizontal and taken at minimum 20-30 minutes apart, in a depth range of $-3830 < z < -150$ m. Thurnherr et al. (2015) calculated between 125 and 517 averaged spectral windows of vertical wavenumber m to obtain the VKE spectral density as a function of vertical wavenumber, $p(m)$, and crucially found that a $p \propto m^{-2}$ across all five data sets. Thurnherr et al. (2015) then estimated the spectral power of the VKE at the "finescale level," corresponding to a vertical wavelengths of $\lambda_0 = 2\pi$ m (where $m_0 = 2\pi/\lambda_0 = 1$ rad m^{-1}) by fitting to the apparent power law, denoted as $p_0 = p(m_0)$. The buoyancy frequency and dissipation rate of kinetic energy corresponding to each internal wave VKE spectral density were calculated using conventional methods discussed in Thurnherr et al. (2015).

Each data set contains information about a different internal wave field subjected to different environmental conditions. Internal waves are generated by disturbances to the background stratification. The background stratification in the off-equatorial data sets is $\mathcal{O}(10^{-3})$ rad s^{-1}, and the equatorial thermocline data set features slightly stronger stratification on the cusp of $\mathcal{O}(10^{-2})$ rad s^{-1}. The influence of the local bathymetry is also present in the data sets; it dominates the patterns of internal wave generation and breaking in the Luzon Strait data set (Alford et al. (2011)), and it interacts with deep-reaching geostrophic flows associated with the Antarctic Circumpolar Current to form turbulent lee waves in the Drake Passage data set (St. Laurent et al. (2012)).

The "latitude effect" on internal waves is a downscale net energy flux arising from Doppler shifting, which depends on the dominant frequency. Since the dominant frequency of internal waves tends to be slightly greater than inertial frequency f, increasing latitude corresponds to increasing Doppler shift in the internal wave field (Henyey et al. (1986); Gregg et al. (2003)). Indeed, Thurnherr et al. (2015) found that the ratio of VKE spectral density to ε is suppressed in the *Equatorial thermocline* data set (MIXET project) relative to the other, off-equatorial data sets. The *East Pacific Rise* (LADDER-3 cruise) and *Luzon Strait* (IWISE

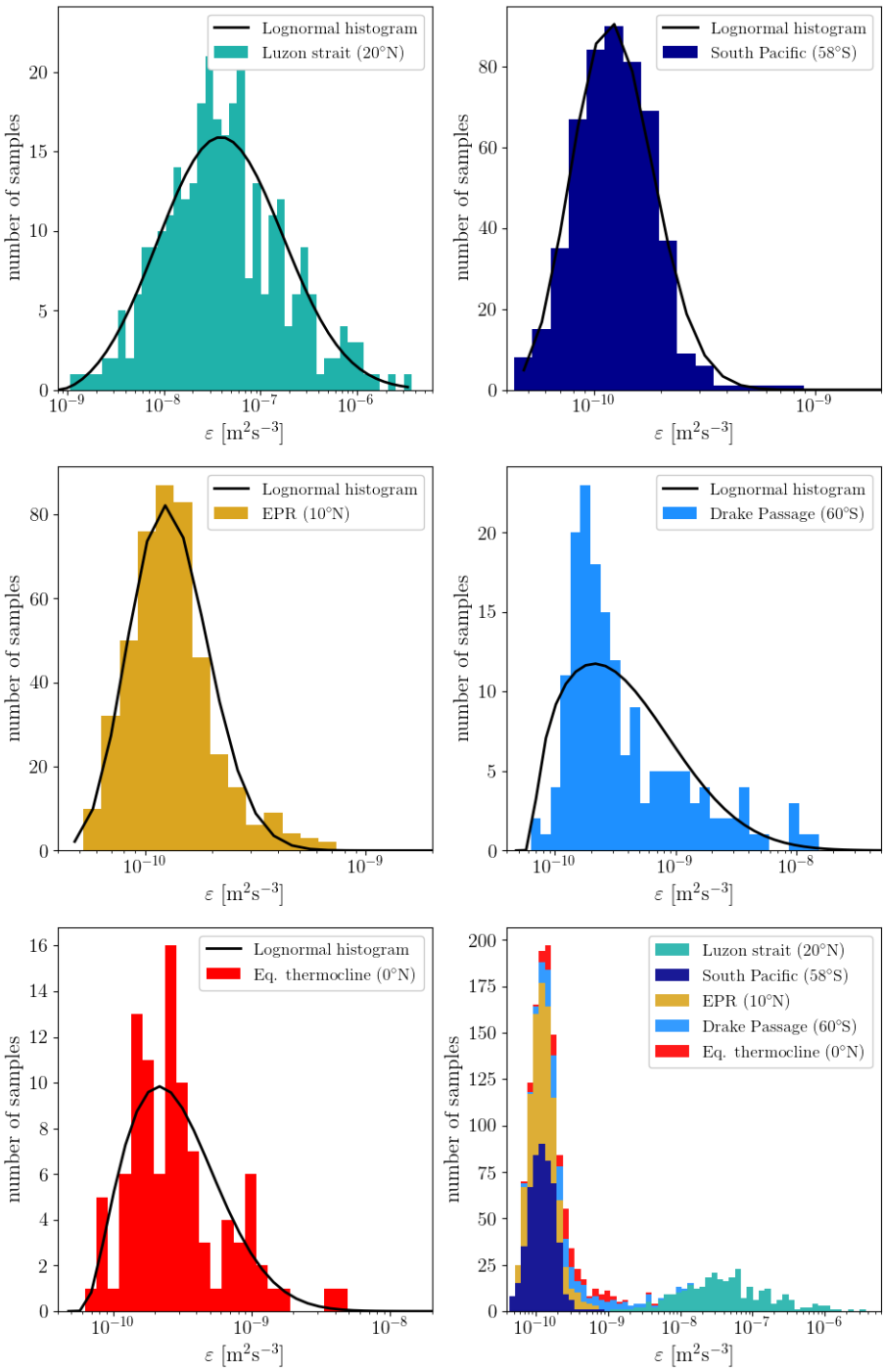

Figure 4-1: PDFs of ϵ for each data set.
The Drake Passage and equatorial thermocline data sets possess significant righthand side tails, while the Luzon Strait data set has the most variance.

project) data sets are tropical (9.7 ± 0.2°N and 20.2 ± 0.2°N, respectively) while the *South Pacific* and *Drake Passage* data sets (both from the DIMES US2 cruise) are high latitude ($58.9 \pm 2.$°N and 59.7 ± 1.4°N, respectively).

Data set	N_{samples}	μ_ε [m^{2}s^{-3}]	σ_ε [m^{2}s^{-3}]	$S_\varepsilon \pm SE_{S,\varepsilon}$	$T_{S,\varepsilon}$	$F_\varepsilon \pm SE_{F,\varepsilon}$	$T_{F,\varepsilon}$
Luzon Strait (20°N)	305	$1.2 \cdot 10^{-7}$	$3.3 \cdot 10^{-7}$	6.69 ± 0.14	840	59.65 ± 0.28	220
South Pacific (58°S)	506	$1.3 \cdot 10^{-10}$	$6.1 \cdot 10^{-11}$	3.46 ± 0.11	720	23.48 ± 0.22	110
East Pacific Rise (10°N)	446	$1.4 \cdot 10^{-10}$	$6.3 \cdot 10^{-11}$	2.93 ± 0.12	540	11.37 ± 0.23	50
Drake Passage (60°S)	168	$7.6 \cdot 10^{-10}$	$1.7 \cdot 10^{-9}$	4.27 ± 0.18	300	19.64 ± 0.37	50
Equatorial thermocline	99	$3.9 \cdot 10^{-10}$	$4.4 \cdot 10^{-10}$	4.45 ± 0.24	180	22.96 ± 0.48	50

Table 4.1: Data set population statistics.

The properties of the PDF of ε for each data set are shown in Table 4.1. All of the properties are consistent with lognormal distributions: positive skewness and excess kurtosis. σ_ε is the standard deviation of the dissipation rate of turbulent kinetic energy. S_ε is the moment coefficient of skewness (a.k.a. skewness) of ε, and $SE_{S,\varepsilon}$ is the standard error of skewness for the finite population of ε. $T_{S,\varepsilon}$ is the test statistic (Cramer (2002)) for the skewness of ϵ: It is an estimate of the skewness of the true population, not the skewness of the finite subsample, S_ε. Since all of the data sets in Table 4.1 $T_{S,\varepsilon} \gg 2$, the true populations of ε for each data set are very likely skewed positive. Similarly, F_ε is the moment coefficient of excess kurtosis (a.k.a. flatness) and $SE_{F,\varepsilon}$ is its standard error. The flatness test statistics for all of the data sets is $T_{F,\varepsilon} > 2$, which indicates that the true populations have longer, fatter tails than a Gaussian distribution and higher and sharper central peaks than a Gaussian distribution. The enhanced flatness and pronounced positive skewness of the ε distribution in all of the data sets is the signature of processes that create anomalously large ε intermittently in space and time: the turbulence occurs in patchy bursts in all of the data sets.

4.3 Supervised learning method

In supervised learning, the model learns the input-to-output relationship after being provided both the inputs (feature vector/tensor) and the respective outputs (labels). Bishop (1994) combined the concept of mixture density models (McLachlan and Basford (1988)) with conventional neural networks to create Mixture Density Networks (MDNs) for supervised representation learning. MDNs can represent arbitrary conditional probability distributions (including multi-modal) in the same way that conventional neural networks can represent arbitrary functions. The ability to represent arbitrary conditional probability distributions is particularly advantageous when the task is to predict mean trends in data with significant non-Gaussian features, such as the thick positive tails of the distributions ε data sets in Table 4.1. In the present study, the MDN output *is a distribution of* ε: There are no imposed assumptions regarding distribution of ε, as are implicitly assumed in nonlinear or linear statistical regressions.

4.3.1 Mixture density networks

A mixture density model is in essence a modal decomposition of a conditional PDF into the sum of weighted conditional PDFs of subpopulations:

$$P(\mathbf{y}|\mathbf{x}) = \sum_{i=1}^{n} \alpha_i(\mathbf{x})\phi_i(\mathbf{y}|\mathbf{x}), \tag{4.2}$$

where $P(\mathbf{y}|\mathbf{x})$ is the PDF of $\mathbf{y}$ conditional upon $\mathbf{x}$, that is $P(\mathbf{y}|\mathbf{x})$ is the probability density of $\mathbf{y}$ given that $\mathbf{x}$ is a particular value. n is the number of "mixtures." Each subpopulation, denoted by subscript i, is the product of the weights α_i and the conditional PDFs $\phi_i(\mathbf{y}|\mathbf{x})$. In this study, $\mathbf{y} = \varepsilon$ and $\mathbf{x} = (p_0, N, f)$. The form of the weighted subpopulation PDFs must be chosen. Here they are chosen to take the form of Gaussian distributions:

$$\phi_i(\mathbf{y}|\mathbf{x}) = \frac{1}{\sqrt{2\pi\sigma_i(\mathbf{x})^2}} \exp\Big[- \frac{(\mathbf{y} - \mu_i(\mathbf{x})}{2\sigma_i(\mathbf{x})^2} \Big] \tag{4.3}$$

where σ_i is the standard deviation and μ_i the mean for the ith subpopulation. A forward pass through the network is shown in the schematic of Bishop (1994) shown in Figure 4-2; the input is passed through a neural network to obtain the parameter vector for the weights of a mixture model, at which point the output PDF is constructed.

The heart of the MDN model is the loss function. It optimizes the neural network model to maximize the statistical likelihood that the predicted variable falls within a probability density function conditional on the input. The MDN model is a conventional neural network with appropriate dimensions for the input of feature vector $\mathbf{x}$ and an output vector of length $3n$, corresponding to the number of subpopulations multiplied by the number of characteristic variables of each subpopulation. In this case, the characteristic variables for each subpopulation are $\alpha_i, \mu_i, \sigma_i$. After one forward pass through the network, the output characteristic variables are then normalized appropriately (i.e. $\sum_{i=1}^{n} \alpha_i = 1$), and the PDF of the mixture model is compared with the labels by estimating the statistical likelihood that the output mixture model PDF gave rise to a particular set of training data labels,

$$\mathcal{L} = \prod_{j=1}^{q} P(\mathbf{y}_j|\mathbf{x}_j), \tag{4.4}$$

where q is the number of training examples, $\mathbf{y}_j$ is the jth training data label, and $\mathbf{x}_j$ is the jth training data feature vector. If $\mathcal{L} \gg 1$ then the training data labels fall within the output PDF that is conditional on the training feature vector. In practice it is convenient to define an error or "loss" function that is minimized during training, so

$$\text{loss} = -\log(\mathcal{L}), \tag{4.5}$$

is minimized as through each successive pass of the training data by optimizing the weights in the conventional neural network that outputs the characteristics of the mixture density model. The network was implemented in Tensorflow (Abadi et al. (2016)) using the Adam optimizer algorithm (Kingma and Ba (2014)).

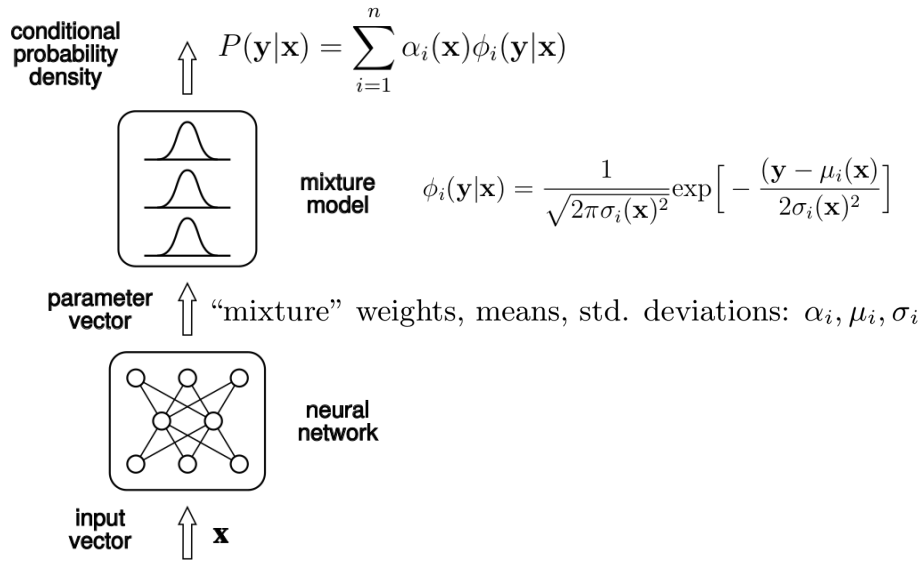

Figure 4-2: Schematic of a forward pass through an MDN, modified from Bishop (1994).

4.3.2 Model training

The limited size of the data set (∼1524 samples) posed two challenges for training the MDN. The first challenge was that the test data (data that the model was applied to separate from the training data) needed to be as large as possible in order to feed the model a representative sample of the distributions of the feature vector, $\mathbf{x} = (p_0, f, N)$, and label variables, ε. Therefore the ratio of training data to testing data was unity (a 50/50 split). The training data was randomly and evenly subsampled from all five data sets.

The second challenge (another symptom of "small" data), was that was the predictions of the PDF of ε varied slightly from model run to model run, because the data set was insufficiently large for a random subsample of half of it to be truly representative of its entirety. To circumvent this problem, the MDN results presented below are the outcomes of many repeated training/testing sessions ("model runs"); effectively, the learning was bootstrapped. This was acheived in three steps by

1. obtaining the trained PDFs $P(\varepsilon)$ (i.e. the weights, means, variances of the training mixture models) of many separate model runs;

2. generating many random samples of the trained $P(\varepsilon)$ for each model,

3. combining all of the random samples from all of the model run PDFs into a pool of data;

4. randomly subsampling the combined pool of data to obtain a final distribution.

With a larger data set, the training-by-bootstrapping would be unnecessary. The bootstrapped results converged for 10-20 model runs. The training-by-bootstrapping method outlined above is equivalent to training on all of the data, because the resulting PDF is generated by a combination of models that together have trained on all of the data. However, with enough data, the bootstrapping techinique will not be required to obtain the same PDF from every training run. Furthermore, the goal of this study is to construct a PDF fit, which is acheived by training on all of the data.

The number of hidden layers was varied from one to four, with little discernable improvement in predictive skill for more layers; only one hidden layer was used to generate the results below. Each variable was normalized by calculating its Z-score (subtracting the mean and dividing by the standard deviation), and the standard sigmoid activation function was applied to the hidden layer of neurons. Through trial and error, neuron dropout was found to be unnecessary because the MDN generates a continuous distribution for each input rather than a single output and therefore MDNs are less likely to overfit the data. The number of neurons per layer was set to 100, and the number of mixtures was set at 18. Adding more mixtures and /or neurons led to no appreciable difference on data set mean values. The neural network weights were initialized with Gaussian random noise centered at 0 with a standard deviation of 0.25, and the learning rate was set to 10^{-4} over a maximum of 120,000 epochs.

Three conditional PDF models were trained: $P(\varepsilon \,|\, p_0)$, $P(\varepsilon \,|\, N^2 f^{-2})$, and $P(\varepsilon \,|\, p_0, N^2 f^{-2})$. The conditional PDF $P(\varepsilon \,|\, p_0, N^2 f^{-2})$ was trained with $f^2 N^{-2}$ to avoid singularities. Mean values for a single model run of $P(\varepsilon \,|\, p_0, N^2 f^{-2})$ are shown in Figure 4-3 (recall that for every input $N^2 f^{-2}$ the model output is a PDF).

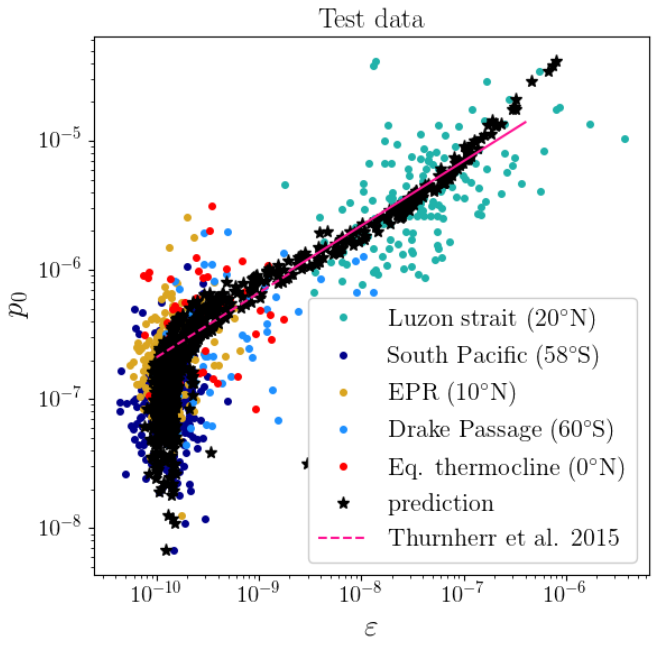

Figure 4-3: Mean values for a typical model run of $P(\varepsilon \,|\, p_0, N^2 f^{-2})$.

4.4 Results & Discussion

Figure 4-4 shows the stacked histograms of the original data set (top left) and the test data results (predictions for the half of the data set that the model was not trained on) for the three different conditional ε PDFs, color-coded by data set. The total mode of all three modeled conditional PDFs plotted in Figure 4-4 match the total mode of the total observed distribution exactly within the histogram bin corresponding to mode$[\varepsilon] = 1.4 \cdot 10^{-10} \pm 2.1 \cdot 10^{-11}$ m^{2}s^{-3}. All three modeled conditional PDFs reproduced the bimodal characater of the observation histogram, and all three modeled conditional PDFs capture the enhanced variance of the Luzon Strait data set. The $P(\varepsilon|p_0)$ and $P(\varepsilon \,|\, p_0, N^2 f^{-2})$ distributions contain a similar error: both predict a mode of Luzon Strait data around $\varepsilon = 2 \cdot 10^{-10}$ m^{2}s^{-3}. This error may be attributed to the fact that the $P(\varepsilon \,|\, p_0)$ and $P(\varepsilon \,|\, p_0, N^2 f^{-2})$ models approximately identified the power law of Thurnherr et al. (2015) and combined that information with the center of mass at $\varepsilon = 1.4 \cdot 10^{-10}$ m^{2}s^{-3} to produce the low mode in Luzon Strait data that does not match the data set. The model without the finescale VKE, $P(\varepsilon|N^2 f^{-2})$, fairs better in the lowest decade, presumably because that model did not find the power law signal.

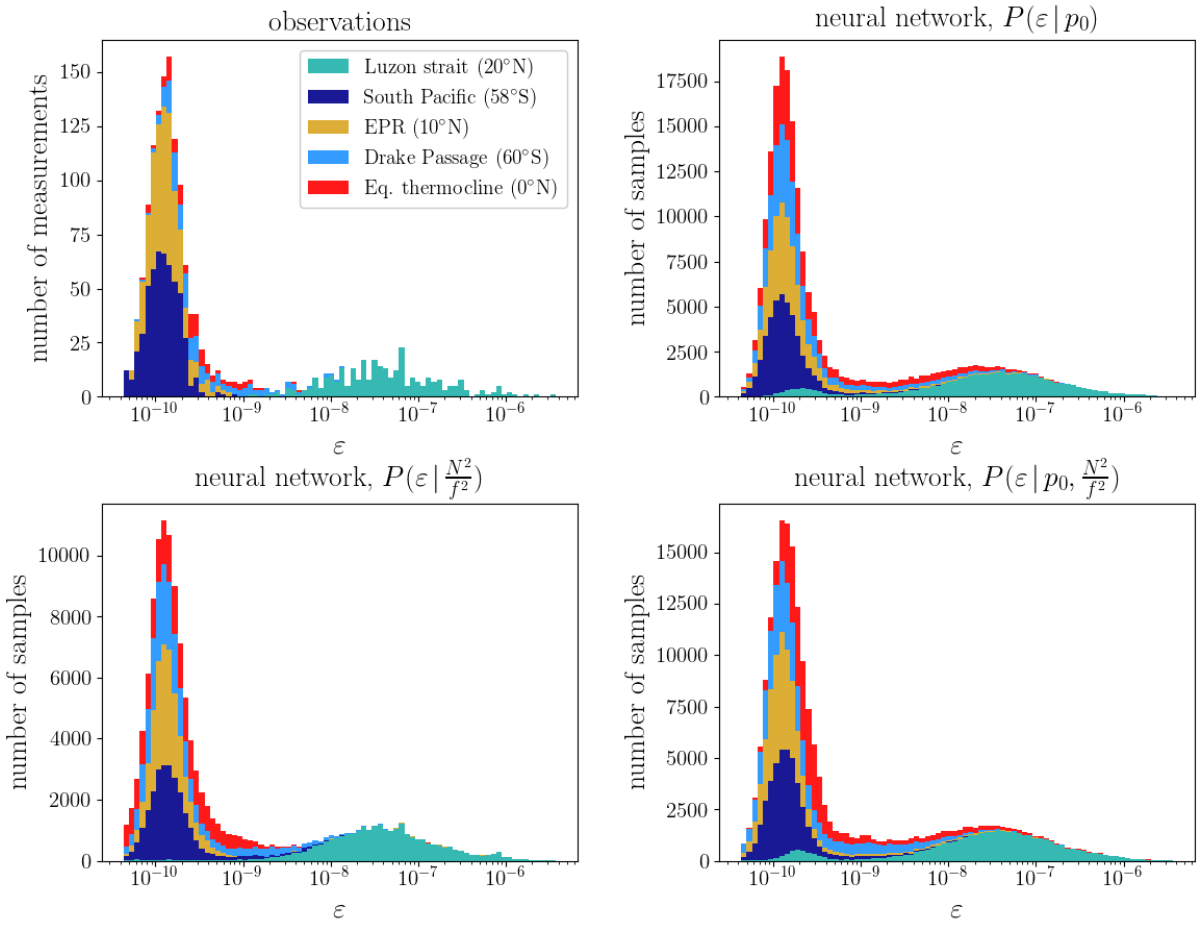

Figure 4-4: Stacked histograms of the observations and MDN results. Note that the VKE conditional models, $P(\varepsilon\,|\,p_0)$ and $P(\varepsilon\,|\,p_0, N^2 f^{-2})$, do not separate the data sets as well as the $P(\varepsilon\,|\,N^2 f^{-2})$ model. The VKE models predict a fictitious low mode of Luzon strait data and tails of the other data set distributions that extend higher ε values than are exist in the observed data. The fictitious tails produced by the VKE models indicate that the PDF fit is more difficult if the algorithm is not trained with environmental parameters ($N^2 f^{-2}$) and that a different normalization scheme for $N^2 f^{-2}$ relative to p_0 may be required for the $P(\varepsilon|p_0, N^2 f^{-2})$, because the $P(\varepsilon\,|\,N^2 f^{-2})$ model separates the data sets to a much better degree.

The power law of Thurnherr et al. (2015) (Equation 4.1) is compared to the model fits in Figure 4-5. The 95% confidence intervals from bootstrapping by bins of $\log_{10}\varepsilon = 0.5$ are shown as error bars. The $P(\varepsilon\,|\,p_0)$ and $P(\varepsilon\,|\,p_0, N^2 f^{-2})$ models approximate the (mean) power law, but taper upwards in the uppermost decade, where the training data was quite sparse. Notably, the $P(\varepsilon\,|\,N^2 f^{-2})$ model produces two bins of ε, near the lowest values of the Luzon Strait data set, in the vicinity of the power law. This can be interpreted as a

correlation between the of N^2/f^2 and p_0 in the lower range of $P(\varepsilon)$ in the Luzon Strait data set. Given the low latitude, the fact that the model was trained upon f^2N^{-2}, and the vigorous amount of local internal tide generation in the Luzon Strait data set (Alford et al. (2011)), one can speculate that the correlation identified in the training of the $P(\varepsilon \,|\, N^2 f^{-2})$ model is between the VKE and weak stratification near the bottom (where $f^2N^{-2} \gg 1$).

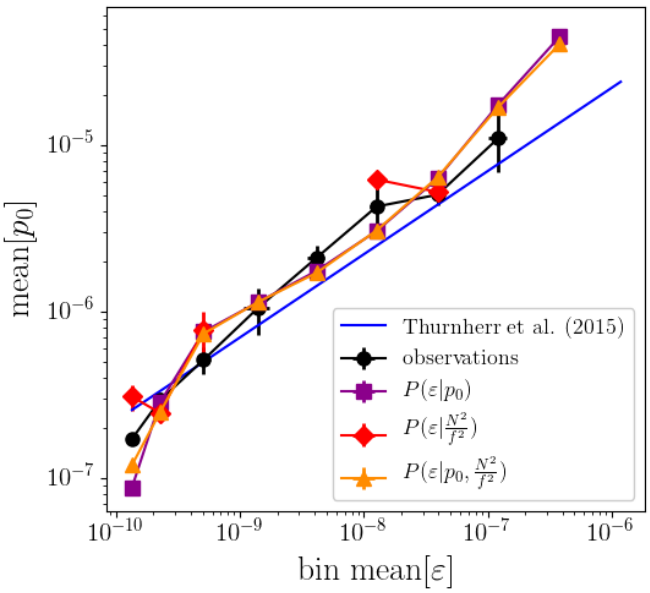

Figure 4-5: The VKE power law fit.

The accuracy of the data set means and data set modes (most likely) of each distribution is shown in Figure 4-6. The 95% confidence interval from bootstrapping is shown for the observed data (x-axes) as error bars. The black line represents exact accuracy, the dark shaded gray bars represent a factor of two accuracy, and the successively lighter shaded bars are factors of four and eight.

The spread of the means of VKE-conditional models, $P(\varepsilon \,|\, p_0)$ and $P(\varepsilon \,|\, p_0, N^2 f^{-2})$, closely resembles that of the power law fit parameterization of Thurnherr et al. (2015), although the Luzon Strait data set accuracy resides almost exactly at an accuracy of a factor of two for the $P(\varepsilon \,|\, p_0, N^2 f^{-2})$ model. The equatorial thermocline data is overpredicted by a factor of four for both VKE-conditional models because the dissipation rate is suppressed relative to the VKE within 1° degree of the equator (Gregg et al. (2003); Thurnherr et al. (2015)). Given the lack of information regarding the shear to strain ratio and

the Garrett-Munk spectrum, the $P(\varepsilon \,|\, N^2 f^{-2})$ performed surprisingly well at predicting the data set means of the Equatorial thermocline and Drake Passage data sets. However, data set means are not an ideal measure of model accuracy because data set or bin integrated quantities will remove errors that are symmetric within the integral quantity. The modes (the right hand column in Figure 4-6) for all three models are quite accurate; curiously, the $P(\varepsilon \,|\, N^2 f^{-2})$ fairs the best in the Luzon Strait data set.

The least accurate MDN predictions for the data set mean are the Luzon Strait and the Drake Passage data sets. The small sample size of the Drake Passage data set means that the prediction error is likely due to insufficient data. The $P(\varepsilon \,|\, p_0, N^2 f^{-2})$ prediction for the Luzon Strait outperforms predictions by conventional finescale parameterizations (Henyey et al. (1986),Polzin et al. (1995),Gregg et al. (2003)) and the p_0 power law finescale parameterization of Thurnherr et al. (2015) while the $P(\varepsilon \,|\, p_0)$ prediction fairs as well as the p_0 power law model of Thurnherr et al. (2015). The error of $P(\varepsilon \,|\, p_0, N^2 f^{-2})$ prediction for the Luzon Strait data set, which occupies almost the entire range of dissipation rate values within $-8 < \log_{10} \varepsilon < -6$, may be due to insufficient sampling at the upper end of ε magnitudes.

Model test: the Orkney Passage

The model was tested on a separate data set from the Orkney Passage, where Deep and Bottom Waters exit the Weddell Sea. A control volume budget indicates that, in the process of exiting the Weddell Sea, significant water mass transformation occurs in the Orkney Passage (Heywood et al. (2002)). The transformation is thought to occur within intense turbulence driven by large overturning events in tidal boundary layer processes (Polzin et al. (2014a)). Figure 4-7 shows the performance of the three conditional PDF models on the Orkney Passage data set, which is quite different from the training data for the models, shown in the upper left plot of Figure 4-4. Both of the VKE models, $P(\varepsilon \,|\, p_0)$ and $P(\varepsilon \,|\, p_0, N^2 f^{-2})$, force the mode toward the low end of the distribution (around 10^{-10} $\mathrm{m^2 s^{-3}}$) but fail to capture the true mode at roughly $3.5 \cdot 10^{-11}$ $\mathrm{m^2 s^{-3}}$, which is outside of the range of the training data. However, both VKE models produce a significant tail similar to tail of the observed ε extending up to 10^{-7} $\mathrm{m^2 s^{-3}}$. The $P(\varepsilon | N^2 f^{-2})$ performs poorly and misses both

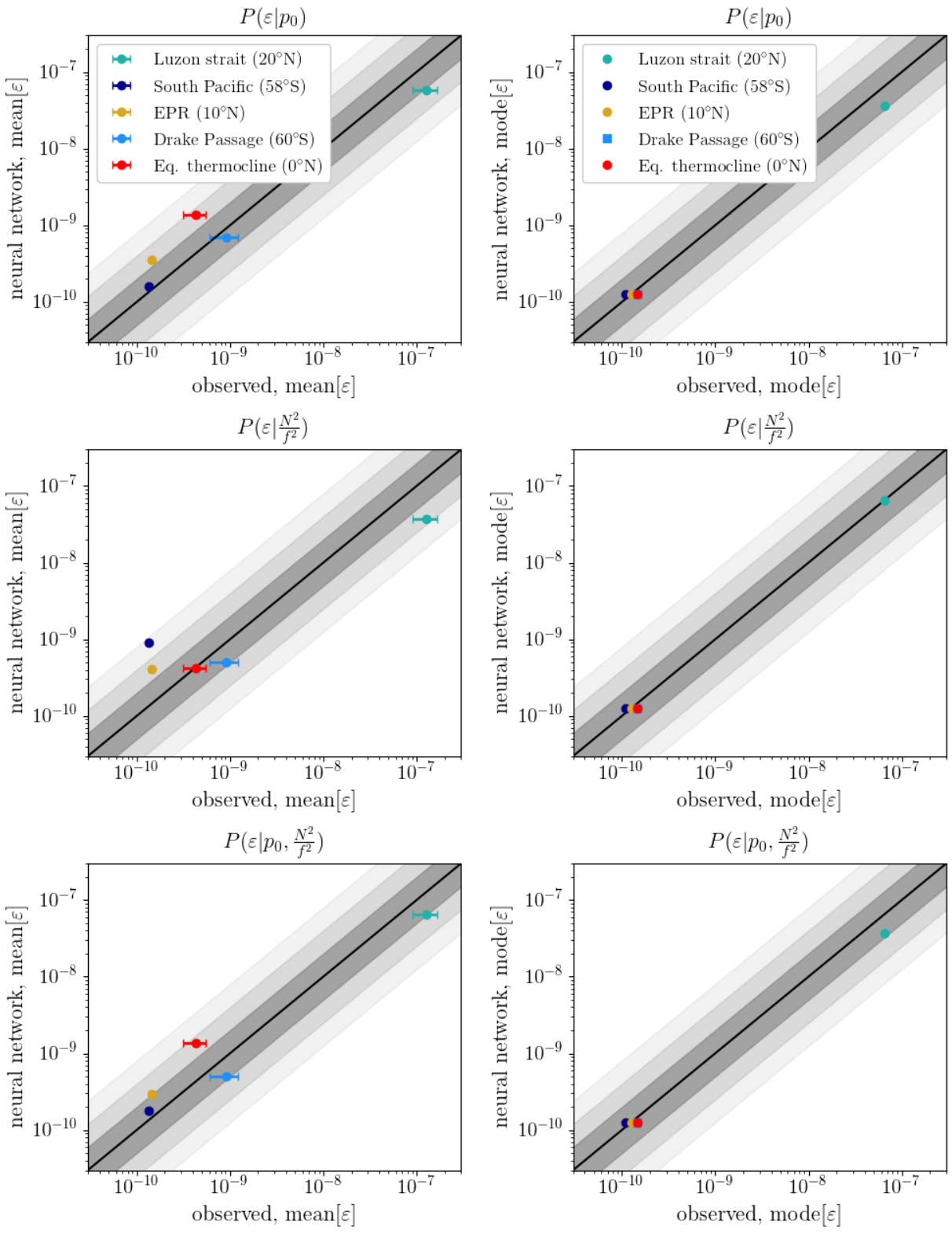

Figure 4-6: Mean and mode accuracy for each data set.

the extent of the right side tail and the mode, while the $P(\varepsilon \,|\, p_0, N^2 f^{-2})$ arguably performs the best.

The mode of the $P(\varepsilon \,|\, p_0, N^2 f^{-2})$ model is the closest to the observations (though still off by an order of magnitude) and the $P(\varepsilon \,|\, p_0, N^2 f^{-2})$ model generates a few values of ε on the order of 10^{-11}. The Orkney Passage data set mean is $1.7 \cdot 10^{-9}$ $\mathrm{m^2 s^{-3}}$, and the predictions of the mean by the $P(\varepsilon \,|\, p_0)$, $P(\varepsilon \,|\, N^2 f^{-2})$, and $P(\varepsilon \,|\, p_0, N^2 f^{-2})$ modles are $2.7 \cdot 10^{-9}$ $\mathrm{m^2 s^{-3}}$, $1.1 \cdot 10^{-9}$ $\mathrm{m^2 s^{-3}}$, and $5.9 \cdot 10^{-10}$ $\mathrm{m^2 s^{-3}}$, respectively. Therefore the $P(\varepsilon \,|\, p_0)$, $P(\varepsilon \,|\, N^2 f^{-2})$ models predict the mean within a factor of 2, and the $P(\varepsilon \,|\, p_0, N^2 f^{-2})$ model predicts the mean within a factor 3. The fact that the means are predicted reasonably well while the distribution modes shown in Figure 4-7 err by an order of magnitude underscores the problem with evaluating the accuracy of a prediction a data set mean values. However, the $P(\varepsilon \,|\, p_0, N^2 f^{-2})$ model represents the data better than the single conditional variable models, which suggests that if an appropriate third or fourth conditional variables can be obtained and used for model training it may still be possible to generate a universal $P(\varepsilon)$ prediction tool.

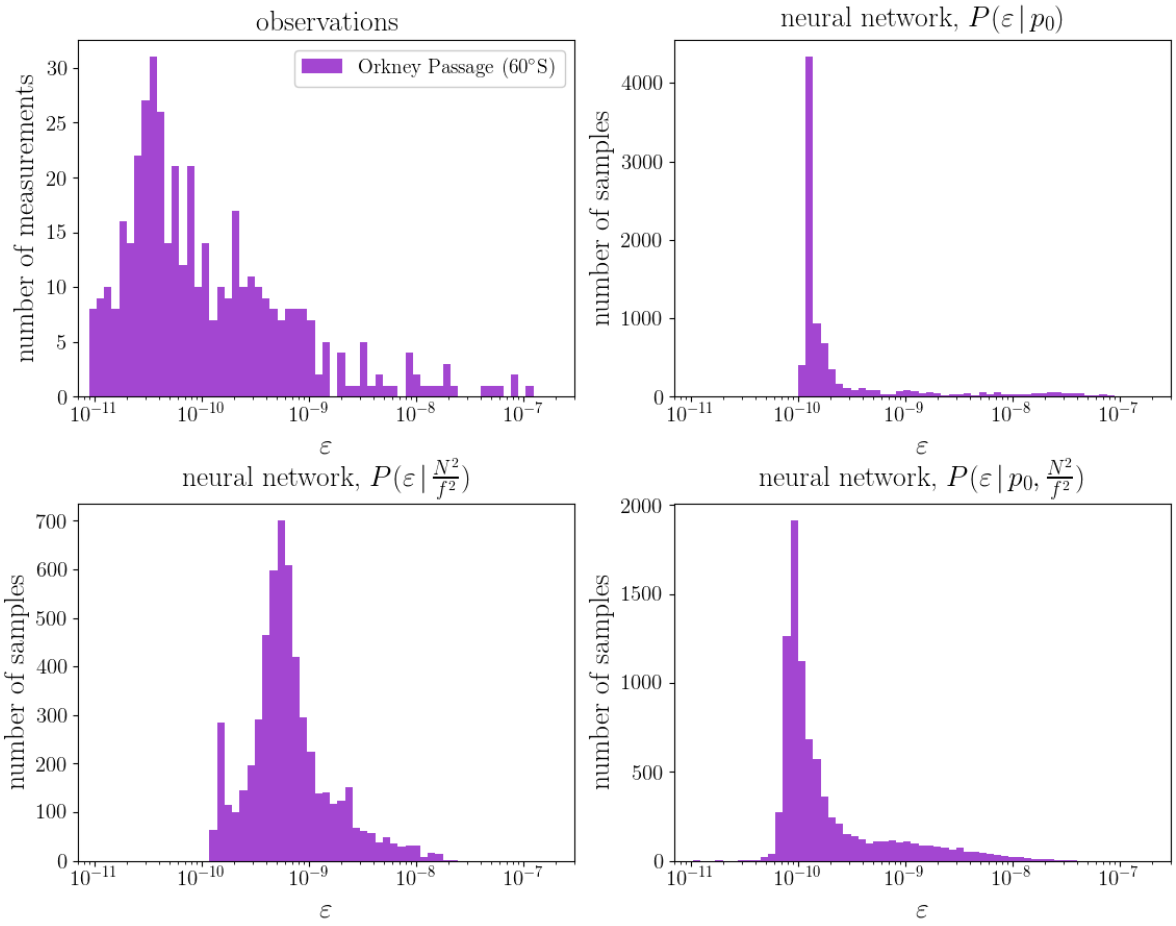

Figure 4-7: Stacked histograms of the observations and MDN results. The $P(\varepsilon\,|\,N^2 f^{-2})$ model generates a few ε values of $\mathcal{O}(10^{-11})$ $\mathrm{m^2 s^{-3}}$, while the single conditional variable models do not. This suggests that the addition of more carefully chosen variables may enable the construction of a universal $P(\varepsilon)$ prediction tool.

4.5 Conclusions

In this chapter, five separate data sets were used to train a neural network prediction of a conditional PDF of the dissipation rate of turbulent kinetic energy, and a separate data set was used to test the neural network prediction. Three separate conditional PDF models were constructed: one conditional on VKE at the finescale, one conditional on N^2/f^2, and one conditional upon both VKE and on N^2/f^2. The models with VKE "found" the VKE-ε power law of Thurnherr et al. (2015). All three models predicted the training data modes, or most likely value in the unimodal distributions to occur, with a factor of 2 for all of the training data sets, and the VKE conditional models predicted the training data mean

ε approximately as well as the VKE-ε power law of Thurnherr et al. (2015), though the prediction of the mean was slightly better for the case of the $P(\varepsilon \,|\, p_0, N^2 f^{-2})$ model. The $P(\varepsilon \,|\, p_0, N^2 f^{-2})$ model also outperformed the mean predictions by conventional shear- and strain-variance based data sets (Henyey et al. (1986), Polzin et al. (1995), Gregg et al. (2003)) for the training data. However, the mean predictions of test data from the Orkney passage imply that data set mean predictions may not be the best error metric because an infinite number of non-Gaussian PDFs, with centers of mass potentially far from the mean and with varying tail thicknesses, may have the same mean value.

Information regarding the temporal variability of ε is inherent to the training data, which is effectively composed of many roughly instantaneous snapshots of turbulent events, some steady and others intermittent. The empirical, probabilistic finescale parameterizations developed in this chapter account for both the intermittency of turbulence production events and the inherent intermittency at the dissipation scale. The statistical signature of intermittency is captured by the approximately lognormal conditional PDFs. The PDF models could be used as a time-dependent model of the dissipation rate as a function of VKE at the finescale and/or N^2/f^2, and be implemented in a ocean circulation model as a distribution of ϵ for grid cell or collection of grid cells.

The Luzon Strait, Drake Passage, South Pacific, East Pacific Rise, and equatorial thermocline data sets are insufficiently large enough train the PDF model with testing data left over. However, a test of the models was performed on the Orkney Passage data set. The results of that test indicated that the model is not a universal prediction tool, but also suggest that the addition of more variables (and of course, more data), it might be possible to develop a global ocean prediction tool for the PDF of ε. By construction, the model developed in the chapter can be easily modified and retrained to include bottom roughness or other dynamically relevant, co-located variables.

Chapter 5

Conclusions

A detailed understanding of the intensity, mechanisms, and three-dimensional spatial distribution of diabatic abyssal turbulence is germane to understanding the dynamics of the abyssal branch the global overturning circulation and ultimately to understanding climate variability on centennial to multi-millennial time scales (Sarmiento and Toggweiler (1984); Ferrari et al. (2014)). While a global portrait of the spatial distribution of diabatic turbulence is emerging (Kunze et al. (2006); Whalen et al. (2012); Waterhouse et al. (2014); Whalen et al. (2015)), the dynamics remain understood only in a qualitative sense (Cessi (2019)). While there are many sources of turbulence in the abyssal ocean, the breaking of internal waves near rough topography appears to be the dominant production mechanism of turbulent kinetic energy. Less is known about the boundary layers on the sloping seafloor than is known about the internal wave field above it. In this thesis, the boundary layers on sloping seafloors have been investigated using direct numerical simulations (DNS) and Floquet stability analysis, and a probabilistic ocean turbulence model has been constructed.

5.1 Comparison of the DNS and Floquet analysis studies

The DNS and Floquet stability analysis chapters of this thesis are an investigation of oscillating, stratified, viscous, and diffusive flow driven by across-isobath tidal forcing on extra-critical abyssal slopes. The problem is a variation of Stokes' second problem, with the addition of Boussinesq stratification and a tilted gravity vector. The DNS results indicate

that the laminar flow is more unstable at low slope Burger numbers because in that regime planetary vorticity induces shear that persists throughout the tidal period while across- and along-isobath disturbances to the shear are less suppressed by the stratification than they would be at slope Burger numbers greater than unity. The low slope Burger number case at Re = 840 was fully turbulent, meaning that turbulence persisted throughout the tidal period, although the turbulence was suppressed slighly during the downslope flow phase, during which the bulk boundary layer stratification increases.

For all of the other cases investigated (slope Burger number of order one in the rotating reference frame cases and infinity in the non-rotating reference frame cases), gravitational instabilities triggered ejections of low momentum fluid upward that induced bypass transition and subsequently bursts of turbulence. Indeed, in additional DNS runs with the $w\partial_z b$ term (which appears as $w\partial_z B$ in the Floquet analysis equations) removed from the governing equations turbulent bursts did not occur. Despite the critical role of buoyancy in triggering the bursts, the turbulence is primarily fed by energy extracted from the mean shear. The burst during the upslope part of the flow is the opposite of the behavior observed by Gayen and Sarkar (2011b), were gravitational instabilities were observed as the flow reversed from downslope to upslope in a DNS of a critical internal tide beam. The difference can be attributed to the tucking of light water under denser water by the critical internal wave beam during the downslope part of the phase. In the simulations in Chapter 2, the internal wave beam is not as tight as it would be at critical slope (Balmforth et al. (2002)); therefore, the bursts of turbulent kinetic energy production arise from less dramatic gravitationally instabilities. Since the turbulence can extract energy from the mean shear most readily when it is decelerating (Gad-El-Hak et al. (1984)) and when the stratification is weak or negative, the shear production driven burst preferentially occurs as the upslope flow is decelerating.

After the bursts occur during the upslope flow portion of the phase they relaminarize as the across-isobath velocity changes sign and begins to accelerate downslope. The most unstable Floquet modes generally corresponded to the vorticity component associated with the gravitational instabilities found in the DNS. However, inherent three-dimensionality of the turbulent bursts and the subsequent relaminarization found in the DNS results are nonlinear flow phenomena that is not captured in the (linear) Floquet stability analysis.

Therefore, the DNS and Floquet stability results suggest that the gravitational instability is a linear process, but its evolution throughout the period of the oscillation is nonlinear. In particular, the Floquet stability analysis fails to capture the enhanced momentum and buoyancy diffusivity of turbulence, relative to molecular diffusivities, that effectively damps the linear unstable modes in the DNS.

The Floquet analysis results indicate that the boundary layers possess linear unstable modes that arise from disturbances in the vorticity component aligned with the across-isobath velocity, for both subcritical and supercritical slopes. The susceptibility of the across-isobath vorticity to disturbances in the along-isobath direction is analogous to the linear instability found in gravitationally unstable Couette flow (Bénard and Avsec (1938); Chandra (1938); Brunt (1951); Deardorff (1965); Gallagher and A. Mercer (1965); Ingersoll (1966)). However, gravitationally unstable Couette flow is a considerably simpler case: there is no flow reversal or acceleration and the gravity vector is normal to the Couette plates. The prevalence of the bursts in the DNS associated with the across-isobath vorticity and the Floquet analysis results suggests that the linear instability of the across-isobath (or streamwise) vorticity is quite robust to parameter space variations. It seems likely that instantaneous instability analysis of the upslope flow phase of the oscillation would produce neutral stability curves similar to the Floquet analysis results in this thesis.

5.2 Slope boundary layers in the abyss

The boundary layers investigated in Chapters 2 and 3 may be observeable on hydraulically smooth abyssal ocean slopes where most of the kinetic energy of the flows is associated with the baroclinic tide. The boundary layers may occur in the presence of wave-wave interactions and breaking, but the interaction of the boundary layers and other sources of turbulence may significantly alter the boundary layer dynamics to such an extent that the boundary layers may not resemble the cases examined in Chapters 2 and 3. Therefore the boundary layers in Chapters 2 and 3 are more likely to be observable in abyssal regions where the breaking internal waves are relatively rare occurances. Heavily sedimented abyssal slopes on the eastern sides of ocean basins may be ideal conditions for observing the boundary layers in

Chapters 2 and 3, because "muddy" slopes are more likely to be hydraulically smooth and abyssal flows over eastern continental slopes have generally weak mean flows and, with the exception of canyons, are not hot spots of internal wave breaking. Figure 5-1 shows sediment depth estimates by Goff and Arbic (2010) and mean slope estimated by Becker and Sandwell (2008). Observations boundary layers on continental slopes by Gemmrich and Van Haren (2001) and Gemmrich and van Haren (2002), in a slightly different parameter regime, exhibit similar bursting behavior as the simulated flows in which the Burger number was greater than unity. They observed semidiurnal tidal boundary layers on smooth slopes with $\mathcal{O}(1$ m) boundary thicknesses and small buoyancy fluxes.

Three mid-latitude (where the M_2 tide frequency is greater that the inertial frequency, $\omega > f$) ocean basin locations were the deep mean flows are generally weak are circled in red to indicate potential places where the boundary layers in Chapters 2 and 3 might be observed. The mean slope of the seafloor in these regions are low, which suggests that dynamics similar to case 5 (low slope Burger number) are expected in these regions in absence of extenuating factors. The boundary layers in Chapters 2 and 3 are associated with small horizontal length scales on larger bathymetric features and could occur many other places in the deep ocean. As more detailed maps of the bathymetry and local flow conditions emerge, the applicability of boundary layers studied in Chapters 2 and 3 will be more readily discernable.

5.3 Implications for numerical circulation models

There are several implications for ocean circulation models in this thesis. The boundary layer turbulence examined in the DNS study confirms that anisotropy must be accounted for in turbulence models of the boundary layer, particularly within a few meters of the seafloor. Drag coefficients (Table 2.5), often used for the prediction of bottom grid cell dissipation in numerical models, were calculated for all simulations. The coefficients become quite small as the Reynolds number is decreased from 840 to 420, which suggests that a low Reynolds number cutoff threshold might be appropriate for numerical models that parameterize integrated boundary layer dissipation as $\epsilon \approx c_D|U|U^2$. In addition, the drag coefficients increased with slope angle, although the steepest slopes in this study are not

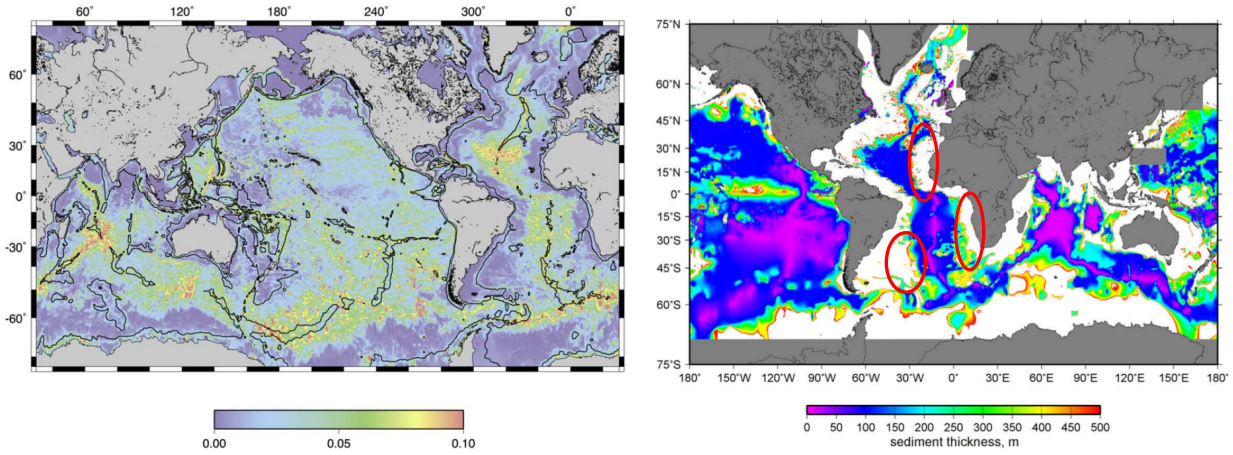

Figure 5-1: Mean slope and sediment thickness estimates.
Left: Seafloor mean slope (m/m) estimate filtered with a 60-km Gaussian filter and interpolated on a 0.5° grid, from Becker and Sandwell (2008). *Right*: Sediment thickness, with > 500 m colored in white, from Goff and Arbic (2010). Red circles are drawn where dynamics similar to cases 1 and 5 are expected.

found in the ocean at the large scales typical of circulation model resolution (scales equal to or greater than k^{-1}).

In Chapter 2, the mixing was observed to be generally weak, with the exception of the low Burger number case where a irreversible mixing efficiency of 15% was estimated to generate the weak stratification of the boundary layer. It was no surprise that the mixing is not dramatic, or even comparable, to the breaking of internal waves over rough topography in places like the Brazil Basin. The goal of the study was to understand the physics of smooth-slope tidal boundary layers produced by the rubbing of the M_2 tide against slopes in the abyss. The results of Chapter 2 suggest that a) gravitational instabilities trigger turbulence but the buoyancy fluxes are small, b) the gravitational instabilities are robust to rotation rate and slope angle, c) that above an unidentified Reynolds number the sloping boundary layer turbulence is likely to resemble the fully turbulent case of Stokes' second problem characterized by shear production rate - dissipation rate balance, and d) fully turbulent Stokes-Ekman boundary layers may be ubiquitous where mean currents are small and the slope Burger number is much less than one.

In Chapter 4, a simple neural network was used to generate a PDF fit of the dissipation rate ε conditional upon a variety of conditional variables. The PDF models were approx-

imately the same in accuracy as the power law fit of Thurnherr et al. (2015) for data set means, and accurately fit the mode (i.e. the most likely sample to be measured) of each data set as well as the total data pool. The probabilistic models discussed in Chapter 4 have several advantages: 1) the mean predictions are consistent with conventional finescale parameterization predictions; 2) new variables can be added easily; 3) the PDF of ε contains information regarding the intermittency of the turbulence, and 4) assuming erogodicity, the PDFs could be used in conjunction with the Osborn (1980) model as stochastic diapycnal mixing models within ocean circulation models. Finally, the PDF models were tested on a separate data set with different physics and ε values outside the range of the training data. Although the PDF models did not fit the test data well, the fact that the PDF model with two condition variables performed slightly better than the PDF models with a single conditional variable suggests that further improvement in accuracy might be gained by introducing other dynamically relevant variables to the model. The PDF model in Chapter 4 is remarkably versatile: It can be used as either a traditional finescale parameterization or as a PDF.

5.4 Limitations and extensions

Many branches extend from the work in this thesis, and there are many ways to improve the studies in Chapter 2, 3, and 4. A few of these are highlighted below:

High Reynolds number DNS & DNS with bottom roughness: Simulations such as these would yield a window into realistic "hot spots" of abyssal turbulence and diabatic transformation while still remaining computationally feasible.

A thorough study of the stratified Stokes-Ekman layers in the low Burger number limit: Are low Burger number stratified Stokes-Ekman layers common in the abyss, where mean flows are often weaker than tidal flows?

Validation of the $k-\varepsilon$ model of Umlauf and Burchard (2011) with DNS data:

How well do two-equation turbulence closures work for sloping abyssal boundaries with conspicuous overturns and gravitational instabilities?

Relax the Boussinesq assumption: How might the DNS cases change, and is the change significant to diabatic transformation?

Break from the vorticity-streamfunction approach to do the Floquet analysis for the rotating reference frame: The rotating reference frame disturbance equations could not be cast as two dimensional except for the wall-normal vorticity. 3D Floquet analysis would find the optimal disturbance mode (it could be not parallel to along- or across-isobath directions.

Explore the steep wall limit: The changes to the flow when the gravity vector primarily projects onto the across-isobath direction needs to be rationalized.

Systematic analysis of noise in the Floquet stability problem by using the pseudo-DNS technique of Luo and Wu (2010): Perhaps the DNS will be more unstable if the properties of the noise required for a growing mode are formalized.

Add a roughness parameter to the finescale parameterization as well as depth and other variables. Can the model blend G-H-P finescale parameterizations seemlessly with internal wave generation site parameterizations like those of St.Laurent and Garrett (2002) and Polzin (2009)?

Implement the most accurate PDF model in an general circulation model: How sensitive is the abyssal circulation to intermittent mixing?

Appendix A

Linear analytical solutions

The following is a derivation of the solutions to Equations 2.38, 2.39, and 2.40. In the other chapters of this thesis, partial derivatives are denoted by ∂_{zz} for the second derivative in z, for example. In this appendix, Leibniz notation is used for derivatives. Begin by assuming solutions of the form

$$u = \mathcal{U}(z)\mathrm{e}^{i\omega t}, \quad v = \mathcal{V}(z)\mathrm{e}^{i\omega t}, \quad b = \mathcal{B}(z)i\mathrm{e}^{i\omega t}. \tag{A.1}$$

It does not matter if we make the ansatz $\mathcal{V}(z)\mathrm{e}^{i\omega t}$ or $\mathcal{V}(z)i\mathrm{e}^{i\omega t}$ (the latter is the correct final form) because the particular solution fixes the phase relationship of u and v. Substitution into Equations Equations 2.38, 2.39, and 2.40: yields

$$\Big(i\omega - \nu\frac{\partial^2}{\partial z^2}\Big)\mathcal{U} = \mathcal{V}f\cos\theta + i\mathcal{B}\sin\theta + Ai, \tag{A.2}$$

$$\Big(i\omega - \nu\frac{\partial^2}{\partial z^2}\Big)\mathcal{V} = -\mathcal{U}f\cos\theta, \tag{A.3}$$

$$\Big(i\omega - \kappa\frac{\partial^2}{\partial z^2}\Big)i\mathcal{B} = -\mathcal{U}N^2\sin\theta. \tag{A.4}$$

The equations above can be reduced to a single inhomogeneous linear partial differential equation for the wall-normal buoyancy structure $\mathcal{B}(z)$:

$$\Big[\Big(i\omega-\nu\frac{\partial^2}{\partial z^2}\Big)\Big(i\omega-\nu\frac{\partial^2}{\partial z^2}\Big)\Big(i\omega-\kappa\frac{\partial^2}{\partial z^2}\Big) \\ +N^2\sin^2\theta\Big(i\omega-\nu\frac{\partial^2}{\partial z^2}\Big)-f^2\cos^2\theta\Big(i\omega-\kappa\frac{\partial^2}{\partial z^2}\Big)\Big]i\mathcal{B}=A\omega N^2\sin\theta. \tag{A.5}$$

Equation A.5 has six characteristic roots for the complementary (homogeneous) component of the solution and 6 linearly independent solutions. To obtain the characteristic solutions, expand all of the terms in Equation A.5:

$$\Big(\frac{\partial^6}{\partial z^6}-i\Big(\frac{2\omega}{\nu}+\frac{\omega}{\kappa}\Big)\frac{\partial^4}{\partial z^4}+\Big(-\frac{\omega^2}{\nu^2}-\frac{2\omega^2}{\nu\kappa}+\frac{f^2\cos^2\theta}{\nu^2}+\frac{N^2\sin^2\theta}{\nu\kappa}\Big)\frac{\partial^2}{\partial z^2} \\ +i\Big(-\frac{f^2\cos^2\theta\omega}{\nu^2\kappa}-\frac{N^2\sin^2\theta\omega}{\nu^2\kappa}+\frac{\omega^3}{\nu^2\kappa}\Big)\Big)\mathcal{B}=i\frac{A\omega N^2\sin\theta}{\nu^2\kappa} \tag{A.6}$$

Therefore our the nonhomogeneous ordinary differential equation has the form:

$$\Big(\frac{\partial^6}{\partial z^6}+ia_4\frac{\partial^4}{\partial z^4}+a_2\frac{\partial^2}{\partial z^2}+ia_0\Big)\mathcal{B}=if_p \tag{A.7}$$

where the subscript p denotes "particular solution" and

$$\begin{aligned}
a_4&=-\Big(\frac{2\omega}{\nu}+\frac{\omega}{\kappa}\Big)=-\frac{\omega}{\kappa}\Big(\frac{2}{\mathrm{Pr}}+1\Big)=-\frac{\omega}{\kappa}\Big(\frac{2+\mathrm{Pr}}{\mathrm{Pr}}\Big)\\
a_2&=-\frac{\omega^2}{\nu^2}-\frac{2\omega^2}{\nu\kappa}+\frac{f^2\cos^2\theta}{\nu^2}+\frac{N^2\sin^2\theta}{\nu\kappa}=\frac{f^2\cos^2\theta+\mathrm{Pr}N^2\sin^2\theta-\omega^2(1+2\mathrm{Pr})}{\kappa^2\mathrm{Pr}^2}\\
a_0&=\frac{\omega^3}{\nu^2\kappa}-\frac{f^2\cos^2\theta\omega}{\nu^2\kappa}-\frac{N^2\sin^2\theta\omega}{\nu^2\kappa}=\frac{\omega(\omega^2-f^2\cos^2\theta-N^2\sin^2\theta)}{\kappa^3\mathrm{Pr}}\\
f_p&=\frac{A\omega N^2\sin\theta}{\nu^2\kappa}
\end{aligned} \tag{A.8}$$

Equation A.7 has the characteristic equation:

$$\lambda^6+ia_4\lambda^4+a_2\lambda^2+ia_0=0, \tag{A.9}$$

which has 6 distinct solutions for λ. The total general solution is the sum of the complementary (homogeneous) solutions and the particular (nonhomogeneous) solutions:

$$\mathcal{B}(z) = \mathcal{B}_{\mathrm{c}}(z) + \mathcal{B}_{\mathrm{p}}(z) \tag{A.10}$$

The complementary solution is therefore of the form:

$$\mathcal{B}_{\mathrm{c}}(z) = c_1 \mathrm{e}^{\lambda_1} + c_2 \mathrm{e}^{\lambda_2} + c_3 \mathrm{e}^{\lambda_3} + c_4 \mathrm{e}^{\lambda_4} + c_5 \mathrm{e}^{\lambda_5} + c_6 \mathrm{e}^{\lambda_6} \tag{A.11}$$

and the particular part of the solution is of the form:

$$\mathcal{B}_{\mathrm{p}} = a_p \tag{A.12}$$

where a_p is an unknown constant.

The particular solution

To solve for a_p, substitute the particular solution form (Equation A.12 into the nonhomogeneous governing equation (Equation A.7):

$$\begin{aligned} a_p &= \frac{f_p}{a_0} \\ &= \frac{AN^2 \sin\theta}{\omega^2 - f^2 \cos^2\theta - N^2 \sin^2\theta} \end{aligned} \tag{A.13}$$

The complementary solution

Let $\phi = \lambda^2$ in Equation A.9 to obtain:

$$\phi^3 + i a_4 \phi^2 + a_2 \phi + i a_0 = 0, \tag{A.14}$$

where

$$\lambda_{1,2} = \pm\sqrt{\phi_1}, \qquad \lambda_{3,4} = \pm\sqrt{\phi_2}, \qquad \lambda_{5,6} = \pm\sqrt{\phi_2}, \tag{A.15}$$

The solutions to this equation are:

$$\beta = \sqrt[3]{2ia_4^3 + 9ia_2a_4 + 3\sqrt{3}\sqrt{4a_2^3 + a_4^2a_2^2 + 18a_0a_4a_2 + 4a_0a_4^3 - 27a_0^2} - 27ia_0} \tag{A.16}$$

$$\phi_1 = \frac{\beta}{3\sqrt[3]{2}} - \frac{\sqrt[3]{2}\,(a_4^2 + 3a_2)}{3\beta} - \frac{ia_4}{3} \tag{A.17}$$

$$\phi_2 = -\frac{\left(1 - i\sqrt{3}\right)\beta}{6\sqrt[3]{2}} + \frac{\left(1 + i\sqrt{3}\right)(a_4^2 + 3a_2)}{3 \cdot 2^{2/3}\beta} - \frac{ia_4}{3} \tag{A.18}$$

$$\phi_3 = -\frac{\left(1 + i\sqrt{3}\right)\beta}{6\sqrt[3]{2}} + \frac{\left(1 - i\sqrt{3}\right)(a_4^2 + 3a_2)}{3 \cdot 4^{1/3}\beta} - \frac{ia_4}{3} \tag{A.19}$$

Boundary conditions

For the parameter space we are interested in $c_1 = c_3 = c_5 = 0$ (to have finite solutions at $z = \infty$):

$$\mathcal{B}(z) = c_2 \mathrm{e}^{-\sqrt{\phi_1}z} + c_4 \mathrm{e}^{-\sqrt{\phi_2}z} + c_6 \mathrm{e}^{-\sqrt{\phi_3}z} + a_p \tag{A.20}$$

Therefore, the vertical structure of the oscillating component of the buoyancy field is: Now we reinterpret the boundary conditions in terms of $\mathcal{B}$:

1. No-slip at the wall applied to the across slope velocity

$$\mathcal{U} = -\frac{1}{N^2 \sin\theta}\Big(i\omega - \kappa\frac{\partial^2}{\partial z^2}\Big) i\mathcal{B} = 0, \quad \text{at} \quad z = 0$$

leads to the expression:

$$c_2(\omega + i\kappa\phi_1) + c_4(\omega + i\kappa\phi_2) + c_6(\omega + i\kappa\phi_3) = -a_p\omega \tag{A.21}$$

2. No-slip at the wall applied to the along slope velocity

$$\mathcal{V} = \frac{1}{f\cos\theta}\Big(\frac{1}{N^2\sin\theta}\Big(\omega^2 + i\omega(\nu + \kappa)\frac{\partial^2}{\partial z^2} - \nu\kappa\frac{\partial^4}{\partial z^4}\Big)\mathcal{B} - \sin\theta\mathcal{B} - A\Big) = 0, \quad \text{at} \quad z = 0$$

leads to the expression:

$$c_6(i\omega\phi_3(\kappa+\nu)-\kappa\nu\phi_3^2-N^2\sin^2\theta+\omega^2)+$$
$$c_2\left(i\omega\phi_1(\kappa+\nu)-\kappa\nu\phi_1^2-N^2\sin^2\theta+\omega^2\right)+$$
$$c_4\left(i\omega\phi_2(\kappa+\nu)-\kappa\nu\phi_2^2-N^2\sin^2\theta+\omega^2\right)=AN^2\sin\theta-a_p\left(\omega^2-N^2\sin^2\theta\right) \quad \text{(A.22)}$$

3. The adiabatic wall boundary condition

$$\frac{\partial\mathcal{B}}{\partial z}=0+0i \quad \text{at} \quad z=0$$

leads to the expression:

$$-c_4\sqrt{\phi_2}-c_6\sqrt{\phi_3}-c_2\sqrt{\phi_1}=0 \quad \text{(A.23)}$$

Therefore we can solve for the coefficients: In matrix form:

$$\mathbf{E}\cdot\mathbf{x}=\mathbf{y}$$

or

$$\begin{bmatrix}E_{11} & E_{12} & E_{13}\\ E_{21} & E_{22} & E_{23}\\ E_{31} & E_{32} & E_{33}\end{bmatrix}\begin{bmatrix}x_1\\ x_2\\ x_3\end{bmatrix}=\begin{bmatrix}y_1\\ y_2\\ y_3\end{bmatrix} \quad \text{(A.24)}$$

where we solve for

$$x_1=c_2=b_1, \quad x_2=c_4=b_2, \quad x_3=c_6=b_3, \quad \text{(A.25)}$$

with $\mathbf{E}$ and $\mathbf{y}$ specified the boundary conditions:

$$y_1=-a_p\omega, \quad y_2=AN^2\sin\theta-a_p\left(\omega^2-N^2\sin^2\theta\right) \quad y_3=0$$

$$E_{11}=\omega+i\kappa\phi_1, \quad E_{12}=\omega+i\kappa\phi_2, \quad E_{13}=\omega+i\kappa\phi_3,$$

$$E_{21}=i\omega\phi_1(\kappa+\nu)-\kappa\nu\phi_1^2-N^2\sin^2\theta+\omega^2$$

$$E_{22} = i\omega\phi_2(\kappa+\nu) - \kappa\nu\phi_2^2 - N^2\sin^2\theta + \omega^2$$

$$E_{23} = i\omega\phi_3(\kappa+\nu) - \kappa\nu\phi_3^2 - N^2\sin^2\theta + \omega^2$$

$$E_{31} = -\sqrt{\phi_1}, \quad E_{32} = -\sqrt{\phi_2}, \quad E_{33} = -\sqrt{\phi_3},$$

The solutions for the coefficients in the $\mathcal{B}$ solution (see Equation A.25) are:

$$\begin{aligned}\Upsilon &= \kappa^2\nu(\sqrt{\phi_2\phi_3}\phi_1 + \sqrt{\phi_1\phi_3}\phi_2 + \sqrt{\phi_1\phi_2}\phi_3) \\ &\quad + i\kappa\nu\omega(\sqrt{\phi_1\phi_2} + \sqrt{\phi_1\phi_3} + \sqrt{\phi_2\phi_3} + \phi_1 + \phi_2 + \phi_3) \\ &\quad + \nu\omega^2 + \kappa N^2\sin^2\theta\end{aligned}$$

$$b_1 = -\frac{1}{\left(\sqrt{\phi_1}-\sqrt{\phi_2}\right)\left(\sqrt{\phi_1}-\sqrt{\phi_3}\right)\Upsilon}\Big(A\kappa N^2\sqrt{\phi_2\phi_3}\sin\theta + iAN^2\omega\sin\theta + \kappa N^2 a_p\sqrt{\phi_2\phi_3}\sin^2\theta \tag{A.26}$$
$$+ i\kappa\nu a_p\omega(\sqrt{\phi_3}\phi_2^{3/2} + \phi_3\phi_2 + \sqrt{\phi_2}\phi_3^{3/2}) + \nu a_p\omega^2\sqrt{\phi_2\phi_3}\Big)$$

$$b_2 = \frac{1}{\left(\sqrt{\phi_1}-\sqrt{\phi_2}\right)\left(\sqrt{\phi_2}-\sqrt{\phi_3}\right)\Upsilon}\Big(A\kappa N^2\sqrt{\phi_1\phi_3}\sin\theta + iAN^2\omega\sin\theta + \kappa N^2 a_p\sqrt{\phi_1\phi_3}\sin^2\theta \tag{A.27}$$
$$+ i\kappa\nu a_p\omega(\sqrt{\phi_3}\phi_1^{3/2} + \phi_3\phi_1 + \sqrt{\phi_1}\phi_3^{3/2}) + \nu a_p\omega^2\sqrt{\phi_1\phi_3}\Big)$$

$$b_3 = -\frac{1}{\left(\sqrt{\phi_1}-\sqrt{\phi_3}\right)\left(\sqrt{\phi_2}-\sqrt{\phi_3}\right)\Upsilon}\Big(A\kappa N^2\sqrt{\phi_1\phi_2}\sin\theta + iAN^2\omega\sin\theta + \kappa N^2 a_p\sqrt{\phi_1\phi_2}\sin^2\theta \tag{A.28}$$
$$+ i\kappa\nu a_p\omega(\sqrt{\phi_2}\phi_1^{3/2} + \phi_2\phi_1 + \sqrt{\phi_1}\phi_2^{3/2}) + \nu a_p\omega^2\sqrt{\phi_1\phi_2}\Big)$$

Solutions

The solutions for the oscillating component of the flow (the components with subscript "O" in Equations 2.31 and 2.32)

$$b(z,t) = \text{real}\big[\mathcal{B}(z)i\mathrm{e}^{i\omega t}\big] = \text{Real}\big[\big(c_2\mathrm{e}^{-\sqrt{\phi_1}z} + c_4\mathrm{e}^{-\sqrt{\phi_2}z} + c_6\mathrm{e}^{-\sqrt{\phi_3}z} + a_p\big)i\mathrm{e}^{i\omega t}\big] \tag{A.29}$$

where b_1, b_2, and b_3 are given by Equations A.26, A.27, and A.28. The across-slope velocity coefficients are:

$$u_1 = b_1(\omega + i\kappa\phi_1), \tag{A.30}$$

$$u_2 = b_2(\omega + i\kappa\phi_2), \tag{A.31}$$

$$u_3 = b_3(\omega + i\kappa\phi_3), \tag{A.32}$$

and the along-slope velocity coefficients are:

$$v_1 = b_1(i\omega\phi_1(\kappa+\nu) - \kappa\nu\phi_1^2 - N^2\sin^2\theta + \omega^2), \tag{A.33}$$

$$v_2 = b_2(i\omega\phi_2(\kappa+\nu) - \kappa\nu\phi_2^2 - N^2\sin^2\theta + \omega^2), \tag{A.34}$$

$$v_3 = b_3(i\omega\phi_3(\kappa+\nu) - \kappa\nu\phi_3^2 - N^2\sin^2\theta + \omega^2), \tag{A.35}$$

and the velocity solutions are

$$\begin{aligned} u(z,t) &= \text{real}\big[\mathcal{U}(z)\mathrm{e}^{i\omega t}\big] \\ &= \text{real}\Big[\frac{\big(u_1\mathrm{e}^{-\sqrt{\phi_1}z} + u_2\mathrm{e}^{-\sqrt{\phi_2}z} + u_3\mathrm{e}^{-\sqrt{\phi_3}z} + a_p\omega\big)\mathrm{e}^{i\omega t}}{N^2\sin\theta}\Big] \end{aligned} \tag{A.36}$$

$$\begin{aligned} v(z,t) &= \text{real}\big[\mathcal{V}(z)i\mathrm{e}^{i\omega t}\big] \\ &= \text{real}\Big[\frac{\big(v_1\mathrm{e}^{-\sqrt{\phi_1}z} + v_2\mathrm{e}^{-\sqrt{\phi_2}z} + v_3\mathrm{e}^{-\sqrt{\phi_3}z} + a_p(\omega^2 - N^2\sin^2\theta) - AN^2\sin\theta\big)i\mathrm{e}^{i\omega t}}{fN^2\cos\theta\sin\theta}\Big] \end{aligned} \tag{A.37}$$

The solutions in A.29, A.36, and A.37 at $t = 0$ are the initial conditions for the simulations in Chapter 2 (with the addition of small amplitude white noise to the buoyancy) and are the

base flow for the Floquet analysis in Chapter 3 (for $f = 0$).

Appendix B

Finite difference grid convergence

Second order accurate finite difference stencils were used to form discrete matrices for the calculation of the first and second derivatives of the buoyancy disturbances (Equations 3.39 and 3.53), for the calculation of the second derivatives of the vorticity disturbances (Equations 3.38 and 3.52), and for calculating the streamfunctions by inverting the vorticity (Equations 3.35 and 3.50). Figure B-1 shows the grid convergence of the buoyancy derivative stencils when applied to the test function $b = \cos(2\pi z/H)$. The test function for checking the

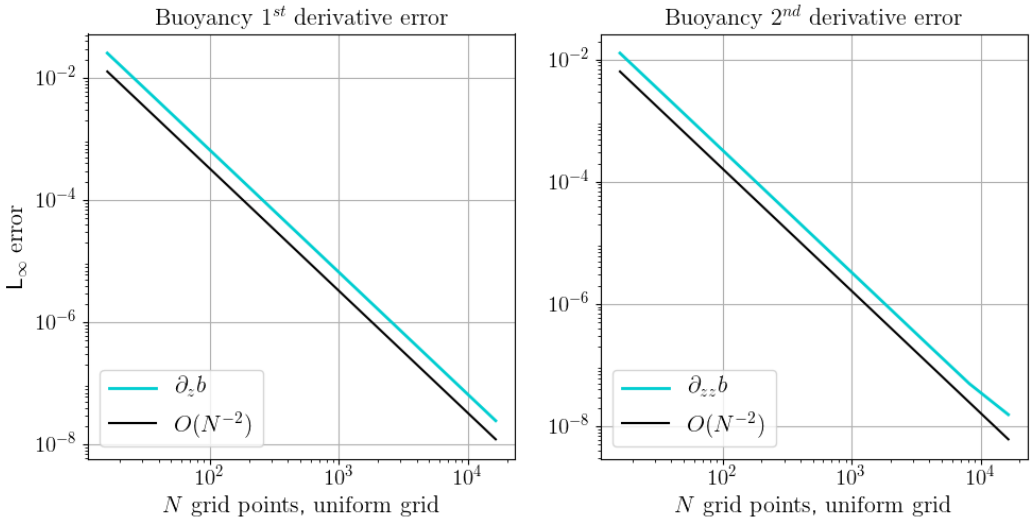

Figure B-1: Grid convergence of buoyancy derivatives.

inversions and vorticity derivatives,

$$\psi(z) = \big((z+1)^3 - z^2 - 3z - 1\big)\mathrm{e}^{-mHz} \tag{B.1}$$

was chosen because it satisfies the same boundary conditions as were required for the Floquet analysis. The test $\psi(z)$ is shown in Figure B-2. The grid convergence of the Woods (1954) vorticity boundary condition (which imposes no-slip and impermeable boundary conditions on the diffusion of vorticity), the second derivative of vorticity, and the inversion of vorticity to obtain the streamfunction are shown in Figure B-3

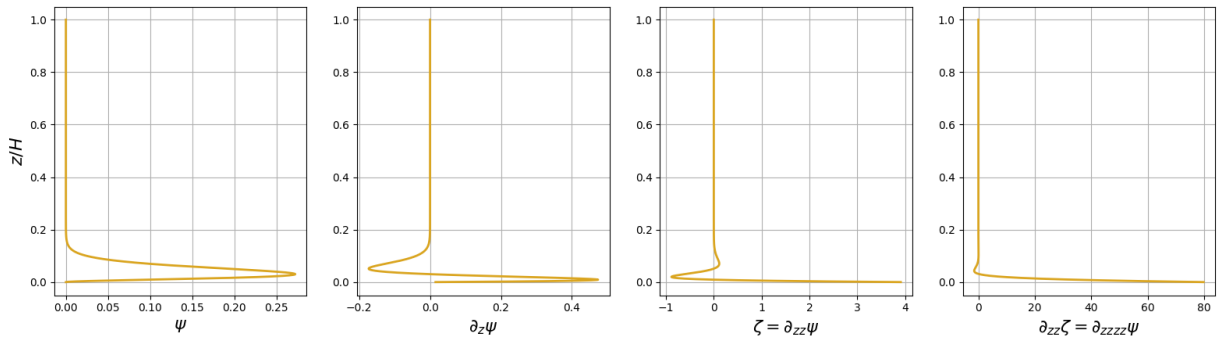

Figure B-2: Test function for ψ.

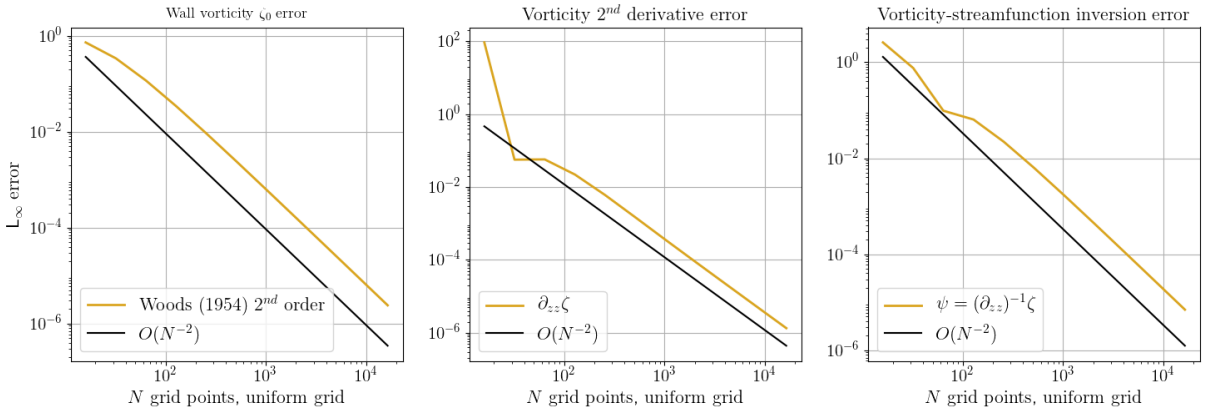

Figure B-3: Grid convergence of finite differences for the vorticity.

Bibliography

M. Abadi, A. Agarwal, P. Barham, E. Brevdo, Z. Chen, C. Citro, G. Corrado, A. Davis, J. Dean, M. Devin, et al. Tensorflow: Large-scale machine learning on heterogeneous distributed systems. *arXiv preprint arXiv:1603.04467*, 2016.

M. Alford, J. MacKinnon, J. Nash, H. Simmons, A. Pickering, J. Klymak, R. Pinkel, O. Sun, L. Rainville, R. Musgrave, et al. Energy flux and dissipation in luzon strait: Two tales of two ridges. *Journal of Physical Oceanography*, 41(11):2211–2222, 2011.

U. Ascher, S. Ruuth, and R. Spiteri. Implicit-explicit runge-kutta methods for time-dependent partial differential equations. *Applied Numerical Mathematics*, 25(2):151–167, 1997.

J. Aucan, M. Merrifield, D. Luther, and P. Flament. Tidal mixing events on the deep flanks of kaena ridge, hawaii. *Journal of Physical Oceanography*, 36(6):1202–1219, 2006.

V. Baidulov. Fine structure of one-dimensional periodic stratified flows. *Fluid Dynamics*, 45 (6):835–842, 2010.

M. Baker and C. Gibson. Sampling turbulence in the stratified ocean: Statistical consequences of strong intermittency. *Journal of Physical Oceanography*, 17(10):1817–1836, 1987.

N. Balmforth, G. Ierley, and W. Young. Tidal conversion by subcritical topography. *Journal of Physical Oceanography*, 32(10):2900–2914, 2002.

D. Barkley and R. Henderson. Three-dimensional floquet stability analysis of the wake of a circular cylinder. *Journal of Fluid Mechanics*, 322:215–241, 1996.

G. Batchelor and A. Townsend. The nature of turbulent motion at large wave-numbers. *Proceedings of the Royal Society of London. Series A. Mathematical and Physical Sciences*, 199(1057):238–255, 1949.

J. Becker and D. Sandwell. Global estimates of seafloor slope from single-beam ship soundings. *Journal of Geophysical Research: Oceans*, 113(C5), 2008.

T. Bell. Lee waves in stratified flows with simple harmonic time dependence. *Journal of Fluid Mechanics*, 67:705–722, 1975a.

T. Bell. Topographically generated internal waves in the open ocean. *Journal of Geophysical Research*, 80:320–327, 1975b.

H. Bénard and D. Avsec. Travaux récents sur les tourbillons cellulaires et les tourbillons en bandes. applications à l'astrophysique et à la météorologie. *J. Phys. Radium*, 9(11): 486–500, 1938.

C. Bishop. Mixture density networks. 1994.

P. Blennerhassett and A. Bassom. The linear stability of flat stokes layers. *Journal of Fluid Mechanics*, 464:393–410, 2002.

P. Blennerhassett and A. Bassom. The linear stability of high-frequency oscillatory flow in a channel. *Journal of Fluid Mechanics*, 556:1–25, 2006.

K. Brink and S. Lentz. Buoyancy arrest and bottom ekman transport. part i: Steady flow. *Journal of Physical Oceanography*, 40(4):621–635, 2010a.

K. Brink and S. Lentz. Buoyancy arrest and bottom ekman transport. part ii: Oscillating flow. *Journal of Physical Oceanography*, 40(4):636–655, 2010b.

D. Brunt. Experimental cloud formation. In *Compendium of Meteorology*, pages 1255–1262. Springer, 1951.

K. Burns, G. Vasil, J. Oishi, D. Lecoanet, and B. Brown. Dedalus: A flexible framework for numerical simulations with spectral methods. *arXiv preprint arXiv:1905.10388*, 2019.

G. Carter, M. Merrifield, J. Becker, K. Katsumata, M. Gregg, D. Luther, M. Levine, T. Boyd, and Y. Firing. Energetics of m 2 barotropic-to-baroclinic tidal conversion at the hawaiian islands. *Journal of Physical Oceanography*, 38(10):2205–2223, 2008.

P. Cessi. The global overturning circulation. *Annual review of marine science*, 11:249–270, 2019.

V. Chalamalla and S. Sarkar. Mixing, dissipation rate, and their overturn-based estimates in a near-bottom turbulent flow driven by internal tides. *Journal of Physical Oceanography*, 45:1969–1987, 2015.

K. Chandra. Instability of fluids heated from below. *Proceedings of the Royal Society of London. Series A-Mathematical and Physical Sciences*, 164(917):231–242, 1938.

S. Chandrasekhar. *Hydrodynamic and hydromagnetic stability*. Oxford University Press, 1961.

R. Chant and W. Stoner. Particle trapping in a stratified flood-dominated estuary. *Journal of Marine Research*, 59(1):29–51, 2001.

S. Chen, R. Chan, S. Read, and L. Bromley. Viscosity of sea water solutions. *Desalination*, 13(1):37–51, 1973.

D. Cramer. *Basic statistics for social research: Step-by-step calculations & computer techniques using minitab*. Routledge, 2002.

T. Dauxois and W. Young. Near-critical reflection of internal waves. *Journal of Fluid Mechanics*, 390:271–295, 1999.

S. Davis. The stability of time-periodic flows. *Annual Review of Fluid Mechanics*, 8(1): 57–74, 1976.

J. Deardorff. Gravitational instability between horizontal plates with shear. *The Physics of Fluids*, 8(6):1027–1030, 1965.

R. Dell and L. Pratt. Diffusive boundary layers over varying topography. *Journal of Fluid Mechanics*, 769:635–653, 2015.

D. Dommenget. The ocean's role in continental climate variability and change. *Journal of Climate*, 22(18):4939–4952, 2009.

D. Dwoyer and M. Hussaini. *Stability of time dependent and spatially varying flows*. Springer, 1987.

G. Egbert and R. Ray. Significant dissipation of tidal energy in the deep ocean inferred from satellite altimeter data. *Nature*, 405(6788):775, 2000.

R. Ferrari, M. Jansen, J. Adkins, A. Burke, A. Stewart, and A. Thompson. Antarctic sea ice control on ocean circulation in present and glacial climates. *Proceedings of the National Academy of Sciences*, 111(24):8753–8758, 2014.

R. Ferrari, A. Mashayek, T. McDougall, M. Nikurashin, and J. Campin. Turning ocean mixing upside down. *Journal of Physical Oceanography*, 2016.

G. Floquet. Sur les équations différentielles linéaires à coefficients périodiques. In *Annales scientifiques de l'École normale supérieure*, volume 12, pages 47–88, 1883.

U. Frisch and R. Morf. Intermittency in nonlinear dynamics and singularities at complex times. *Physical review A*, 23(5):2673, 1981.

M. Gad-El-Hak, S. Davis, J. Mcmurray, and S. Orszag. On the stability of the decelerating laminar boundary layer. *Journal of Fluid Mechanics*, 138:297–323, 1984.

A. Gallagher and A McD A. Mercer. On the behaviour of small disturbances in plane couette flow with a temperature gradient. *Proceedings of the Royal Society of London. Series A. Mathematical and Physical Sciences*, 286(1404):117–128, 1965.

C. Garrett. Marginal mixing theories. *Atmosphere-Ocean*, 29(2):313–339, 1991.

C. Garrett and E. Kunze. Internal tide generation in the deep ocean. *Annual Review of Fluid Mechanics*, 39:57–87, 2007.

C. Garrett, P. MacCready, and P. Rhines. Boundary mixing and arrested ekman layers: Rotating stratified flow near a sloping boundary. *Annual Review of Fluid Mechanics*, 25 (1):291–323, 1993.

B. Gayen and S. Sarkar. Turbulence during the generation of internal tide on a critical slope. *Physical Review Letters*, 104(21), 2010a.

B. Gayen and S. Sarkar. Large eddy simulation of a stratified boundary layer under an oscillatory current. *Journal of Fluid Mechanics*, 643:233–266, 2010b.

B. Gayen and S. Sarkar. Direct and large-eddy simulations of internal tide generation at a near-critical slope. *Journal of Fluid Mechanics*, 681:48–79, 2011a.

B. Gayen and S. Sarkar. Negative turbulent production during flow reversal in a stratified oscillating boundary layer on a sloping bottom. *Physics of Fluids*, 23(10):101703, 2011b.

J. Gemmrich and H. Van Haren. Thermal fronts generated by internal waves propagating obliquely along the continental slope. *Journal of physical oceanography*, 31(3):649–655, 2001.

J. Gemmrich and H. van Haren. Internal wave band eddy fluxes above a continental slope. *Journal of marine research*, 60(2):227–253, 2002.

R. Geyer and P. MacCready. The estuarine circulation. *Annual review of fluid mechanics*, 46:175–197, 2014.

C. Gibson. Intermittency of internal wave shear and turbulence dissipation. *Coastal and estuarine studies*, pages 363–376, 1998.

J. Goff and B. Arbic. Global prediction of abyssal hill roughness statistics for use in ocean models from digital maps of paleo-spreading rate, paleo-ridge orientation, and sediment thickness. *Ocean Modelling*, 32(1), 2010.

S. Goldstein et al. Modern developments in fluid dynamics, vol. 1. *Chapter XI, Section*, 1, 1938.

M. Gregg. Scaling turbulent dissipation in the thermocline. *Journal of Geophysical Research: Oceans*, 94(C7):9686–9698, 1989.

M. Gregg, H. Seim, and D. Percival. Statistics of shear and turbulent dissipation profiles in random internal wave fields. *Journal of physical oceanography*, 23(8):1777–1799, 1993.

M. Gregg, T. Sanford, and D. Winkel. Reduced mixing from the breaking of internal waves in equatorial waters. *Nature*, 422(6931):513, 2003.

M. Gregg, E. D'Asaro, J., and E. Kunze. Mixing efficiency in the ocean: annual review of marine science. *Ocean Modelling*, 10:443–473, 2018.

A. Gurvich and A. Yaglom. Breakdown of eddies and probability distributions for small-scale turbulence. *The Physics of Fluids*, 10(9):S59–S65, 1967.

J. Hart. A possible mechanism for boundary layer mixing and layer formation in a stratified fluid. *Journal of Physical Oceanography*, 1:258–262, 1971.

F. Henyey, J. Wright, and S. Flatté. Energy and action flow through the internal wave field: An eikonal approach. *Journal of Geophysical Research: Oceans*, 91(C7):8487–8495, 1986.

K. Heywood, A. Garabato, and D. Stevens. High mixing rates in the abyssal southern ocean. *Nature*, 415(6875):1011, 2002.

S. Hoerner. Fluid-dynamic drag. *Hoerner fluid dynamics*, 1965.

N. Hogg and B. Owens. Direct measurement of the deep circulation within the brazil basin. *Deep Sea Research Part II: Topical Studies in Oceanography*, 46(1-2):335–353, 1999.

R. Holmes, C. de Lavergne, and T. McDougall. Ridges, seamounts, troughs, and bowls: Topographic control of the dianeutral circulation in the abyssal ocean. *Journal of Physical Oceanography*, 48(4):861–882, 2018.

H. Hu and R. Kelly. Stabilization of longitudinal vortex instabilities by means of transverse flow oscillations. *Physics of Fluids*, 9(3):648–654, 1997.

R. Huang and X. Jin. Deep circulation in the south atlantic induced by bottom-intensified mixing over the midocean ridge. *Journal of Physical Oceanography*, 32(4):1150–1164, 2002.

A. Ingersoll. Convective instabilities in plane couette flow. *The Physics of Fluids*, 9(4): 682–689, 1966.

G. Iooss and D. Joseph. *Elementary stability and bifurcation theory*. Springer Science & Business Media, 2012.

D. Jackett and T. McDougall. A neutral density variable for the worldâĂŹs oceans. *Journal of Physical Oceanography*, 27(2):237–263, 1997.

S. Jayne and L. St. Laurent. Parameterizing tidal dissipation over rough topography. *Geophysical Research Letters*, 28(5):811–814, 2001.

D. Kingma and J. Ba. Adam: A method for stochastic optimization. *arXiv preprint arXiv:1412.6980*, 2014.

J. Klymak, R. Pinkel, and L. Rainville. Direct breaking of the internal tide near topography: Kaena ridge, hawaii. *Journal of Physical Oceanography*, 38(2):380–399, 2008.

A. Kolmogorov. The local structure of turbulence in incompressible viscous fluid for very large reynolds numbers. *Cr Acad. Sci. URSS*, 30:301–305, 1941.

I. Kovacic, R. Rand, and S.M. Sah. Mathieu's equation and its generalizations: Overview of stability charts and their features. *Applied Mechanics Reviews*, 70(2), 2018.

R. Kraichnan. Intermittency in the very small scales of turbulence. *The Physics of Fluids*, 10(9):2080–2082, 1967.

E. Kunze, E. Firing, J. Hummon, T. Chereskin, and A. Thurnherr. Global abyssal mixing inferred from lowered adcp shear and ctd strain profiles. *Journal of Physical Oceanography*, 36(8):1553–1576, 2006.

K. Lamb. Internal wave breaking and dissipation mechanisms on the continental slope/shelf. *Annual Review of Fluid Mechanics*, 46:231–254, 2014.

W. Large, J. McWilliams, and S. Doney. Oceanic vertical mixing: A review and a model with a nonlocal boundary layer parameterization. *Reviews of Geophysics*, 32(4):363–403, 1994.

C. De Lavergne, G. Madec, F. Roquet, R. Holmes, and T.J. McDougall. Abyssal ocean overturning shaped by seafloor distribution. *Nature*, 551:181–186, 2017.

J. Ledwell, E. Montgomery, K. Polzin, L. St. Laurent, R. Schmitt, and J. Toole. Evidence for enhanced mixing over rough topography in the abyssal ocean. *Nature*, 403:179–182, 2000.

S. Lentz and J. Trowbridge. The bottom boundary layer over the northern california shelf. *Journal of Physical Oceanography*, 21(8):1186–1201, 1991.

S. Levitus, J. Antonov, T. Boyer, O. Baranova, H. Garcia, R. Locarnini, A. Mishonov, J. Reagan, D. Seidov, E. Yarosh, et al. World ocean heat content and thermosteric sea level change (0–2000 m), 1955–2010. *Geophysical Research Letters*, 39(10), 2012.

A. Lorke, F. Peeters, and A. Wüest. Shear-induced convective mixing in bottom boundary layers on slopes. *Limnology and Oceanography*, 50(5):1612–1619, 2005.

A. Lorke, L. Umlauf, and V. Mohrholz. Stratification and mixing on sloping boundaries. *Geophysical Research Letters*, 35(14), 2008.

R. Lueck and T. Mudge. Topographically induced mixing around a shallow seamount. *Science*, 276(5320):1831–1833, 1997.

R. Lumpkin and K. Speer. Global ocean meridonal overturning. *Journal of Physical Oceanography*, 37(10):2550–2562, 2007.

J. Luo and X. Wu. On the linear instability of a finite stokes layer: instantaneous versus floquet modes. *Physics of Fluids*, 22(5):054106, 2010.

P. MacCready and P. Rhines. Buoyant inhibition of ekman transport on a slope and its effect on stratified spin-up. *Journal of Fluid Mechanics*, 223:631–661, 1991.

J. MacKinnon, L. St Laurent, and A. Garabato. Diapycnal mixing processes in the ocean interior. In *International Geophysics*, volume 103, pages 159–183. Elsevier, 2013.

J. Marshall and K. Speer. Closure of the meridional overturning circulation through southern ocean upwelling. *Nature Geoscience*, 5(3):171–180, 2012.

J. Marshall, D. Jamous, and J. Nilsson. Reconciling thermodynamic and dynamic methods of computation of water-mass transformation rates. *Deep Sea Research Part I: Oceanographic Research Papers*, 46(4):545–572, 1999.

A. Mashayek, H. Salehipour, D. Bouffard, P. Caulfield, R. Ferrari, M. Nikurashin, W. Peltier, and W. Smyth. Efficiency of turbulent mixing in the abyssal ocean circulation. *Geophysical Research Letters*, 44(12):6296–6306, 2017.

P. McComas, C.and Müller. Time scales of resonant interactions among oceanic internal waves. *Journal of physical oceanography*, 11(2):139–147, 1981.

G. McLachlan and K. Basford. *Mixture models: Inference and applications to clustering*, volume 84. M. Dekker New York, 1988.

A. Melet, R. Hallberg, S. Legg, and K. Polzin. Sensitivity of the ocean state to the vertical distribution of internal-tide-driven mixing. *Journal of Physical Oceanography*, 43(3):602–615, 2013.

J. Middleton and D. Ramsden. The evolution of the bottom boundary layer on the sloping continental shelf: A numerical study. *Journal of Geophysical Research: Oceans*, 101(C8): 18061–18077, 1996.

A. Monin and A. Yaglom. *Statistical fluid dynamics*, volume 1. MIT Press, 1971.

J. Moum, A. Perlin, J. Klymak, M. Levine, T. Boyd, and P. Kosro. Convectively driven mixing in the bottom boundary layer. *Journal of Physical Oceanography*, 34(10):2189–2202, 2004.

W. Munk. Abyssal recipes. *Deep Sea Research and Oceanographic Abstracts*, 13(4):707–730, 1966.

W. Munk and C. Wunsch. Abyssal recipes II: energetics of tidal and wind mixing. *Deep Sea Research Part I: Oceanographic Research Papers*, 45(12):1977–2010, 1998.

W. Munk, F. Snodgrass, and M. Wimbush. Tides off-shore: Transition from california coastal to deep-sea waters. *Geophysical and Astrophysical Fluid Dynamics*, 1(1-2):161–235, 1970.

B. Noack and H. Eckelmann. A global stability analysis of the steady and periodic cylinder wake. *Journal of Fluid Mechanics*, 270:297–330, 1994.

T. Osborn. Estimates of the local rate of vertical diffusion from dissipation measurements. *Journal of Physical Oceanography*, 10(1):83–89, 1980.

T. Peacock, R. Stocker, and J. Aristoff. An experimental investigation of the angular dependence of diffusion-driven flow. *Physics of Fluids*, 16(9):3503–3505, 2004.

B. Pearson and B. Fox-Kemper. Log-normal turbulence dissipation in global ocean models. *Physical review letters*, 120(9):094501, 2018.

W. Peltier and C. Caulfield. Mixing efficiency in stratified shear flows. *Annual Review of Fluid Mechanics*, 35(1):135–167, 2003.

O. Phillips. On flows induced by diffusion in a stably stratified fluid. *Deep Sea Research and Oceanographic Abstracts*, 17(3):435–443, 1970.

O. Phillips, J. Shyu, and H. Salmun. An experiment on boundary mixing: mean circulation and transport rates. *Journal of Fluid Mechanics*, 173:473–499, 1986.

R. Pinkel, W. Munk, P. Worcester, B. Comuelle, D. Rudnick, J. Sherman, J. Filloux, B. Dushaw, B. Howe, T. Sanford, et al. Ocean mixing studied near hawaiian ridge. *Eos, Transactions American Geophysical Union*, 81(46):545–553, 2000.

K. Polzin. Idealized solutions for the energy balance of the finescale internal wave field. *Journal of Physical Oceanography*, 34(1):231–246, 2004.

K. Polzin. An abyssal recipe. *Ocean Modelling*, 30(4):298–309, 2009.

K. Polzin and E. Montgomery. Microstructure profiling with the high resolution profiler. *Proceedings of the Office of Naval Research Workshop on Microstructure Sensors*, pages 109–115, 1996.

K. Polzin, J. Toole, and R. Schmitt. Finescale parameterizations of turbulent dissipation. *Journal of physical oceanography*, 25(3):306–328, 1995.

K. Polzin, J. Toole, J. Ledwell, and R. Schmitt. Spatial variability of turbulent mixing in the abyssal ocean. *Science*, 276(5309):93–96, 1997.

K. Polzin, A. Garabato, E. Abrahamsen, L. Jullion, and M. Meredith. Boundary mixing in orkney passage outflow. *Journal of Geophysical Research: Oceans*, 119(12):8627–8645, 2014a.

K. Polzin, A. Garabato, T. Huussen, B. Sloyan, and S. Waterman. Finescale parameterizations of turbulent dissipation. *Journal of Geophysical Research: Oceans*, 119(2):1383–1419, 2014b.

L. Prandtl. Über flussigkeitsbewegung bei sehr kleiner reibung. *Verhandl. III, Internat. Math.-Kong., Heidelberg, Teubner, Leipzig, 1904*, pages 484–491, 1904.

F. Primeau and M. Holzer. The ocean's memory of the atmosphere: Residence-time and ventilation-rate distributions of water masses. *Journal of physical oceanography*, 36(7): 1439–1456, 2006.

N. Rapaka, B. Gayen, and S. Sarkar. Tidal conversion and turbulence at a model ridge: direct and large eddy simulations. *Journal of Fluid Mechanics*, 715:181–209, 2013.

E. Richardson and E. Tyler. The transverse velocity gradient near the mouths of pipes in which an alternating or continuous flow of air is established. *Proceedings of the Physical Society*, 42(1):1, 1929.

J. Robichaux, S. Balachandar, and S. Vanka. Three-dimensional floquet instability of the wake of square cylinder. *Physics of Fluids*, 11(3), 1999.

X. Ruan and A. Thompson. Bottom boundary potential vorticity injection from an oscillating flow: A pv pump. *Journal of Physical Oceanography*, 46(11):3509–3526, 2016.

C. Sabine, R. Feely, N. Gruber, R. Key, K. Lee, J. Bullister, R. Wanninkhof, C. Wong, Do. Wallace, B. Tilbrook, et al. The oceanic sink for anthropogenic co2. *Science*, 305(5682): 367–371, 2004.

S. Salon and V. Armenio. A numerical investigation of the turbulent stokes–ekman bottom boundary layer. *Journal of Fluid Mechanics*, 684:316–352, 2011.

S. Sarkar and A. Scotti. From topographic internal gravity waves to turbulence. *Annual Review of Fluid Mechanics*, 49:195–220, 2017.

J. Sarmiento and J. Toggweiler. A new model for the role of the oceans in determining atmospheric p_{CO_2}. *Nature*, 308(5960):621–624, 1984.

H. Schlichting. Hauptaufsätze: turbulenz bei wärmeschichtung. *ZAMM Journal of Applied Mathematics and Mechanics*, 15(6):313–338, 1935.

W. Shaw, J. Trowbridge, and A. Williams. Budgets of turbulent kinetic energy and scalar variance in the continental shelf bottom boundary layer. *Journal of Geophysical Research: Oceans*, 106(C5):9551–9564, 2001.

H. Simmons, R. Hallberg, and B. Arbic. Internal wave generation in a global baroclinic tide model. *Deep Sea Research Part II: Topical Studies in Oceanography*, 51(25-26):3043–3068, 2004.

H. Simmons, S. Jayne, L.C. St.Laurent, and A. Weaver. Tidally driven mixing in a numerical model of the ocean general circulation. *Journal of Physical Oceanography*, 6(3):245–263, 2005.

J. Simpson, J. Brown, J. Matthews, and G. Allen. Tidal straining, density currents, and stirring in the control of estuarine stratification. *Estuaries*, 13(2):125–132, 1990.

D. Slinn and M. Levine. Modeling internal tides and mixing over ocean ridges. *Proceedings of the 'Aha Huliko'a Hawaiian Winter Workshop*, pages 59–68, 1997.

D. Slinn and J. Riley. Turbulent mixing in the oceanic boundary layer caused by internal wave reflection from sloping terrain. *Dynamics of atmospheres and oceans*, 24(1-4):51–62, 1996.

P. Spalart and B. Baldwin. Direct simulation of a turbulent oscillating boundary layer. In *Turbulent shear flows 6*, pages 417–440. Springer, 1987.

L. St. Laurent and H. Simmons. Estimates of power consumed by mixing in the ocean interior. *Journal of climate*, 19(19):4877–4890, 2006.

L. St Laurent and A. Thurnherr. Intense mixing of lower thermocline water on the crest of the mid-atlantic ridge. *Nature*, 448(7154):680, 2007.

L. St. Laurent, A. Garabato, J. Ledwell, A. Thurnherr, J. Toole, and A. Watson. Turbulence and diapycnal mixing in drake passage. *Journal of Physical Oceanography*, 42(12):2143–2152, 2012.

L. St.Laurent and C. Garrett. The role of internal tides in mixing the deep ocean. *Journal of Physical Oceanography*, 32(10):2882–2899, 2002.

L. St.Laurent, J. Toole, and R. Schmitt. Buoyancy forcing by turbulence above rough topography in the abyssal brazil basin. *Journal of Physical Oceanography*, 31(12):3476–3495, 2001.

H. Stommel and A. Arons. On the abyssal circulation of the world ocean- I. stationary flow patterns on a sphere. *Deep Sea Research*, 6:140–154, 1960.

H. Stommel, A. Arons, and A. Faller. Some examples of stationary planetary flow patterns in bounded basins. *Tellus*, 10(2):179–187, 1958.

L. Talley. *Descriptive Physical Oceanography.* Academic Press, 2011.

L. Talley. Closure of the global overturning circulation through the indian, pacific, and southern oceans: Schematics and transports. *Oceanography*, 26(1):80–97, 2013.

G. Taylor. Statistical theory of turbulence. *Proceedings of the Royal Society of London. Series A, Mathematical and Physical Sciences*, 151(873):421–444, 1935.

S. Thorpe. Current and temperature variability on the continental slope. *Philosophical Transactions of the Royal Society of London A: Mathematical, Physical and Engineering Sciences*, 323:471–517, 1987.

S. Thorpe. *An introduction to ocean turbulence.* Cambridge University Press, 2007.

S. Thorpe and L. Umlauf. Internal gravity wave frequencies and wavenumbers from single point measurements over a slope. *Journal of marine research*, 60(5):699–723, 2002.

A. Thurnherr and K. Speer. Boundary mixing and topographic blocking on the mid-atlantic ridge in the south atlantic. *Journal of Physical Oceanography*, 33(4):848–862, 2003.

A. Thurnherr and K. Speer. Representativeness of meridional hydrographic sections in the western south atlantic. *Journal of Marine Research*, 62(1):37–65, 2004.

A. Thurnherr, K. Richards, C. German, G. Lane-Serff, and K. Speer. Flow and mixing in the rift valley of the mid-atlantic ridge. *Journal of Physical Oceanography*, 32(6):1763–1778, 2002.

A. Thurnherr, L. St. Laurent, K. Speer, J. Toole, and J. Ledwell. Mixing associated with sills in a canyon on the midocean ridge flank. *Journal of physical oceanography*, 35(8): 1370–1381, 2005.

A. Thurnherr, E. Kunze, J. Toole, L. St.Laurent, K. Richards, and A. Ruiz-Angulo. Vertical kinetic energy and turbulent dissipation in the ocean. *Geophysical Research Letters*, 42 (18):7639–7647, 2015.

J. Toole. Temporal characteristics of abyssal finescale motions above rough bathymetry. *Journal of Physical Oceanography*, 37:409–427, 2007.

J. Toole, R. Schmitt, and K. Polzin. Estimates of diapycnal mixing in the abyssal ocean. *Science*, 264(5162):1120–1123, 1994.

J. Toole, J. Ledwell, K. Polzin, R. Schmitt, E. Montgomery, L. St.Laurent, and W. Owens. The brazil basin tracer release experiment. *International WOCE Newsletter*, 28:25–28, 1997.

J. Trowbridge and S. Lentz. Asymmetric behavior of an oceanic boundary layer above a sloping bottom. *Journal of Physical Oceanography*, 21(8):1171–1185, 1991.

R. Turnewitsch, S. Falahat, J. Nycander, A. Dale, R. Scott, and D. Furnival. Deep-sea fluid and sediment dynamicsâĂŤinfluence of hill-to seamount-scale seafloor topography. *Earth-Science Reviews*, 127:203–241, 2013.

L. Umlauf and H. Burchard. Diapycnal transport and mixing efficiency in stratified boundary layers near sloping topography. *Journal of Physical Oceanography*, 41(2):329–345, 2011.

C. Von Kerczek and S. Davis. The instability of a stratified periodic boundary layer. *Journal of Fluid Mechanics*, 75(2):287–303, 1976.

A. Waterhouse, J. MacKinnon, J. Nash, M. Alford, E. Kunze, H. Simmons, K. Polzin, L. St. Laurent, O. Sun, R. Pinkel, et al. Global patterns of diapycnal mixing from measurements of the turbulent dissipation rate. *Journal of Physical Oceanography*, 44(7): 1854–1872, 2014.

G. Weatherly, S. Blumsack, and A. Bird. On the effect of diurnal tidal currents in determining the thickness of the turbulent ekman bottom boundary layer. *Journal of Physical Oceanography*, 10(2):297–300, 1980.

C. Whalen, L. Talley, and J. MacKinnon. Spatial and temporal variability of global ocean mixing inferred from argo profiles. *Geophysical Research Letters*, 39(18), 2012.

C. Whalen, J. MacKinnon, L. Talley, and A. Waterhouse. Estimating the mean diapycnal mixing using a finescale strain parameterization. *Journal of Physical Oceanography*, 45(4): 1174–1188, 2015.

S. Wijffels, D. Roemmich, D. Monselesan, J. Church, and J. Gilson. Ocean temperatures chronicle the ongoing warming of earth. *Nature Climate Change*, 6(2):116, 2016.

K. Winters. Tidally driven mixing and dissipation in the stratified boundary layer above steep submarine topography. *Geophysical Research Letters*, 42(17):7123–7130, 2015.

L. Woods. A note on the numerical solution of fourth order differential equations. *The Aeronautical Quarterly*, 5(4):176–184, 1954.

C. Wunsch. On oceanic boundary mixing. *Deep Sea Research and Oceanographic Abstracts*, 17(2):293–301, 1970.

C. Wunsch and R. Ferrari. Vertical mixing, energy, and the general circulation of the oceans. *Annual Reviews of Fluid Mechanics*, 36:281–314, 2004.

N. Zilberman, J. Becker, M. Merrifield, and G. Carter. Model estimates of m 2 internal tide generation over mid-atlantic ridge topography. *Journal of Physical Oceanography*, 39(10): 2635–2651, 2009.